KU LEUVEN

FACULTEIT WETENSCHAPPEN

β-delayed fission and α-decay spectroscopy of ^{194,196}At

Simon SELS

Promotor: Prof. Dr. P. Van Duppen
Begeleider: L. Ghys

Proefschrift ingediend tot het behalen van de graad van Master of Science in Physics

Academiejaar 2012-2013

"Obstacles are those frightening things we see when we take our eyes of our goal."

Henry Ford

Contents

List of Figures vi

List of Tables viii

Dankwoord ix

Samenvatting xi

Summary xiii

Vulgariserende samenvatting xv

1 Introduction **1**
- 1.1 General nuclear concepts . . . 1
- 1.2 Nuclear decay processes . . . 2
  - 1.2.1 α decay . . . 2
  - 1.2.2 β decay . . . 3
  - 1.2.3 γ decay . . . 4
- 1.3 Fission . . . 5
  - 1.3.1 Fission fragment mass distributions . . . 6
  - 1.3.2 Theoretical descriptions . . . 8
  - 1.3.3 β-delayed fission . . . 10
    - 1.3.3.1 β-delayed fission process and systematics . . . 10
    - 1.3.3.2 Regions of occurrence . . . 13
- 1.4 Decay of ^{194,196}At . . . 15

2 Motivation **16**
- 2.1 βDF of At . . . 16
- 2.2 α-decay spectroscopy . . . 19
- 2.3 Further studies on At . . . 19

3 Experiment **20**
- 3.1 ISOLDE . . . 20
  - 3.1.1 Laser Ionisation . . . 21
  - 3.1.2 Mass separation . . . 23
- 3.2 Windmill system . . . 25

3.3 Detectors . . . 26
3.3.1 Silicon detectors . . . 26
3.3.1.1 Pulse height defect . . . 28
3.3.2 Germanium detectors . . . 29

4 Alpha decay spectroscopy of ^{196}At 30
4.1 Data . . . 30
4.2 ^{196}At fine structure . . . 35
4.3 α-γ analysis and the ^{192}Bi level scheme . . . 36
4.3.1 Projections and possible relations . . . 37
4.3.2 Running gates . . . 43
4.3.3 Possible α+e^{-} summing in region C and D . . . 44
4.3.4 Populating only one isomer in ^{192}Bi . . . 48
4.3.5 ^{192}Bi level scheme . . . 50
4.3.6 Reduced α widths, δ_{α}^{2} . . . 51
4.4 Calculation of b_{β} for ^{196}At . . . 52
4.4.1 Direct production . . . 54
4.4.2 Additional corrections . . . 56
4.5 Determination of half lives . . . 58

5 Fission analysis 62
5.1 Schmitt calibration . . . 62
5.2 Determination of mass and TKE distributions . . . 64
5.3 SRIM simulations . . . 66
5.3.1 Implantation depth . . . 66
5.3.2 Energy loss of fission fragments in carbon foil . . . 68
5.4 Discussion of mass and TKE distributions . . . 71
5.5 $P_{\beta DF}$ and $T_{1/2p,\beta DF}$ of ^{196}At . . . 75

6 Conclusion 79

Bibliography 81

List of Figures

1.1 Chart of nuclei . . . 2
1.2 Fission barrier (1) . . . 5
1.3 Symmetric and asymmetric fission fragment mass distributions . . . 6
1.4 Asymmetric fission due to shell effects . . . 7
1.5 Fission barrier(2) . . . 9
1.6 Potential Energy Surface (PES) and shape parameters . . . 10
1.7 β-Delayed fission . . . 11
1.8 $T_{1/2p,\beta DF}$ systematics . . . 12
1.9 Viola plot . . . 13
1.10 Regions with β-Delayed fission . . . 14
1.11 Q(At) and B_f(Po) . . . 14
1.12 Decay of ^{194,196}At . . . 15

2.1 Asymmetric fission of ^{180}Hg . . . 17
2.2 Fission (a)symmetry regions . . . 18

3.1 ISOLDE Layout . . . 21
3.2 At creation and separation . . . 22
3.3 At ionization scheme . . . 22
3.4 Contamination in ion beams . . . 23
3.5 Comparison of GPS and HRS contaminants . . . 24
3.6 Experimental Setup . . . 25
3.7 Windmill system . . . 26
3.8 Windmill implantation station . . . 28
3.9 Windmill implantation station: Detector names . . . 28

4.1 Spectrum: Total energy range (Si detector) . . . 31
4.2 Energy spectrum for each Si detector . . . 32
4.3 $\alpha - \gamma$ time difference . . . 33
4.4 $\alpha - \gamma$ coincidence plot . . . 34
4.5 ^{196}At fine structure (fit) . . . 35
4.6 α-γ coincidence plot 2 . . . 36
4.7 $\alpha - \gamma$ time difference - Region E . . . 37
4.8 coincident γ projections . . . 38
4.9 coincident γ projections X-ray region . . . 40
4.10 ^{192}Bi level scheme - part 1 . . . 41

4.11 γ-γ coincidence plot . . . 42
4.12 γ-γ coincidence projection (200 keV) . . . 43
4.13 Running gate on 200 keV and 221 keV γ . . . 44
4.14 α + conversion e^- energies . . . 46
4.15 α decay of ^{192}Bi . . . 48
4.16 preliminary ^{192}Bi level scheme . . . 51
4.17 Direct production: Lasers on/off . . . 55
4.18 Direct production: Po and Bi time structure . . . 55
4.19 WM movement: Timing . . . 57
4.20 WM movement: Count correction . . . 58
4.21 ^{196}Po Half life . . . 60
4.22 ^{192}Bi Half life . . . 60
4.23 ^{196}At Half life . . . 61

5.1 SRIM implanation depth . . . 67
5.2 Projection of SRIM implantation depth . . . 67
5.3 Beamspot and emission angles randomization . . . 68
5.4 Energy loss simulation . . . 69
5.5 Energy loss in carbon foil . . . 70
5.6 Mass distributions of ^{194,196}At . . . 71
5.7 TKE distributions after βDF of ^{194,196}At . . . 72
5.8 Mass distributions of ^{196}At gating on low and high TKE . . . 73
5.9 Mass distributions of ^{194}At gating on low and high TKE . . . 73
5.10 3D representation of mass and TKE distributions of ^{196}At . . . 74
5.11 3D representation of mass and TKE distributions of ^{194}At . . . 75
5.12 Viola plot with ^{196}At . . . 76
5.13 Plot with $T_{1/2p,\beta DF}$ systematics including ^{196}At . . . 78

List of Tables

3.1 table: Silicon detector specifics 28

4.1 table: α fine structure energies and integrals 36
4.2 table: Observed γ-ray energies and X-rays for different regions 39
4.3 table: γ energy addition 42
4.4 table: α + conversion e^- sum energies 47
4.5 table: Expected sum counts in region C 47
4.6 table: Beta branch 54
4.7 table: ^{196}Po counts for dedicated lasers Off/On measurements 56
4.8 table: Half lives 59
4.9 table: ^{196}At fine structure half lives 59

5.1 table: Calibration constants for fission analysis 63
5.2 table: Fit results for TKE and mass distribution of ^{194,196}At 75
5.3 table: Number of observed fission events of ^{194,196}At for GPS and HRS data 76
5.4 table: $P_{\beta DF}$ and $T_{1/2p,\beta DF}$ of ^{196}At for GPS and HRS data 77

Dankwoord

Het werk, zoals ik het hier presenteer in deze thesis, had nooit kunnen worden wat het nu is zonder de hulp van vele mensen. Ik vind het daarom ook belangrijk om deze personen hier te bedanken voor alle steun die ze mij geboden hebben.

Ten eerste zou ik graag mijn promotor Piet Van Duppen, Mark Huyse en Ricardo Raabe willen bedanken om mij de mogelijkheid te bieden dit jaar te spenderen in een ongelofelijk aangename onderzoeksgroep, alsook voor de ophelderende gesprekken die mijn onderzoek hebben vooruit geholpen. De experimenten in CERN waarin ik dankzij hen heb kunnen deelnemen waren extreem boeiend en leerrijk.

Op de tweede plaats verdient Lars, mijn begeleider, een geweldig grote "Dankuwel!". Hij heeft mij doorheen het ganse jaar bijna dagelijks geholpen. Zelfs toen ik gedurende enkele maanden in het eerste semester in York op erasmus-uitwisseling was, stond hij mij bij via Skype. Van Lars heb ik het voorbije jaar gigantisch veel geleerd, gaande van programmeren en het uitvoeren van analyse, tot de technische kant van het experimenteren zoals in CERN. Voor een leuke portie humor en gelach was hij gelukkig ook steeds te vinden. I wouldn't have had such a great experience last year, if I had not been put in our office, 'Café Coulex', at the IKS. Therefore, I would like to thank Nele, Kashia, Liam and also Jan for the great times I had there, and I must say that I feel sad to leave such a wonderful office.

A great 'Thank you' also goes out to Andrei Andreyev and the nuclear structure group at the University of York. They made me feel at home during my stay in the UK. I made some great friends in York, whom I would very much like to thank personally: Mark, Chris, Adam, Tom, Phil, Jack, Laura, Victoria and Adele, Thank you very much

for making my stay in York such an unforgettable experience. Thanks to them, I became the best-ranked Belgian player in the Physics Squash League in York. Though I must add, I was the *only* Belgian player. Thanks for the fun times, guys.

Graag wou ik ook nog mijn jaargenoten en medestudenten Fysica willen bedanken voor de geweldig leuke voorbije 5 jaar in Leuven. Een speciale bedanking gaat hierbij uit naar Ruben, Valerie, Janne, Maarten, Jake, Kaveh en Elise voor de leuke tijd op het IKS.

Mijn ouders en drie broers wil ik bedanken om mij te steunen door dik en dun in alles wat ik tot nu toe heb gedaan. Als allerlaatste zou ik dan ook nog Lieselot willen bedanken: Bedankt om er steeds voor mij te zijn!

Ranst
Juni 2013

Samenvatting

In dit werk worden de neutronarme kernen ^{194,196}At (Z= 85, N= 109, 111) onderzocht. Meerbepaald werd het α-verval van ^{196}At, alsook de β-vertraagde fissie van ^{194,196}At bestudeerd. β-vertraagde fissie is een twee-staps vervalproces waarbij een moederkern (in dit geval ^{194,196}At) via β verval geëxciteerde toestanden van een dochterkern voedt. Wanneer deze geëxciteerde toestanden in de nabijheid van of boven de zogenaamde fissiebarrière van de dochterkern zijn gelegen, bestaat er een mogelijkheid dat deze kern fissie ondergaat.

De studie van bovengenoemde vervalmethodes is interessant omwille van verschillende redenen. Zo is β-vertraagde fissie een unieke methode om lage-energie fissie te bestuderen in kernen die anders geen spontane fissie zouden ondergaan. Door het bestuderen van de vrijgekomen totale kinetische energie (TKE) en de massadistributie van de uitgestuurde fissie-fragmenten, kunnen fissietheorieën getoetst worden aan experimentele resultaten en eventueel verbeterd worden. Recente studies hebben een onverwacht fissiegedrag geobserveerd van ^{180}Hg, dewelke werd bestudeerd via β-vertraagde fissie van ^{180}Tl. Asymmetrische fissie, waarbij de splitsende kern vervalt in een zwaardere en lichtere kern, werd waargenomen, hoewel symmetrische fissie werd verwacht. Hierdoor werd op de kernkaart een nieuwe regio van assymetrische fissie ontdekt. De kernen die in deze thesis worden bestudeerd, liggen in een regio waar een overgang wordt verwacht van asymmetrische naar symmetrische fissie.

De experimenten waarvan de data werd geanalyseerd in deze thesis, werden uitgevoerd in de ISOLDE-faciliteit in CERN. Hier werden de bestudeerde kernen ^{194,196}At geproduceerd via een spallatiereactie. Deze reactie werd geïnduceerd door middel van een energetische botsing van versnelde protonen met een uraniumcarbide trefschijf. De geproduceerde At-elementen werden geïoniseerd met behulp van een driestaps laserionisatieproces, waarna ze werden geëxtraheerd met elektroden om vervolgens te worden

gescheiden op basis van massa in een massaseparator. De ionen werden geïmplanteerd in koolstoffolies, die op een roterend wiel werden gemonteerd. Langerlevend verval kan worden opgemeten door, na elke supercyclus, de koolstoffolie te roteren van het implantie- naar het vervalstation. In de detectieopstelling werd het radioactief verval van de geïmplanteerde kernen gedetecteerd met behulp van vier siliciumdetectoren, twee-bij-twee verdeeld over het implantatie- en vervalstation, en twee germanium detectoren.

Aan de hand van de studie van het α-verval van ^{196}At, werd de tot nog toe onbekende fijnstructuur van ^{196}At bepaald. Hier werden ten minste drie nieuwe α lijnen bepaald. Door middel van het bestuderen van de α-γ coïncidenties werd een voorlopig niveauschema voor ^{192}Bi opgesteld. Dit werd gedaan door het onderzoeken van de energieën van, en de mogelijke relaties tussen de uitgezonden γ-stralen. Ook werd onderzocht of het mogelijk was of enkele α-pieken in het energiespectrum te verklaren zijn via het 'kunstmatige' effect van α-elektron somming. Een argumentatie werd opgebouwd om aan te tonen dat slechts één isomeer van ^{192}Bi werd gevoed, wat erop kan wijzen dat ook slechts één isomeer van ^{196}At werd geproduceerd. Een precieze waarde voor de β-vertakking van ^{196}At werd bepaald. Het hoofdstuk wordt afgesloten met de bepaling van half-waardetijden van verschillende geproduceerde isotopen. Deze half-waardetijden werden vervolgens vergeleken met literatuurwaarden.

In het eerste deel van het hoofdstuk in verband met de fissieanalyse, wordt de Schmitt-calibratie uitgelegd. Hiermee worden de opgemeten pulshoogten van de fissiefragmenten omgezet tot TKE- en massadistributies. Energieverlies in de koolstoffolie werd gesimuleerd met behulp van het SRIM computerprogramma. De uiteindelijk bekomen TKE- en massadistributies vertonen interessante eigenschappen, waarbij een relatie tussen beide observabelen waargenomen werd. Zo komt een hoge TKE in beide isotopen overeen met een smalle symmetrische piek in de massadistributie. De lagere TKE-waarden komen overeen met een veel bredere of zelfs asymmetrische massaverdeling. Twee duidelijk verschillende fissiemodi werden dus gevonden. Dit hoofdstuk wordt afgesloten met de bepaling van de partiële half-waardetijd en kans voor β-vertraagde fissie. Beide waarden worden vergeleken met eerder gevonden waarden voor andere kernen.

In het laatste hoofdstuk van deze thesis wordt een conclusie van de uitgevoerde analyse geformuleerd en worden mogelijke vooruitzichten voor een verdere studie aangekaart.

Summary

In this work, the neutron-deficient nuclei of ^{194,196}At (Z= 85, N= 109, 111) are studied. More specifically, the α decay of ^{196}At and the β-delayed fission of ^{194,196}At are discussed. β-delayed fission is a two-step decay process where a parent nucleus (^{194,196}At in this case) populates excited states of a daughter nucleus via β decay. When these excited states are located in the vicinity of the so-called fission barrier, the possibility exists that this nucleus undergoes fission.

The study of above-mentioned decay methods is interesting because of different reasons. β-delayed fission is a unique method to study low-energy fission in nuclei which would otherwise not undergo spontaneous fission. In low-energy fission, microscopic effects such as shell effects or pairing, which have an influence on the fission process, are not negligible. By studying the amount of released total kinetic energy (TKE) and the mass distributions of the emitted fission fragments, fission theories can be compared to experimental results and possibly be enhanced. Recent studies have observed an unexpected fission behavior of ^{180}Hg, which was studied via β-delayed fission of ^{180}Tl. Asymmetric fission, where a fissioning nucleus splits into a heavy and a light nucleus, was found, although symmetric fission was expected. Because of this, a new region of asymmetric fission on the nuclear chart was discovered. The nuclei studied in this thesis are found in a region where a transition from asymmetric to symmetric fission is expected.

The experiments of which the data was analyzed in this thesis, were conducted at the ISOLDE facility in CERN. Here, the studied ^{194,196}At nuclei were produced via a spallation reaction. This reaction was induced by an energetic collision of accelerated protons with an uraniumcarbide target. The produced At elements were ionized via a three-step laser ionization process, after which they were extracted with electrodes in

order to be mass separated in a mass separator. The ions were implanted in carbon foils which were mounted on a rotating wheel. Longer-living decay can be measured by rotating the carbon foil from the implantation to the decay station after every super cycle. In the detection setup, the radioactive decay of the implanted nuclei was detected with four silicon detectors, pair-wise distributed over the implantation and decay station, and two germanium detectors.

Based on the study of the α decay of ^{196}At, the hitherto unknown fine structure of ^{196}At can be determined. At least three new α-decay lines were observed. By studying α-γ coincidences, a preliminary level scheme of ^{192}Bi was presented. This was done by investigating the energies of, and possible relations between the emitted γ rays. It was also investigated whether or not several α peaks in the energy spectrum could be explained by the 'artificial' effect of α-electron summing. An argumentation was built to show that only one isomer of ^{192}Bi was populated, which may point to the population of only one isomer of ^{196}At. A precise value of the β branch of ^{196}At was determined. The chapter is concluded with the determination of half-lives of several produced isotopes. These half-lives were then compared to literature values.

In the first part of the chapter concerning the fission analysis, the so-called Schmitt-calibration is explained. With this calibration, the measured pulse heights of the fission fragments can be converted to TKE- and mass distributions. The so-called pulse-height defect, to which silicon detectors are subjected, and the energy loss in the carbon foils are accounted for. This energy loss in the carbon foil was simulated using the SRIM program. The obtained TKE- and mass distributions show interesting properties, for which a relationship between both observables was found. As such, a high TKE corresponds to a narrow symmetric peak in the mass distribution for both isotopes. The lower TKE values correspond to a much broader or even asymmetric mass distribution. Two very different fission modes were thus observed. This chapter is ended with the determination of the partial half-life and the probability of β-delayed fission. Both values are compared to previously-found values for different isotopes.

In the final chapter of this thesis, a conclusion of the conducted analysis is formulated and a possible outlook for a further study is discussed.

Vulgariserende samenvatting

Een atoom, de bouwsteen van al het tastbare dat we rondom ons waarnemen, is opgebouwd uit een atoomkern met daarrond elektronen. De kern, die slechts heel erg klein is ten opzichte van het hele atoom, bevat zowat alle massa van het atoom en bestaat uit nog kleinere deeltjes die protonen en neutronen worden genoemd. Isotopen zijn elementen met hetzelfde aantal protonen, maar een verschillend aantal neutronen in hun atoomkern. In deze thesis worden twee verschillende isotopen van Astaat (At) bestudeerd, namelijk ^{194,196}At. De bestudeerde isotopen zijn radioactief en kortlevend. Ze vervallen via α- of β-verval, waarbij respectievelijk Bi en Po worden geproduceerd. Soms wordt via β-verval Po geproduceerd waarvan de kern energetisch genoeg is om kernsplitsing (=fissie) te ondergaan. Dit twee-stapsprocess, waarbij een kern eerst β-verval ondergaat en daarna splitst, noemt men β-vertraagde fissie. In deze thesis worden zowel het α-verval van ^{196}At als de β-vertraagde fissie van ^{194,196}At onderzocht.

De studie van bovengenoemde vervalmethodes is interessant omwille van verschillende redenen. Zo is β-vertraagde fissie een unieke methode om lage-energie fissie te bestuderen. Door het bestuderen van de vrijgekomen totale kinetische energie (TKE) en de massa's van de uitgestuurde fissie-fragmenten, kunnen fissietheorieën getoetst worden aan experimentele resultaten en eventueel verbeterd worden. Recente studies hebben een onverwacht fissiegedrag geobserveerd van ^{180}Hg, dewelke werd bestudeerd via β-vertraagde fissie van ^{180}Tl. Asymmetrische fissie, waarbij de splitsende kern vervalt in een zwaardere en lichtere kern, werd waargenomen, hoewel symmetrische fissie werd verwacht. Hierdoor werd op de kernkaart een nieuwe regio van assymetrische fissie ontdekt. De kernen die in deze thesis worden bestudeerd, liggen in een regio waar een overgang wordt verwacht van asymmetrische naar symmetrische fissie.

De experimenten waarvan de data werd geanalyseerd in deze thesis, werden uitgevoerd in mei 2011 en mei 2012 in de ISOLDE-faciliteit in CERN. Hier werden de ^{194,196}At isotopen geproduceerd via een kernreactie. Deze reactie werd geïnduceerd door middel van een energetische botsing van versnelde protonen met uranium. Na de productie werden ze zeer precies geselecteerd uit een grote hoeveelheid van andere elementen die ook werden aangemaakt, waarna ze naar de detectieopstelling werden geleid. Hier werd het verval van de isotopen exact opgemeten.

Aan de hand van de studie van het α-verval van ^{196}At, konden eigenschappen worden bestudeerd die tot nog toe onbepaald waren. Zo werd de preciese verhouding tussen de hoeveelheid α- en β-verval berekend en werd ook een voorlopige versie van het zogenoemde niveauschema van ^{192}Bi opgesteld. Ook werden de half-waardetijden voor verschillende isotopen bepaald en vergeleken met literatuurwaarden. In de studie van de β-vertraagde fissie van ^{194,196}At kwamen interessante eigenschappen aan het licht. Zo werd er een relatie gevonden tussen de hoeveelheid kinetische energie die vrijkomt bij een splitsing van Po en de massa's van de kernen waarin Po uiteindelijk splitste. Twee zeer verschillende fissiemodi werden gevonden.

In het laatste hoofdstuk wordt een conclusie van de uitgevoerde analyse geformuleerd en worden mogelijke vooruitzichten voor een verdere studie aangekaart.

Chapter 1

Introduction

In this introductory chapter, general nuclear concepts, nuclear decay processes important for understanding β-delayed fission and the spectroscopic data analysis in this thesis are discussed. α, β and γ decay, as well as fission are explained.

1.1 General nuclear concepts

Atoms consist of an electron cloud surrounding an atomic nucleus. Almost all of the atomic mass is situated in the nucleus, which is very small compared to the size of the atom (10^{-15} compared to 10^{-10} m) [1].
A nucleus consists of Z positively charged protons and N neutrons having a neutral charge. The total number of nucleons A is called the mass number and Z, the atomic number, characterizes the atom. The electromagnetic interaction pushes protons away from each other, while the strong force, felt by both protons and neutrons, keeps the nucleons together. The weak interaction is also present in the nucleus and is responsible for e.g. β decay, but gravitation can be neglected due to the small masses of the nucleons ($\sim 10^{-27}$ kg).
Nuclides having the same Z, but different N are called isotopes, while isotones have the same N, and isobars the same mass number A. Generally, nuclides are respesented as ${}^{A}_{Z}X_{N}$.

The nuclear chart shown in figure 1.1 plots all known nuclei in function of Z (vertically) and N (horizontally). The color code denotes stability (black squares) or the main

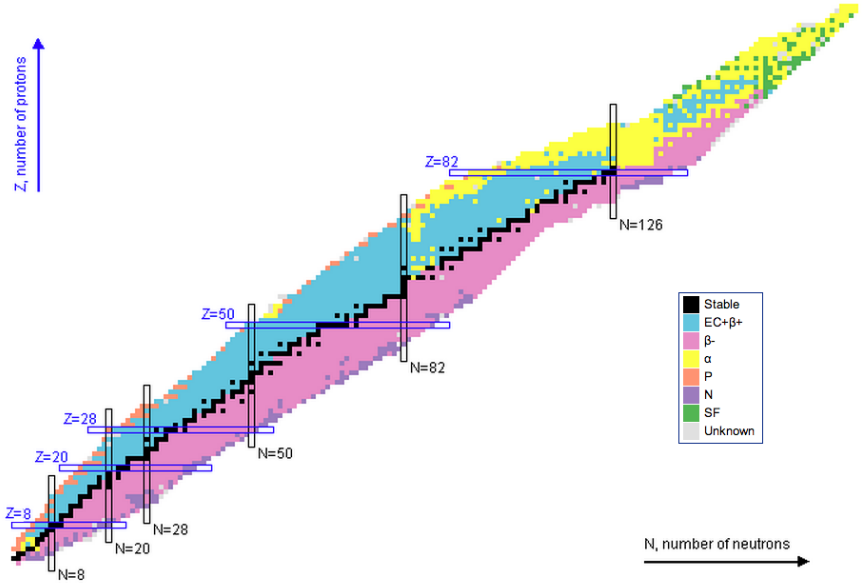

FIGURE 1.1: Chart of nuclei. Figure taken from [2].

process of decay for a certain nucleus. Several of these processes are discussed in section 1.2.

1.2 Nuclear decay processes

1.2.1 α decay

α decay is the process whereby a nucleus emits an α particle, which is in fact a helium nucleus consisting of two protons and two neutrons. The process is thus represented as:

$$^{A}_{Z}X_{N} \rightarrow ^{A-4}_{Z-2} X'_{N-2} + \alpha. \tag{1.1}$$

The net energy released in a decay process, the Q value, is calculated for α decay as

$$Q = (m(X) - m(X') - m(\alpha))\, c^2 \tag{1.2}$$

where $m(X)$ denotes the neutral atomic mass of X.
Usually, the Q-value is of the order of 5 MeV for an α-emission process.
Most α emitters have a mass higher than $A \sim 150$. Moreover, it becomes a dominant decay process in nuclei exceeding mass number 190.

α emission can be considered a tunneling process, where an α particle behaves as if it resides in a spherical region determined by the daughter nucleus. The probability for α decay and tunneling trough this potential barrier are strongly related. A certain state in a parent nucleus can also populate many different states in the daughter nucleus. This is denoted as the 'fine structure' of α decay. Since the spin of the α particle is equal to zero, the angular momentum carried by an α particle must be orbital in nature. The tunneling probability for an α particle trough the barrier depends on the Q value between the initial and final state, but also on the height and thickness of the barrier. This barrier height is increased with a 'centrifugal potential' proportional to $l(l+1)$, where l denotes the angular momentum. As a result of this, the probability of α decay for a given initial state decreases with increasing final state energy and increasing angular momentum change. The parity change associated with α emission is $(-1)^l$ [1].

1.2.2 β decay

Three closely related nuclear processes, β^+, β^- and electron capture (EC), are commonly denoted as β decay. In all of these processes a bound proton in the nucleus is converted to a neutron or vice versa, thus changing the proton number Z and neutron number N by one unit, but keeping the mass number A constant. The processes are written as

$$ {}^{A}_{Z}X_N \rightarrow {}^{A}_{Z+1}X'_{N-1} + e^- + \bar{\nu} \qquad \text{for } \beta^- \text{ decay} \tag{1.3} $$

$$ {}^{A}_{Z}X_N \rightarrow {}^{A}_{Z-1}X'_{N+1} + e^+ + \nu \qquad \text{for } \beta^+ \text{ decay} \tag{1.4} $$

$$ {}^{A}_{Z}X_N + e^- \rightarrow {}^{A}_{Z-1}X'_{N+1} + \nu \qquad \text{for electron capture} \tag{1.5} $$

where on the left-hand side, the parent nucleus is given and on the right-hand side the daughter nucleus, emitted β particles and (anti)neutrinos are given. In electron capture, an atomic electron, mostly from the K- or L-shell, is absorbed in the nucleus. In order to fill the resulting vacancy, electrons rearrange in the atomic shells and characteristic X rays are emitted. An important feature, due to the fact that $\beta^{\pm}$ decay is a three body process, is the continuous energy distribution of β particles, ranging from zero to an upper limit, the endpoint energy. In electron capture only two end products are present, so the emitted neutrino is monoenergetic. β decay provides a convenient way for an unstable nucleus to "slide down" the mass parabola of constant A and to approach the stable isobar [1]. β^-- and β^+/EC decay will thus respectively

happen on the neutron- and proton-rich side of the nuclear chart.
The Q value for the three different β-decay processes are calculated as

$$Q_{EC} = \left(m\left({}^{A}X\right) - m\left({}^{A}X'\right)\right)c^2 - B_n \tag{1.6}$$
$$Q_{\beta^+} = \left(m\left({}^{A}X\right) - m\left({}^{A}X'\right) - 2m_e\right)c^2 \tag{1.7}$$
$$Q_{\beta^-} = \left(m\left({}^{A}X\right) - m\left({}^{A}X'\right)\right)c^2. \tag{1.8}$$

In these formulas, X represents the parent nucleus, X' the daughter nucleus and $m(X)$ the neutral atomic mass of X. B_n is the binding energy of the captured electron in the electron-capture process and m_e is the electron mass.

Note that β^+ decay involves the creation of an electron-positron pair, as represented by the $2m_ec^2$ (=1022 keV) term in eq. 1.7. EC decay can thus have a positive Q-value, while β^+ decay is prohibited [1].

1.2.3 γ decay

Gamma rays are emitted when a nucleus decays from an excited state to a lower state. This process is in competition with the emission of conversion electrons and pair creation.
The energy of an emitted gamma ray equals the energy difference between the final and initial state minus the recoil energy given to the nucleus. The recoil effect is generally much smaller than the experimental uncertainty, and can thus usually be neglected [1].

A gamma ray carries an amount of angular momentum L. Considering conservation of angular momentum, L must take on a value between $I_i + I_f$ and $|I_i - I_f|$, where $I_{i,f}$ is the angular momentum of the initial and final states respectively.
A transition from an excited state to a state lower in energy, can be of an electric (E) or magnetic (M) type. The usual notation of a transition's multipolarity is EL or ML, and the multipole order is defined as 2^L. From relatively simple estimations, it can be concluded that transition rates are higher for lower multipolarities and for a given

multipole order, electric radiation is more likely than magnetic radiation [1]. For electric transitions, the parity π equals $(-1)^L$, while for magnetic transitions $\pi = (-1)^{L+1}$.

Gamma ray emission is in competition with internal conversion, where an atomic electron is sent out with an energy equal to the energy difference between the initial and final state minus the binding energy of the electron. The binding energy depends on the electron shell and can range from a few eV to a hundred keV. The vacancy left by the electron is rapidly filled by other electrons, emitting characteristic X-rays. The internal conversion coefficient α is the ratio of the probability for sending out converted electrons to gamma rays for a given transition.

1.3 Fission

Nuclear fission is a drastic decay process where a heavier parent nucleus splits into two smaller fragment nuclei. Fission results from the complex competition between the attractive nuclear- and repulsive Coulomb forces active in nuclei. The process is dictated by macroscopic (e.g. mean field) as well as microscopic (e.g. single particle, shell, pairing) effects [3].
A nucleus can undergo fission, when a state with energy E^* is populated that has the possibility to overcome the so-called fission barrier. The potential energy along the path towards fission is called the 'fission barrier' and is shown in figure 1.2 [4].

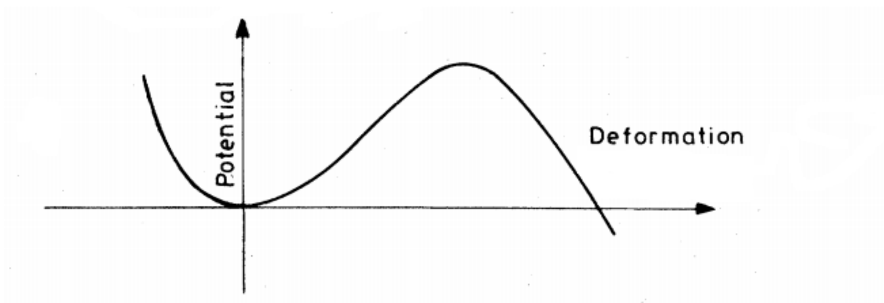

FIGURE 1.2: The potential energy along the minimum energy trajectory for increasing elongation. Figure from [5]

Fission is broadly classified either as high-energy fission or as low-energy fission, for which the excitation energy of the single compound nucleus either strongly exceeds or is either equal or comparable to the fission barrier respectively.

The advantage of studying low-energy fission is that the microscopic effects of fission are not washed out [3]. Low-energy fission processes include for instance spontaneous fission ($E^* = 0$), β-delayed fission ($E^* < Q_\beta$), Coulex-induced fission ($E^* \sim 11$ MeV, [6]) or fission induced by thermal neutrons ($E^* \sim$ several MeV).

1.3.1 Fission fragment mass distributions

Fission is said to be symmetric if the fragment mass distribution is peaked around the central $\sim A/2$ value, or asymmetric when the distribution shows a double-humped structure as result of the emission of a heavy and light fragment. This is schematically shown in figure 1.3.

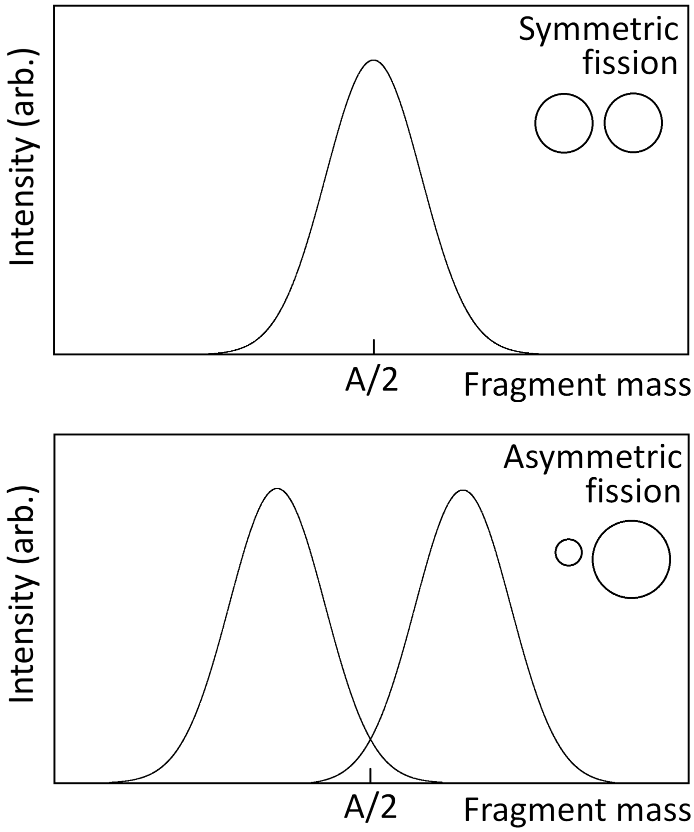

FIGURE 1.3: Symmetric and asymmetric fission fragment mass distributions for a fissioning parent nucleus with mass number A.

Fission asymmetry is found to be dominant in the uranium region. Shell effects of the doubly-magic $^{132}_{50}Sn_{82}$ nucleus are accounted for this result. Experimentally, the mass of the heavy fission fragment is observed to stay roughly constant, while the light fragment mass increases linearly with A as shown in figure 1.4.
The resulting mass distributions do not only depend on possible shell effects, but also on the excitation of the fissioning nucleus. At very high excitation energies (far above the fission barrier), fission is thought to be predominantly symmetric.

In 1986, Hulet et al. reported on a phenomenon they named 'bimodal fission', where at least two separate modes of fission are present [7]. These modes can involve two peaks in the kinetic energy distribution, symmetric and asymmetric fragment mass distributions and separate thresholds for the onset of asymmetric and symmetric fission [8]. These characteristics are also found in the fission analysis of ^{194,196}At, as is discussed in chapter 5.

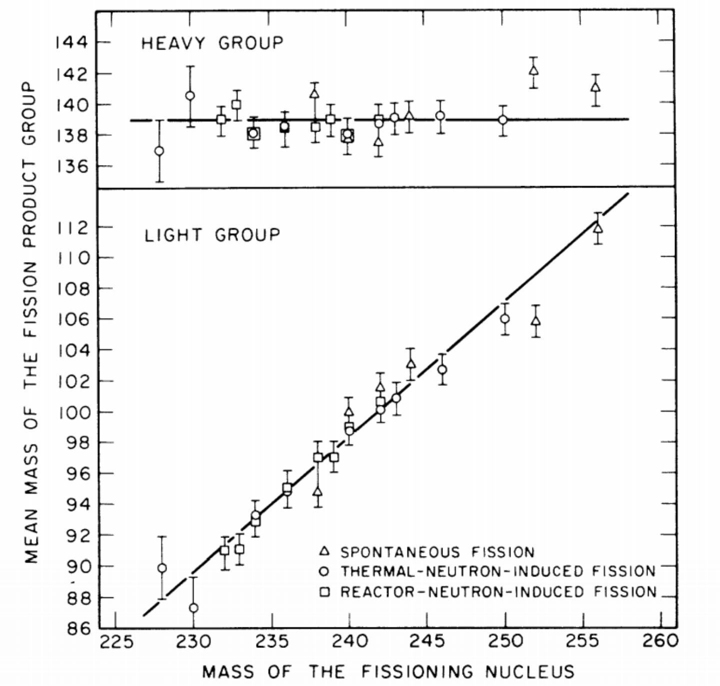

FIGURE 1.4: Average masses of light and heavy groups as function of the masses of the fissioning nucleus taken from [9]

1.3.2 Theoretical descriptions

During the last decades, several different theories were developed to describe fission. The first theories were based on the Liquid Drop Model(LDM), where the nucleus is considered in analogy to a charged liquid drop. In the LDM, the binding energy of the nucleus is described with the semi-empirical mass formula.

$$E = E_v + E_s + E_c + E_c + E_p = E_{LDM} + E_p \tag{1.9}$$

$E_{v,s,c,p}$ are the volume, surface, Coulomb and pairing energy terms respectively.
The surface and Coulomb terms are important to describe nuclear deformation. The energy difference related to deformation is then $E_{def} = E_s(\epsilon) + E_c(\epsilon) - E_s(0) - E_c(0)$, where ϵ is the eccentricity of an ellipsoid, which serves as a measure for the deviation from a spherical shape. If E_{def} is positive, the nucleus will be unstable against stretching. Eventually, two charge centers, separated by a neck, will be formed. The neck will finally rupture at the so-called scission point. The Coulomb interaction will then repel both fission fragments, resulting in a total kinetic energy (TKE) of approximately

$$U = \frac{kQ_1Q_2}{(r_1 + r_2)} \sim Z^2/A^{1/3} \tag{1.10}$$

U represents the potential energy, Q_i, r_i represent the nuclear charge and radius of fragment i. Z, A are the proton and mass numbers of the parent nucleus, and $k = 1/(4\pi\epsilon_0)$, as in usual electrostatics. This formula was derived simply by starting from the Coulomb potential energy of two touching charged spheres, using the relationship between a nuclear radius and mass number: $r = 1.2$ fm $.A^{1/3}$.

The LDM however has some shortcomings and can e.g. not explain the predominantly asymmetric fission of most actanides. Shell effects were accounted for several experimental results left unexplained by the LDM. In later developments on fission theory, Strutinsky developed a method to combine this previous picture with the shell structure of the nucleus and it's effects on the fission barrier [4].

Another, more recent, theoretical approach involves the construction of a potential energy surface (PES). This is a multidimensional map whereby the potential energy

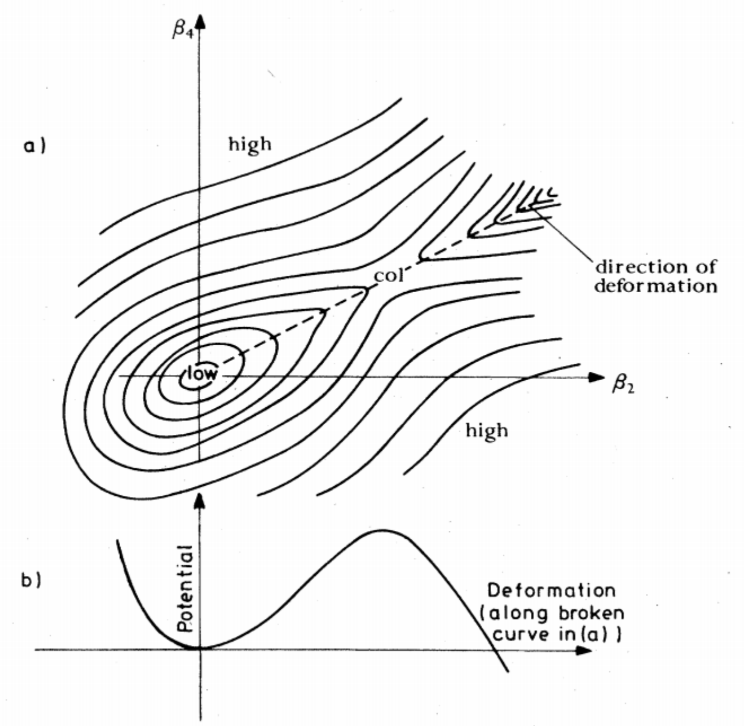

FIGURE 1.5: (a) potential energy contours as function of quardupole (β_2) and hexadecapole (β_4) deformation parameters, which are coefficients in Legendre polynomial of a liquid drop surface. (b) The potential energy along the minimum energy trajectory for increasing elongation. Figure from [5]. The barrier peak in (b) corresponds to the point marked as 'col' in (a).

is given for a certain nuclear deformation at different stages of the fission process. An example of such a PES is given in figure 1.6. The calculation of the deformation energy can yield an energy landscape consisting of different peaks, valleys, ridges, saddle points...
The fission barrier is then explained as being due to the increase of the potential energy along the path towards fission, as is shown in figure 1.5.

A fissioning nucleus starts from a given point on the PES. Before reaching the scission point, the nucleus 'passes through' this energy landscape and takes on different deformations. Two charge centers emerge and eventually, the nucleus splits into two fission fragments.

Möller et al. for instance introduced a five-dimensional deformation space, depending on five nuclear shape parameters: elongation, mass asymmetry, left fragment deformation, right fragment deformation and neck width [10]. The effect of these parameters on the nuclear shape can be seen in figure 1.6. This model makes use of a so-called

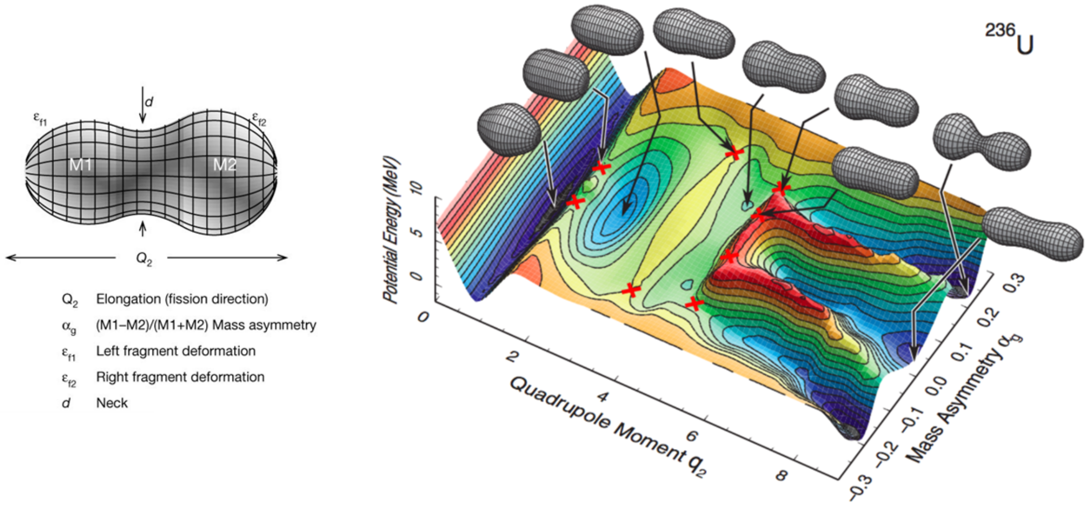

FIGURE 1.6: Left: Shape paramaters from [10]. Right: Example of a 2D projection of the 5D Potential Energy Surface(PES) for ^{236}U and nuclear shapes for different points on the PES, from [11].

immersion method to predict fission modes and fission fragment yields, by studying the behavior of imaginary 'water' on the PES [8].

1.3.3 β-delayed fission

1.3.3.1 β-delayed fission process and systematics

β-delayed fission is a two-step nuclear process. A parent nucleus undergoes β decay, populating the ground or excited states of the daughter nucleus. If these states are higher than or in vicinity of the fission barrier height B_f, there is a probability for fission to occur. In competition with fission, these excited states can also be depopulated via other mechanisms such as γ and/or particle emission.

Important to note is the fact that the energy of this excited state is limited by the Q value for β decay of the parent nuclide Q_β, which makes β-delayed fission an unique tool to study near- or even sub-barrier fission. Figure 1.7 shows a schematic representation of the βDF process for a nucleus where Q_β is slightly above B_f. Populated states above or near the barrier can have a reasonable fission probability. Sub-barrier states depend on quantum mechanical tunneling (dashed arrow lines) to undergo fission. On the right-hand side, the probability for fission with respect to excitation energy is shown in a qualitative way. It should be noted however that the β-feeding towards higher lying levels decreases rapidly due to a phase-space factor, roughly proportional to $(Q_{EC} - E)^5$ [12].

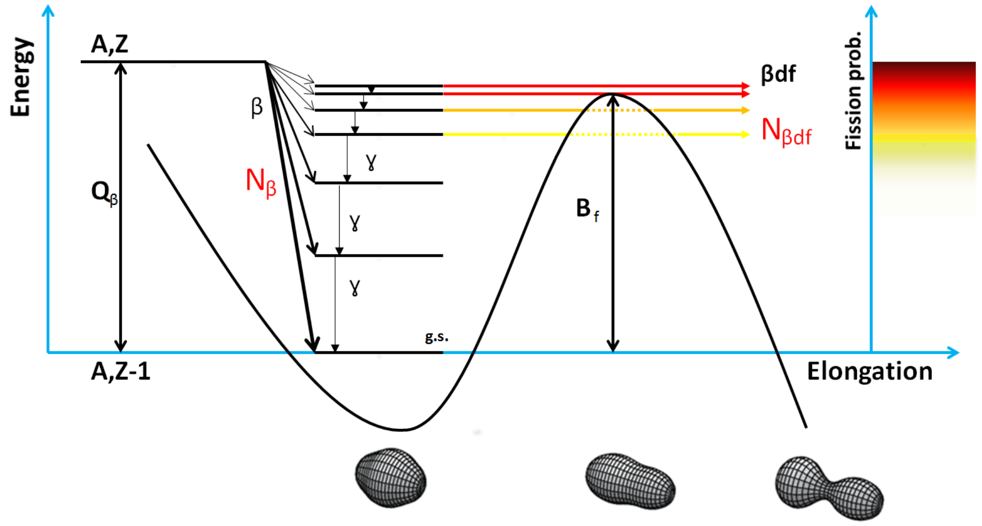

FIGURE 1.7: βDF on the neutron-deficient side of the chart of nuclei. Figure adjusted from [13]. In the color code that represents the fission probabilities, darker colors correspond to higher probabilities.

The probability for β-delayed fission P$_{\beta DF}$, of a given nucleus is defined as the number of fission events following the β decay of the parent nucleus ($N_{\beta DF}$), divided by the number of β decays (N_β). And theoretically, the formula is given by equation (1.11).

$$P_{\beta DF} = \frac{N_{\beta DF}}{N_\beta} = \frac{\int_0^{Q_{EC}} F(Q_{EC} - E) S_\beta(E) \frac{\Gamma_f(E)}{\Gamma_{tot}(E)} dE}{\int_0^{Q_{EC}} F(Q_{EC} - E) S_\beta(E) dE} \tag{1.11}$$

The P$_{\beta DF}$ value is thus influenced by Q_β, the β-strength function S_β, the fission barrier height of the daughter and the competition between fission and de-excitation of the excited states [3]. S_β determines the population of the excited states in the daughter nucleus. $F(Q_\beta - E)$ is the statistical Fermi function and $\Gamma_{tot,f}$ are the total and fission decay widths respectively. As suggested by [3], the partial βDF half-life, $T_{1/2p,\beta DF}$, defined in equation (1.12), can be compared to systematic trends and provides some advantage over the use of P$_{\beta DF}$, especially in cases where the β branching b_β is small and hard to determine experimentally.

$$T_{1/2p,\beta DF} = \frac{T_{1/2,tot}}{b_\beta \times P_{\beta DF}} = \frac{T_{1/2,tot}}{\int_0^{Q_{EC}} F(Q_{EC} - E) S_\beta(E) \frac{\Gamma_f(E)}{\Gamma_{tot}(E)} dE} \tag{1.12}$$

A linear trend for $P_{\beta DF}$ in function of Q_{EC} was found by Shaughnessy et al. in [14]. In the βDF review paper of Andreyev et al. [3], this trend was acknowledged and new data for Tl isotopes was added. Here the partial βDF half-life, $T_{1/2p,\beta DF}$, was presented instead of $P_{\beta DF}$. The Tl partial half-lives are situated on a shifted line with a similar slope with respect to the trans-uranium data.
It is expected, that occurence of βDF strongly depends on the *difference* $Q_{EC} - B_f$ instead of solely, Q_{EC}. Therefore, $T_{1/2p,\beta DF}$ is shown in function of this difference. The plots were produced for two different models in [3] and are shown in figure 1.8.

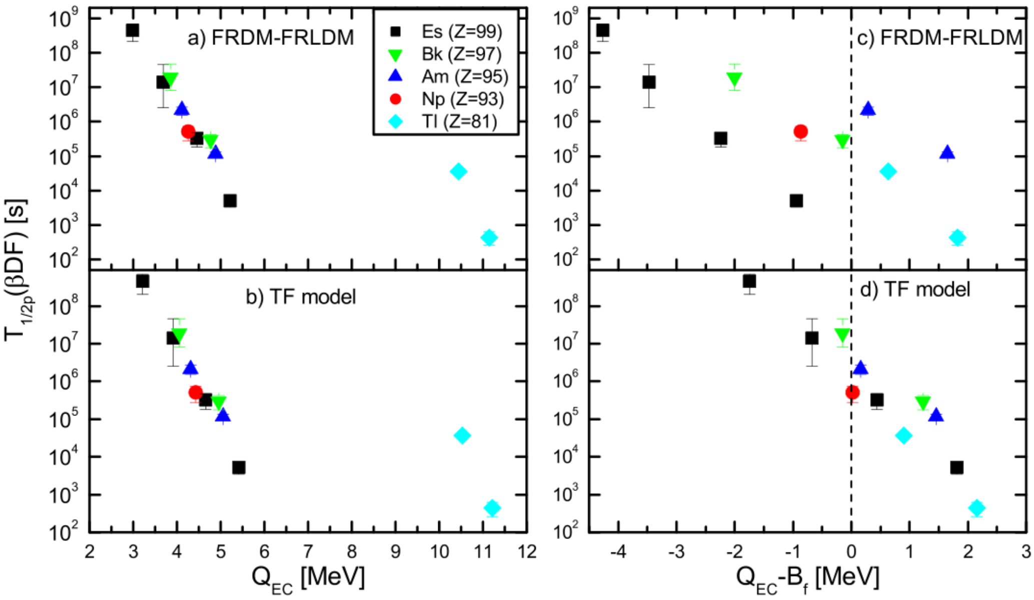

FIGURE 1.8: $T_{1/2p,\beta DF}$ in function of Q_{EC} (left) and $Q_{EC} - B_f$(right), taken from [3].

The total kinetic energy (TKE) released in fission of ^{194,196}Po, studied via βDF of ^{194,196}At can be compared to Viola systematics. Viola suggested in 1966 a linear relationship between TKE release in fission and $Z^2/A^{1/3}$. This last parameter is the Coulomb parameter of a fissioning nucleus and is related to the coulomb repulsion of two charged spheroid fission fragments (see also eq.(1.10). After collection of more fission data, this linear trend was reevaluated in 1984 to be $TKE = 0.1189 Z^2/A^{1/3} + 7.3$ MeV [15]. The so-called viola-plot is shown in figure 1.9.

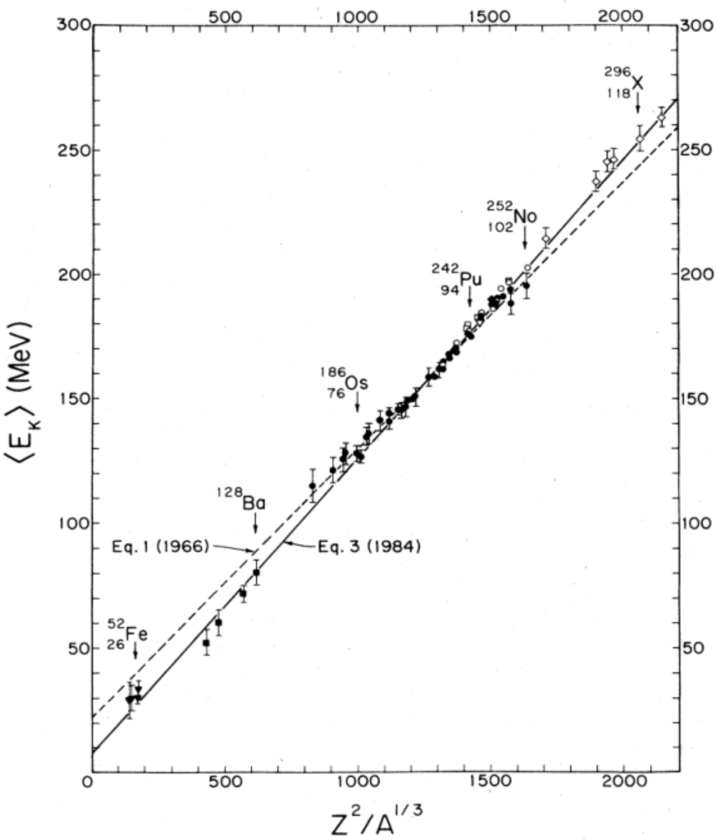

FIGURE 1.9: Total kinetic energy (TKE) release systematics in fission. TKE, here denoted as $< E_k >$, is shown versus the Coulomb parameter $Z^2/A^{1/3}$. Plot taken from [15]

1.3.3.2 Regions of occurrence

So far, only two regions where βDF occurs have been identified. These are the uranium and neutron-deficient lead regions, indicated by black shapes in figure 1.10. βDF is also expected to happen in the region of neutron-rich super heavy nuclei, which is currently experimentally unaccessible. Here, it might be that βDF plays an important roll in the so-called r-process [16].

A βDF branch, detectable with present-day instrumentation, requires a non-negligible β decay branch b_β and β-feeding to excited states with an energy higher than or comparable to the fission barrier B_f of the daughter nucleus. In literature, $b_\beta > 1\%$ and $Q_{EC} \gtrsim B_f - 2$ MeV has been quoted as rule of thumb to fulfill these requirements [3],[13],[8].

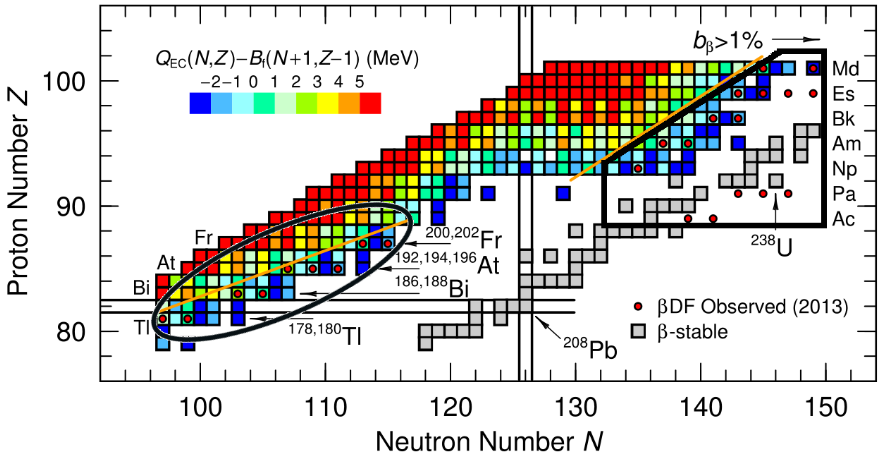

FIGURE 1.10: $Q - B_f$ values for nuclei where βDF might be expected. Figure adjusted from[3].

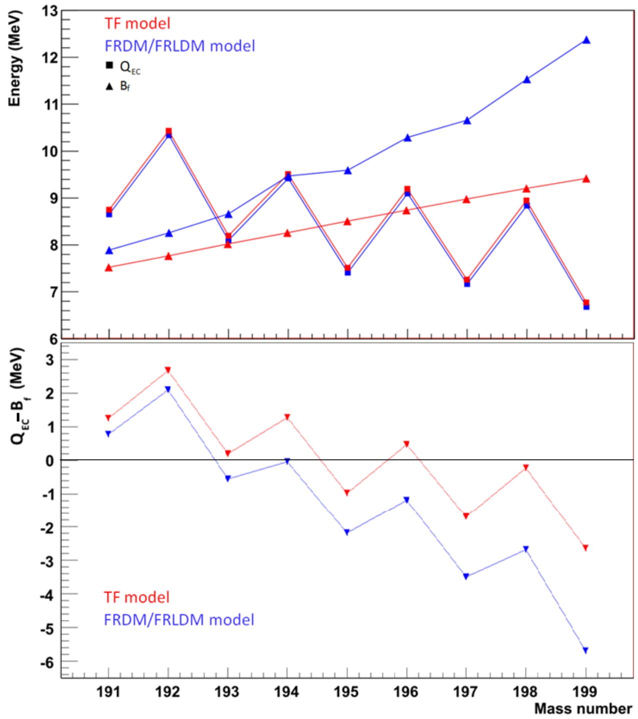

FIGURE 1.11: Top: $Q_{EC}(^{196}\text{At})$ and $B_f(^{196}\text{Po})$ compared for TF and FRDM/FRLDM models.
Bottom: $Q_{EC}(^{196}\text{At})$ - $B_f(^{196}\text{Po})$ for TF and FRDM/FRLDM models.

In figure 1.11, the $Q_{EC}(At)$ and $B_f(Po)$ values for the parent-daughter decay system At-Po, studied in this thesis, are shown. Red points are calculated using the Finite Range Droplet Model (FRDM) and the Finite Range Liquid Drop Model (FRDLM) for Q_{EC} and B_f values respectively [17],[8]. Blue markers denote calculations from the Thomas-Fermi (TF) model for atomic masses and fission barriers [18], [19].

1.4 Decay of ^{194,196}At

Astatine (At), the element studied in this thesis, is the rarest naturally occurring element on earth [20]. At is of interest for several different fields of science (e.g cancer treatment in medicine, nuclear structure studies and β-delayed fission in nuclear physics). The (simplified) decay of ^{194,196}At and it's daughters is shown in figure 1.12 and will be discussed more deeply throughout this thesis. No α decay fine structure, feeding to excited states or γ decay is depicted here.

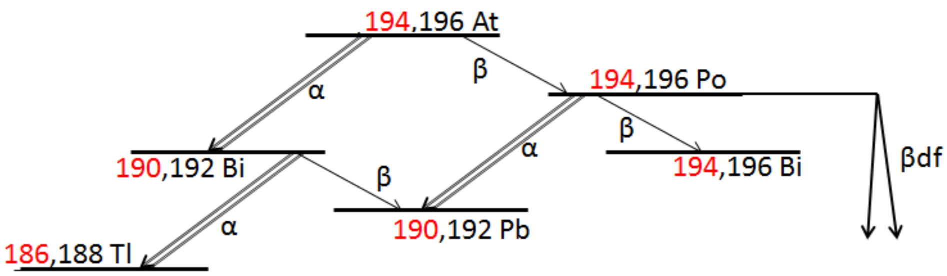

FIGURE 1.12: Decay of ^{194,196}At.

For the decay of ^{196}At, prior to this work, only one α line with energy 7049(3) keV was known. The half-life that was quoted in [2] was 0.388(14)s, and the β branch b_β of ∼4.9 % was calculated from systematics. The spin and parity of the ground state is thought to be (3^+), which is deduced from systematics of odd-odd nuclei in the region of At. A short-living isomeric state with a mean lifetime of τ=11(2) μs with spin and parity (5^+) at an energy of 157,9(1) keV was proposed in [21].
For ^{194}At, two isomers ((3^+) and (10^-), both from systematics) with half-lives of ∼0,040 s and ∼0,250 s respectively are known and quoted on [2]. The β branch for both isomers is unknown. The energy of the α decay of ^{194}At is measured to be 7200(20) keV and ∼7140 keV for the 0,250 and 0,040 s isomers respectively.

Chapter 2

Motivation

2.1 βDF of At

β-delayed fission is a unique tool to study low-energy fission for exotic nuclei, where the excitation energy of the fissioning states can be comparable to, or even below the fission barrier. As mentioned in section 1.3, fission is a process that is subject to the interplay of macroscopic (collective) and microscopic (e.g. shell effects, pairing,..) effects. In low-energy fission, the microscopic effects might not be negligible, since they are not 'washed out' as is the case in high-energy fission. The shape of the PES is of extreme importance to the fission behavior of a nucleus that undergoes low-energy fission, as suggested by [22]. It is by studying this fission behavior, by measuring the fission fragment mass and the total kinetic energy distributions, that fission theory can be compared to experiment.

The recently discovered unexpected fission behavior of ^{180}Hg, following the β decay of ^{180}Tl, has increased interest in experimentally probing fission properties over an extended nuclear chart region [12], [23], [24].
βDF of ^{180}Tl showed an unexpected asymmetric fission fragment mass distribution. It was first anticipated that ^{180}Hg would fission in two ^{90}Zr isotopes, having a magic N=50 and semi-magic Z=40 configuration. Experiment showed however, that the resulting fragment masses were centered around A=100 and A=80, being ^{100}Ru and ^{80}Kr assuming the N/Z ratio is similar in both fission fragments [22], [13]. The resulting fission fragment mass and total kinetic energy distribution is shown in figure 2.1. This asymmetric fission can thus not be explained solely via shell-effects, as is the case in

trans-uranium region of asymmetric fission. Here shell effects from the doubly-magic ^{132}Sn are thought to cause fission asymmetry. This striking feature triggers an interest to study fission properties of other isotopes in the neutron-deficient lead region. Theorists have attempted to explain this unexpected fission behavior of ^{180}Hg ([12], [25], [26]), and it would be interesting to compare more experimental data for low-energy fission in the lead region to theoretical predictions. βDF is an excellent tool for this purpose.

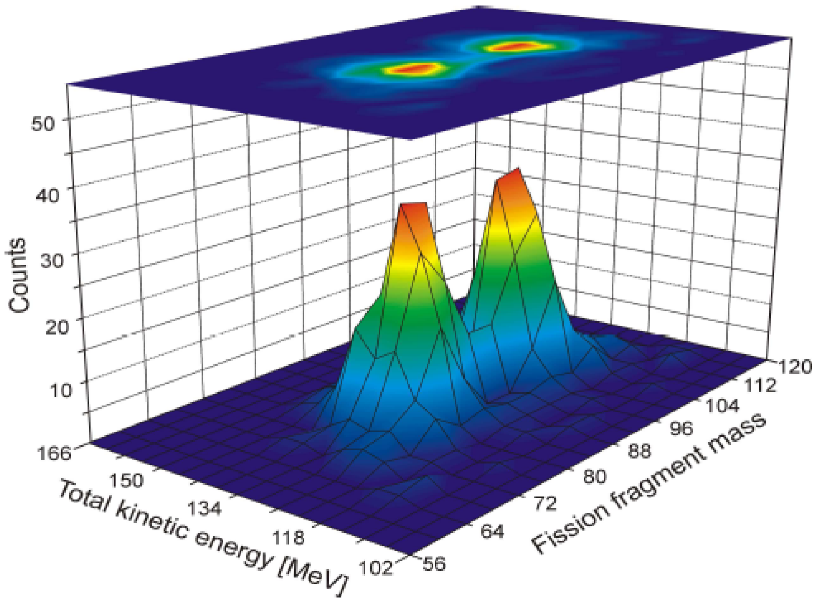

FIGURE 2.1: Unexpected asymmetric fragment mass and kinetic energy distributions of ^{180}Hg following β decay of ^{180}Tl, figure from [22]

Low-energy fission behavior can be roughly mapped on the nuclear chart into regions of predominantly (a)symmetric fission, as is shown in figure 2.2. The heavy actanides fission mostly asymmetric, while symmetric fission dominates in the pre-actanides. These regions are indicated on figure 2.2

Recent β-delayed fission experiments on ^{178,180}Tl have firmly established a new region of asymmetric fission on the nuclear chart [3], [27]. This implies a transition region from asymmetry to symmetry in the vicinity of the neutron-deficient Po isotopes, which are investigated in this thesis via the βDF of ^{194,196}At.

Studying different fission regions of the nuclear chart also allows the fission studies for different N/Z values. For the trans-uranium region, N/Z ~1.55, while the neutron-deficient lead region has a N/Z value of ~1.3. Comparison of fission properties might help to better predict fission behavior in experimentally inaccessible regions of the nuclear chart.

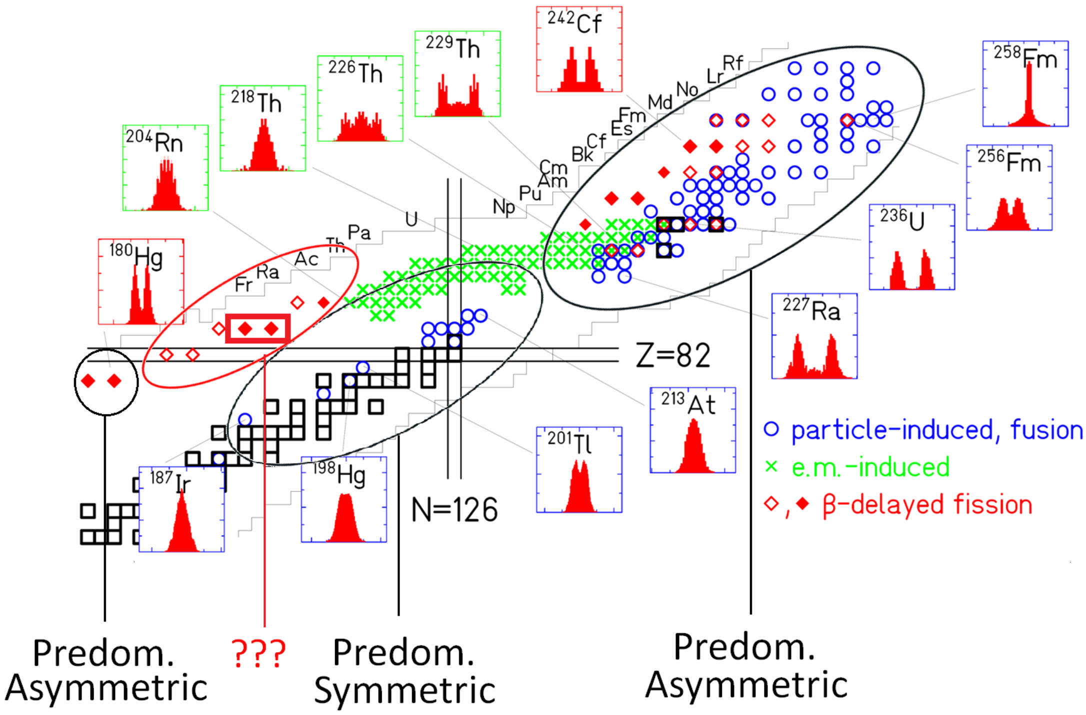

FIGURE 2.2: Nuclear chart showing different regions of predominantly (a)symmetric low energy fission. The red ellipse is yet unexplored and contains the ^{194,196}Po isotopes (red box), studied in this thesis via βDF of ^{194,196}At. Figure adjusted from [3].

In order to measure the probability for βDF, $P_{\beta DF}$, a reliable value for the β branch of the parent nucleus is required, in this thesis, this was done by comparing the amount of alpha decays of the daughter to the amount of alpha decays of the parent. This is explained deeper in the analysis chapters of this work. If isomers are present, it could in principle be that these show different fission behavior or it could be that only one of them undergoes βDF. The presence or absence of multiple isomeric states was investigated via α decay spectroscopy.

2.2 α-decay spectroscopy

Moreover, the study of α decay and α-γ coincidences for At and it's decay products also provides information on the previously unknown decay scheme of ^{192}Bi, populated trough α decay of ^{196}At. The investigation of low-lying energy levels in the daughter nucleus may indicate shape coexistence. This phenomenon, as found in ^{186}Pb [28] ($Z = 82$), is the presence of different nuclear shapes at low-lying excitation levels having the same spins and parities. Its origin is still under debate and more experimental information is thus needed [24]. Half-lives of produced isotopes can also be determined using the observed time-structure of the α decay.

2.3 Further studies on At

Besides studying βDF, At is also of interest to other nuclear structure studies and even different fields of science. For example, cancer treatments using ^{211}At have shown promising results [29].

In additions, laser spectroscopy experiments on At, allowing the investigation of its ground-state properties, have been conducted and are currently being analyzed. By measuring the hyperfine structure and isotope shifts for a wide range of At isotopes, magnetic and quadrupole moments, spins, charge radii and deformations will be deduced. These quantities measured for At will be compared to the previously studied isotope chains in the $Z = 82$ region (Au, Hg, Pb, Bi, Po, Rn, Fr) [24]. Reflection asymmetric octupole collective behaviour for neutron-rich Rn isotopes has recently been found using Coulomb excitation [30]. Heavy At isotopes might exhibit similar behavior. An odd-even staggering trend in the charge radii could indicate such a stable octupole deformation [24].

Chapter 3

Experiment

The βDF experiments of At were conducted in ISOLDE, CERN in May 2011 and May 2012. In this chapter, the ISOLDE (Isotope Separation On-Line DEvice) facility, production of the At ion beam and detection system are discussed.

3.1 ISOLDE

The on-line mass separator ISOLDE, located at CERN (European Centre for Nuclear Research), is a facility offering a large variety of radioactive ion beams for studies in different fields such as nuclear, atomic and solid state physics, material and life science [31]. A schematical overview of the ISOLDE facility is given in figure 3.1.

ISOLDE receives 1.4 GeV proton pulses (PP) coming from the Proton Synchrotron Booster (PSB), a stack of four smaller synchrotrons. These proton bunches, having a length of 2.4 μs each and separated in time by 1.2 s, are first accelerated in a linear accelerator (linac 2) up to an energy of 50 MeV before entering the PSB. When protons leave the PSB, they can either be transported to ISOLDE, other CERN facilities or further accelerated in the CERN accelerator complex.
This division is arranged in super cycles (SC), consisting of at most 42 different proton pulses.
In ISOLDE, the protons impinge on a solid or liquid target, where a wide range of isotopes is produced by fission, spallation or fragmentation. The target is kept at very

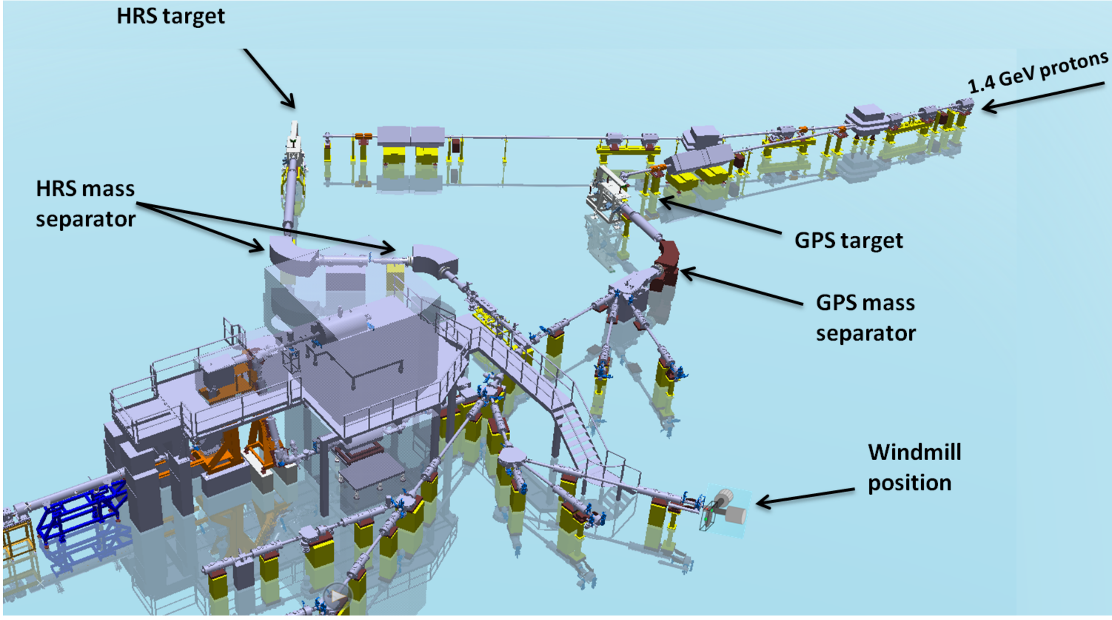

FIGURE 3.1: Layout of the ISOLDE facility located at CERN, Geneva [31]

high temperatures (∼2000 °C) to reduce diffusion, desorption and effusion times of the produced elements out of the target. Also the transfer line is kept at a high temperature to avoid lingering of the atoms to the walls of the line [32]. From this mixture of produced atoms, only the isotope of interest is extracted. Via selective ionization and mass separation. The ionization mechanism can either be surface ionization, electron impact ionization or resonant laser ionization. The choice of technique, depends heavily on the ionization potential and the production rate for a given element.
After ionizing the element of interest, the ions are extracted with extraction electrodes and sent to one of the two mass separators in ISOLDE. These are the General Purpose Separator (GPS) and the High Resolution Separator(HRS).
During the At β-delayed fission experiments, uranium carbide (UC_x) was used as target material and At, mostly produced via spallation, was ionized via a resonant laser scheme, discussed in section 3.1.1. The experiment in May 2011 employed HRS, while GPS was used in May 2012. After mass separation the ions were led to the Windmill chamber, which is further discussed in section 3.2.

3.1.1 Laser Ionisation

In order to form an isotopically pure beam, the extraction of a given element has to be very selective. As mentioned before, At isotopes were ionized by shining resonantly

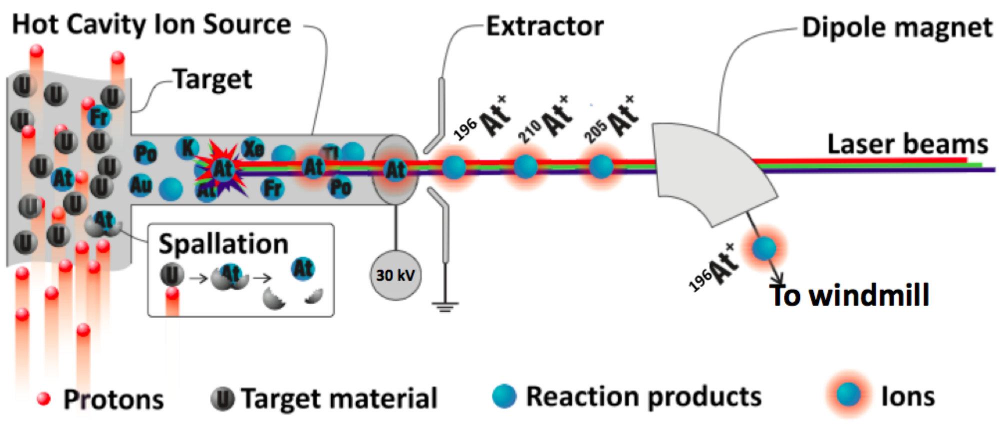

FIGURE 3.2: Creation, ionization, extraction and mass-separation of ^{196}At, figure adjusted from [20]

tuned laser light onto the atoms. By precisely tuning the ISOLDE RILIS lasers, At atoms are stepwise excited and eventually ionized using atomic transitions.
In a recent study, an efficient ionization scheme was developed yielding an ion current of up to 150 pA/μC for ^{205}At [20]. This three-step photoionization scheme is given in figure 3.3.

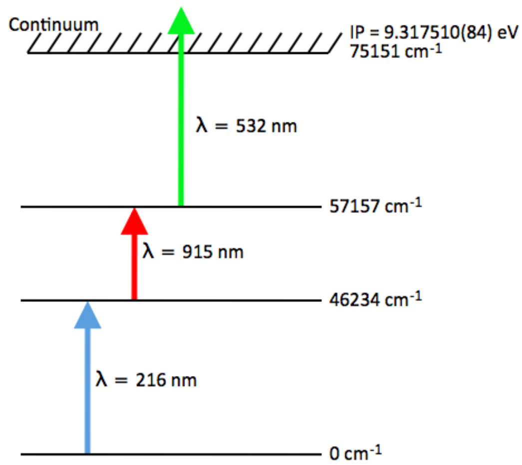

FIGURE 3.3: The used ionization scheme for At. The cited levels, wavelengths and ionization potential(IP) were taken from [20].

First-step excitation was obtained by tuning a dye laser to a fundamental frequency of 15411,2 cm^{-1}, which was then frequency tripled. The second step was reached by tuning a dye laser to 10923,5 cm^{-1}. Finally, a frequency-doubled Nd:YAG laser provided 532 nm light in order to excite electrons to the continuum.

3.1.2 Mass separation

In order to select the isotope of interest, produced ions are extracted with an extraction electrode at 20 to 60 kV voltage and sent through a mass separator. As mentioned, two mass separators are present, namely GPS and HRS. They have a mass resolving power ($\Delta M/M$) of about 2400 and 5000 respectively.

These mass separators consist of 1 (GPS) and 2 (HRS) dipole analyzing magnets, which are also shown in figure 3.1. HRS allows for one beam to be extracted and sent to an experimental setup via the central beam line. GPS is designed to offer the possibility of beam sharing. Different masses are available at the same time in the focal plane of the separator and three beams can be delivered to different setups via the central, low and high mass beam lines [31]. Beam sharing might be useful, since high production cross sections for a series of isotopes can be obtained, resulting in intense beams at several masses [32].

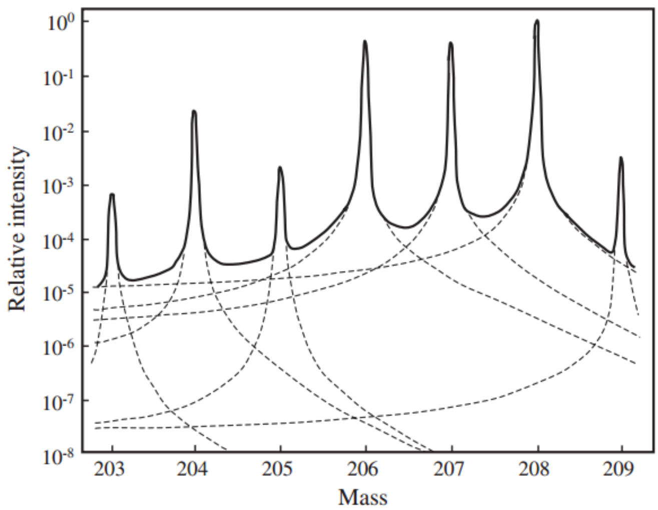

FIGURE 3.4: Spectrum of an ion beam obtained after mass separation taken from [32].

Even after mass separation, contaminants can be present in the ion beam. When ions are extracted and transported through beam lines, collisions with rest gas cause a spread in energy and directional changes to occur. These 'disturbances' are responsible for a relatively small amount of neighboring masses to be present in the ion beam after mass separation, even when the mass resolution is very good [32]. Furthermore, the separated beam can also contain isobaric contaminants from surface-ionized elements, such as for instance Fr or Tl, which are produced at much higher rates [33].

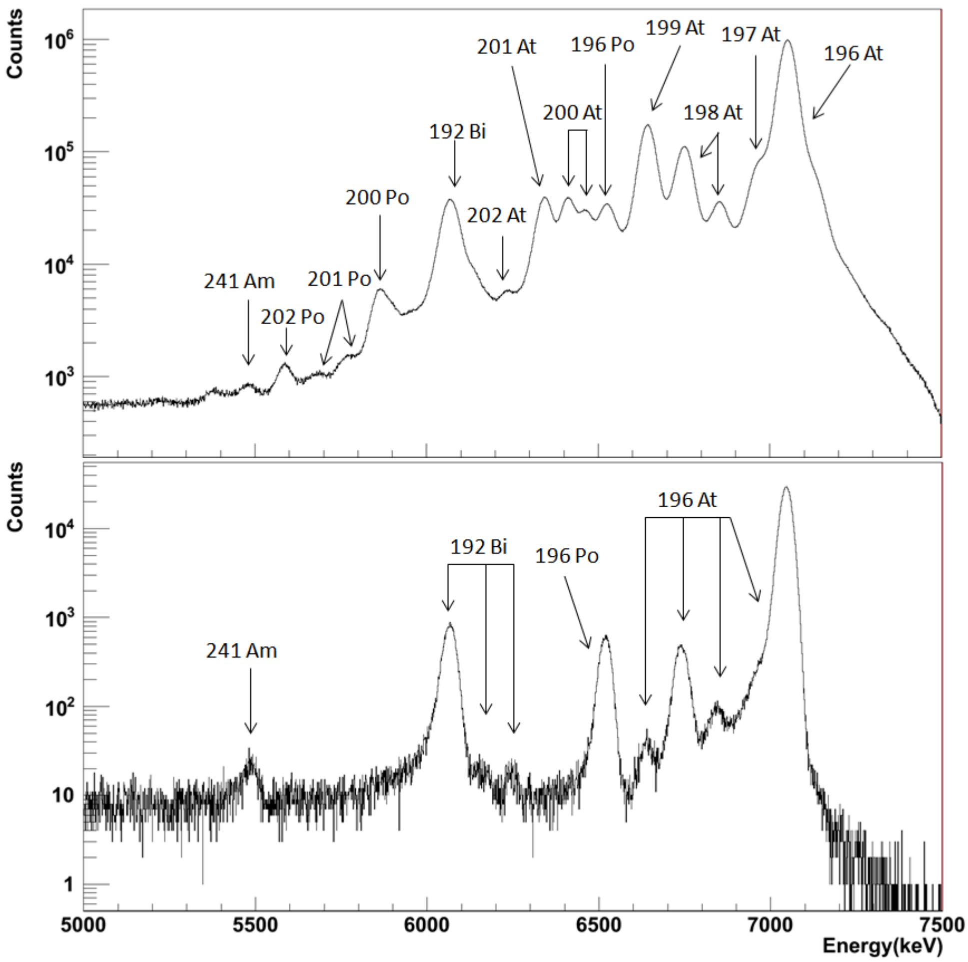

FIGURE 3.5: Energy spectrum in alpha range for GPS(above) and HRS(below) taken in May 2012 and May 2011 respectively.

In figure 3.5, the α spectrum taken with GPS for this experiment shows many contaminants in comparison to the spectrum taken with HRS. The HRS beam was pure: only ^{196}At and its decay products ^{196}Po and ^{192}Bi were present in the α spectrum, while the GPS beam contained many different masses, ranging from ^{196}At to ^{202}At. This spectrum dissimilarity is partly attributed to the difference in resolving power for GPS and HRS, but is also due to the fact that HRS consists of 2 bending magnets. Neighboring 'mass tails' due to gas collisions which can pass the first magnet, will be purified further by the second magnet.

3.2 Windmill system

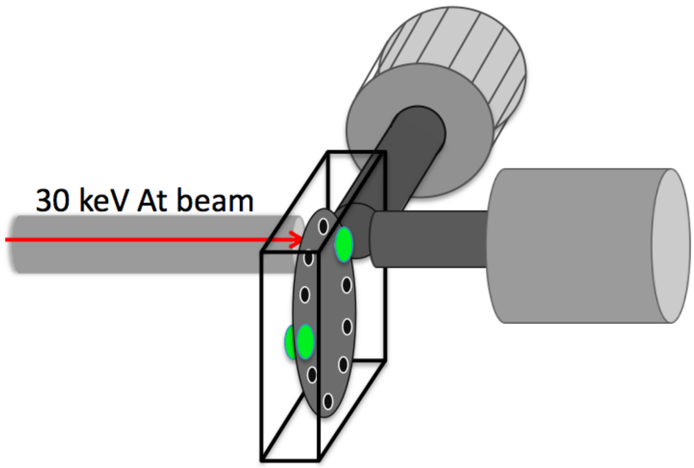

FIGURE 3.6: Experimental setup showing the windmill with rotating wheel and carbon foils(black). Also the Ge(grey) and Si(green) detectors are shown.

In order to measure fission fragments and alpha particles coming from the decay of At, the Windmill (WM) detection setup was used. The Windmill system, shown schematically in figure 3.7, is a vacuum chamber reaching pressures in the order of 10^{-6} mbar, in which a rotating wheel is mounted. The ISOLDE beam is implanted in a set of 10 carbon foils (20 $\mu g/cm^2$ or 888 Å thick) embedded in the wheel.
Four silicon detectors are placed in two different observatory stations around the wheel. The implantation station consists of an annular detector, through which the beam passes, and a (full) surface barrier detector on the backside of the wheel. The decay station consists of two silicon PIPS detectors placed on either side of the wheel and is separated by the implantation station with an angle of 144° with respect to the wheel center.
The wheel can be rotated from the implantation station to the decay station by a step motor. The beam is implanted in a carbon foil for the duration of one supercycle before it is turned. The remaining longer-lived radioactivity can than be observed at the decay station for the duration of another supercycle before the wheel is turned again. In both experiments, the supercycle had a duration of 42 s, thus consisting of 35 proton pulses.

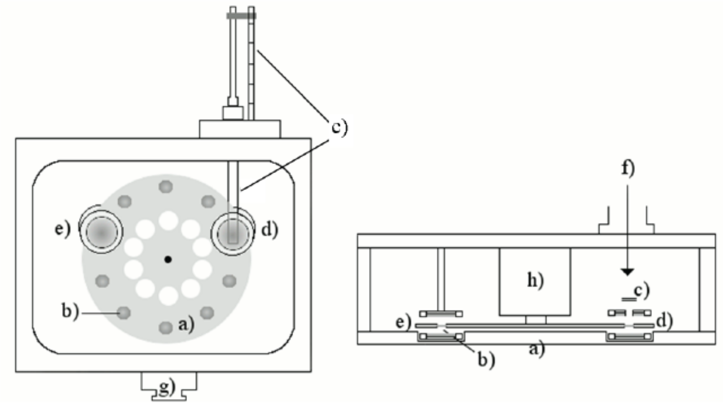

FIGURE 3.7: The Windmill system: front view(left) and top view(right) showing (a) rotating wheel, (b) carbon foil, (c) current measurement and collimator, (d) implantation station (with two silicon detectors), (e) decay station (with two silicon detectors), (f) separator beam, (g) vacuum pump hole, (h) step motor. Figure from [34]

3.3 Detectors

The detectors used to measure the radioactive decay of At, it's daughters and some possible other mass contaminants were positioned inside (Si detectors) as well as outside (Ge detectors) the Windmill, as shown in figure 3.6.

3.3.1 Silicon detectors

Most silicon detectors are based on a junction of p-type and n-type material. The diffusion of electrons and holes to either side of the junction and the recombination of these charge carriers leaves positively charged ions on the n-type side and negatively charged ions on the p-type side. This configuration results in what is called a 'depletion layer'. The thickness of this layer, which is the sensitive part of the detector, can be greatly enlarged by applying a reverse-bias voltage over the Si crystal.
Electron-hole pairs created in the depletion region, are collected by the electric field that is present inside the material, thus causing a measurable signal. An important feature is that the energy of the incident radiation on the material is proportional to the amount of electron-hole pairs created, and thus to the recorded pulse height [35].
Surface barrier detectors are fabricated by evaporating a thin layer of gold and aluminium, which act as an electric contact onto the silicon material.[36].

Passivated Implanted Planar Silicon (PIPS) detectors on the other hand, make use of implanted electrical contacts and are characterized by their very low leakage currents in comparison to surface barrier detectors [35].

The detectors inside the windmill, were four silicon detectors grouped in two observatory stations: an implantation and a decay station.
At the implantation site, schematically shown in figure 3.8, an annular and a full silicon surface barrier detector, both made bij Ortec [36], were placed at either side of the rotating wheel. The annular detector has an active area of 450 mm^2 ($\sim$ 24 mm $\oslash$), including the hole of 6 mm in diameter through which the beam passes. It was placed at a distance of 7 mm from the foil. The solid angle covered by the annular detector is 20% of 4π. The Full Width at Half Maximum (FWHM) of the annular detector for a typical α line was $\sim$ 40 keV in May 2011, while in May 2012, the resolution was $\sim$ 50 keV.
The full surface barrier detector at the backside of the wheel has an active area of 300 mm^2 ($\sim$ 19,5 mm $\oslash$), and was placed at a distance of 4 mm from the carbon foil, resulting in a solid-angle coverage of 31%. The FWHM of α lines was $\sim$ 35 keV for this detector during the run in May 2011, and $\sim$ 60 keV in 2012.
When referring to one of these two detectors in this thesis, Si1 and Si2 will be used to denote the annular and full surface barrier detectors respectively. Detector serial numbers can also be found in table 3.1.

Two Passivated Implanted Planar Silicon (PIPS) detectors from Canberra [37] were placed at the decay station at either side of the rotating wheel. Both detectors have an active area of 300 mm^2, showed a FWHM of $\sim$ 38 keV for α decay lines. The PIPS detector placed on the same side of the wheel as the full surface barrier detector(Si2), will be referred to as Si3, while the PIPS detector placed on the same side as the annular detector(Si1) will be referred to as Si4. A figure showing all detector names is presented in figure 3.9.

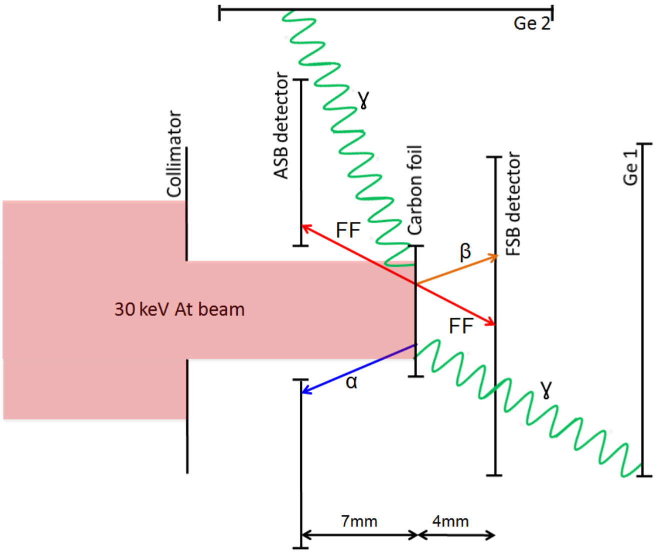

FIGURE 3.8: Schematical top view of the implantation station. The anullar (ASB) and full (FSB) surface barrier detectors and both Ge detectors are shown. Different types of radiation stopped in the detectors is also shown.

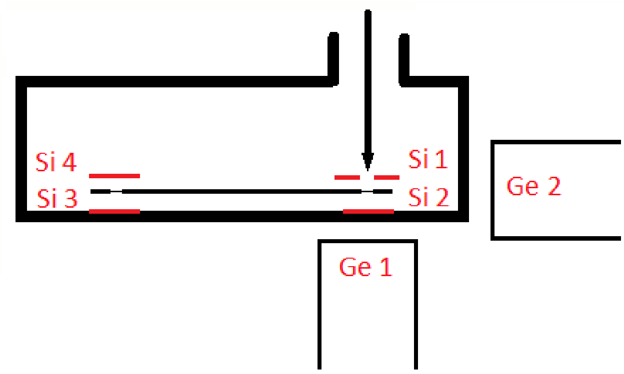

FIGURE 3.9: Schematical top view of the implantation station. Names used to denote different detectors in this thesis are shown.

Detector	Serial number
Si1	43-051F
Si2	41-038D
Si3	74256
Si4	74257

TABLE 3.1: Silicon detector serial numbers.

3.3.1.1 Pulse height defect

A very important concept to adress when using silicon semiconductor detectors for heavy ion spectroscopy is the so-called Pulse height defect(PHD). A heavy ion with a given energy, incident on the detector will give rise to a smaller pulse height as

compared to a light ion with the same energy would.
The PHD is defined as the difference between the true energy of the heavy ion and the apparant energy for an alpha calibration [35]. Different effects contribute to the total PHD. On the one hand, the window defect is caused by radiation depositing energy in non-sensitve areas of the detector. On the other hand, non-ionizing atomic collisions and charge carrier recombination in the sensitive layer of the detector also result in a lower pulse height. [38]. The larger recombination rate of electron-hole pairs for heavy ions is due to dense plasma of charge carreirs that surrounds an ion track inside the detector. This plasma locally reduces the effective electric field, causing longer collection times and thus a larger recombination probability [38].
When measuring the incoming energy of a heavy ion (e.g. fission fragments), one has to acknowledge this PHD and correct for it. Calibration measurements on the Windmill detectors, performed at the Lohengrin spectrometer at ILL, allow to correct for this effect.

3.3.2 Germanium detectors

During the run in May 2011, two High-Purity Germanium (HPGe) detectors from Canberra [37] were positioned at the side of the windmill as shown in figure 3.6. When a γ ray enters a Ge crystal, it creates electron-hole pairs. The amount of created pairs is proportional to the energy deposited in the material. The collection of the electron-hole pairs is realized by setting up an electric field in the crystal. This allowed energy measurements of γ rays, allowing to construct α-γ and γ-γ coincidences. The HPGe placed parallel to the beam direction is a coaxial detector with a relative efficiency of 90%. By convention, HPGe detectors are characterized by "relative efficiency". Relative efficiency is defined as the efficiency of a point ^{60}Co source at 25 cm from the face of a standard 3-inch x 3-inch right circular cylinder NaI(Tl) detector [36].
The HPGe detector placed perpendicular to the beam direction is a coaxial HPGe with a relative efficiency of 70%. The 90% and 70% HPGe both showed a FWHM of ~2.4 keV at a γ-ray energy of 1.3 MeV. In order to reduce thermal noise, HPGe detectors have to be cooled with liquid nitrogen.
Because of a large dead time it was impossible to properly operate the HPGe detectors during the experiment of 2012 and they were thus disconnected. The large dead time was probably due to the large amount of contamination present in the beam (section 3.1.2), causing the amount of emitted γ rays to be much higher than the in 2011.

Chapter 4

Alpha decay spectroscopy of ^{196}At

This chapter will deal with α decay spectroscopy of ^{196}At. Mostly, data collected during the run of May 2011 will be discussed. The purity of the beam allows a study of the (previously unknown) fine structure of ^{196}At. The presence of both Si and HPGe detectors, as discussed in chapter 3, make it possible to identify unknown low-lying states in ^{192}Bi, via α-γ coincidences with the fine structure of ^{196}At.
A preliminary level scheme for ^{192}Bi is given. The β branch (b_β) is also calculated from the data and half-life values for ^{196}At, ^{196}Po and ^{192}Bi are studied and compared to literature.

4.1 Data

The Si detectors were energy calibrated using known α lines of ^{196}At,^{196}Po and ^{192}Bi , present in the spectrum. The HPGe detectors were energy calibrated with known γ lines, coming from different radioactive sources placed in front of the detectors before the start of the At measurements. Both HPGe detectors were also calibrated for efficiency by using several radioactive sources.

In figure 4.1, the energy spectrum (0-90 MeV) taken in May 2011 (top) and May 2012(bottom) for Si2 is shown, since here the different types of particles, characterized by the different amount of energy deposited in the detector are very clear. The different particles as well as summing effects are named.
Electrons are found at low energies, α particles are situated in a range of $\sim$ 5 MeV

- 7 MeV, while fission fragments deposit energies between 50 and 85 MeV. A count in double or triple α sum peaks arises when two or three α particles enter the silicon detector at a time difference which is too short for the integration time of the detector signal to separate. Those two or three particles are then 'mistakenly' accounted for as a single event having an energy equal to the sum of the separate particle energies.

The large number of electrons in this spectrum does not only come from the decay of At and it's daughters, but also from (isobaric) mass contaminants present in the beam, which can for instance be surface ionized and are possibly produced with rates several orders of magnitude higher than At, such as e.g. Tl [33].

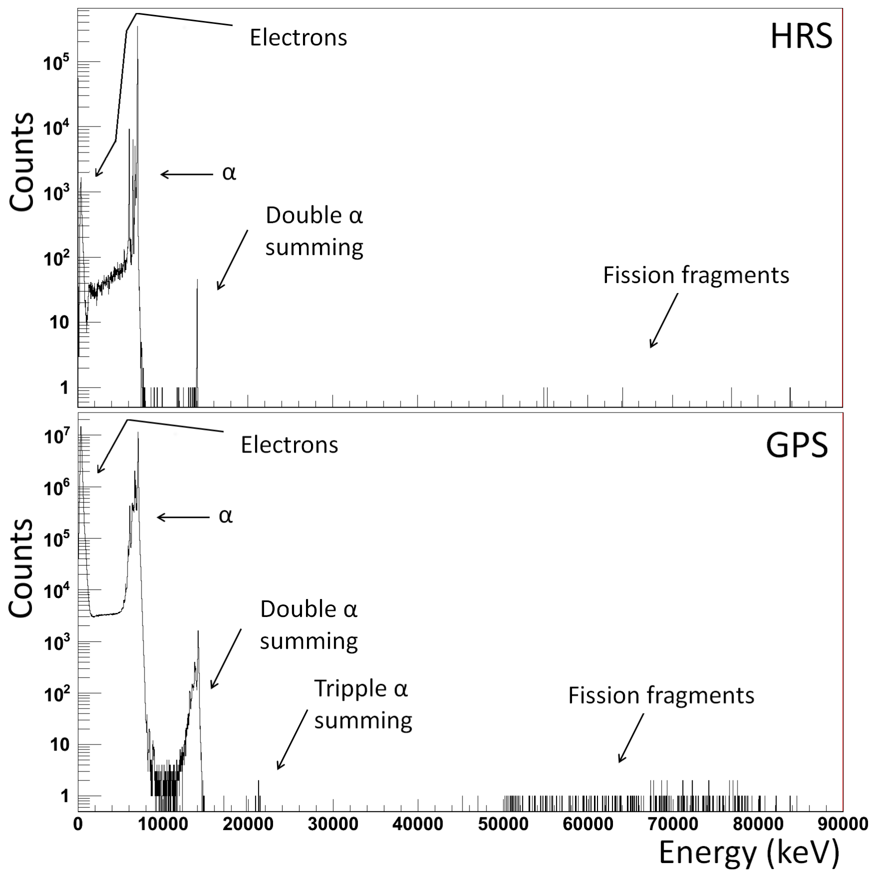

FIGURE 4.1: Energy spectrum for full surface barrier detector (Si2). Data from May 2012 with HRS(top) and from May 2011 with GPS(bottom). Different types of particles are named. (4500 Bins)

A comparison of the energy spectra in 'α range' for all four Si detectors is shown in figure 4.2 for data collected in 2011. The peaks are identified as α decays of ^{192}Bi, ^{196}Po and ^{196}At as indicated in figure 4.2. The four right-most peaks only appear in Si1,2, while the peaks on the left of the spectrum can be found in all four spectra.

This is because Si1,2 are situated at the implantation station of the WM (see section 3.3.1). After the wheel is turned to the decay station, ^{196}At will have decayed almost completely, having a half-life of 0.374(3) s. ^{192}Bi and ^{196}Po have longer half-lives (34.2(8) s and 5.64(6) s resp.) and are thus still visible at the decay station. A description of the half life determinations can be found in section 4.5.

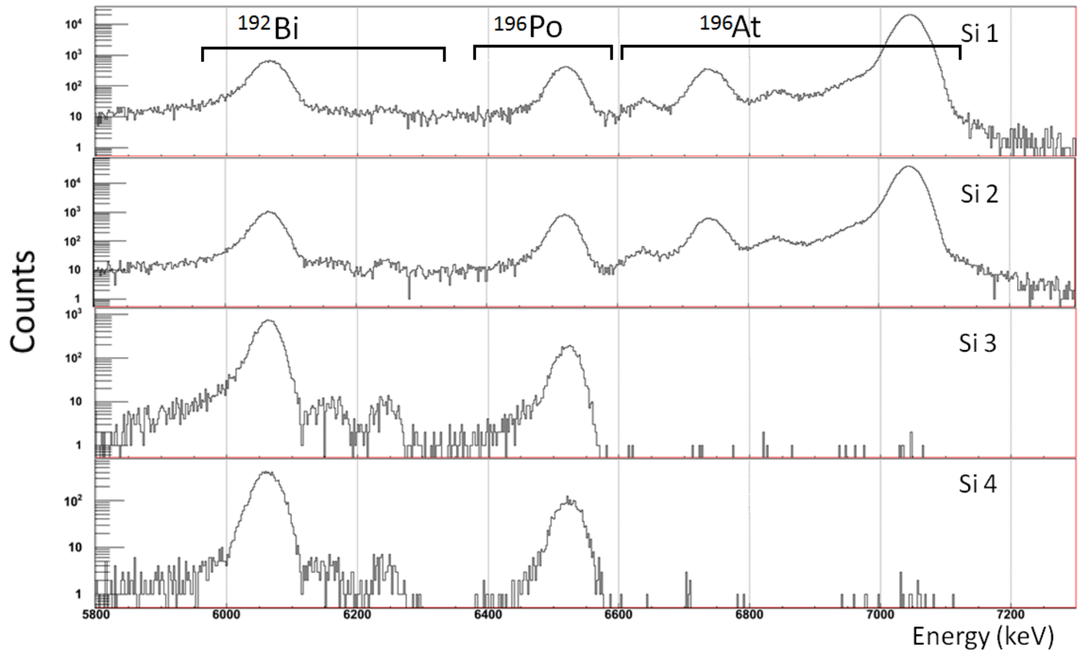

FIGURE 4.2: Energy spectrum in α range for Si1,Si2,Si3 and Si4 from top to bottom respectively. (4000 Bins)

During the May 2011 run, HPGe detectors were connected for ~30 minutes, during which $\sim 1.5\times10^6$ gamma rays were detected by both detectors. Since the data acquisition system also recorded the arrival time of all detector signals, it is possible to relate these γ rays to detected particles in for example Si detectors. Roughly 1.8×10^4 of these events were detected within a time interval of 2 μs before or after a particle event. Most of these coincidences are $e^- - \gamma$ events, since only ~1500 counts arise from the detection of an α particle and γ ray within this time window.
Based on the structure of the recorded time difference between α and coincident γ rays, shown in 4.3, the prompt timing gate for α-γ coincidences was chosen to be 0-600 ns. This choice reduces random coincidences. Figure 4.4 shows an α-γ plot, containing all prompt coincident events, defined by the latter the time window. This is shown in the bottom spectrum. The top spectrum shows the α decay energy spectrum.

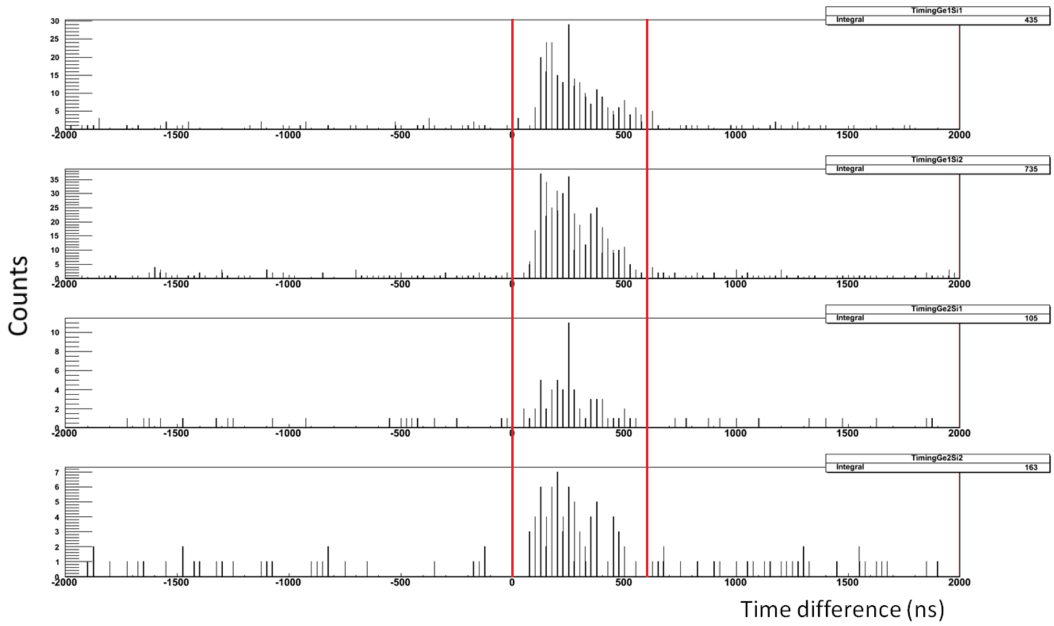

FIGURE 4.3: Time difference for α-γ coincident events for 4 different detector combinations (Si1Ge1 - Si2Ge1 - Si1Ge2 - Si2Ge2 from top to bottom). Energy ranges are: $E_\gamma \in$ [0,500] keV, $E_\alpha \in$ [5000,7300] keV. Two red lines indicate the chosen [0,600] ns coincident time window.

The combined information allows to construct a level scheme of ^{192}Bi, as discussed in section 4.3.

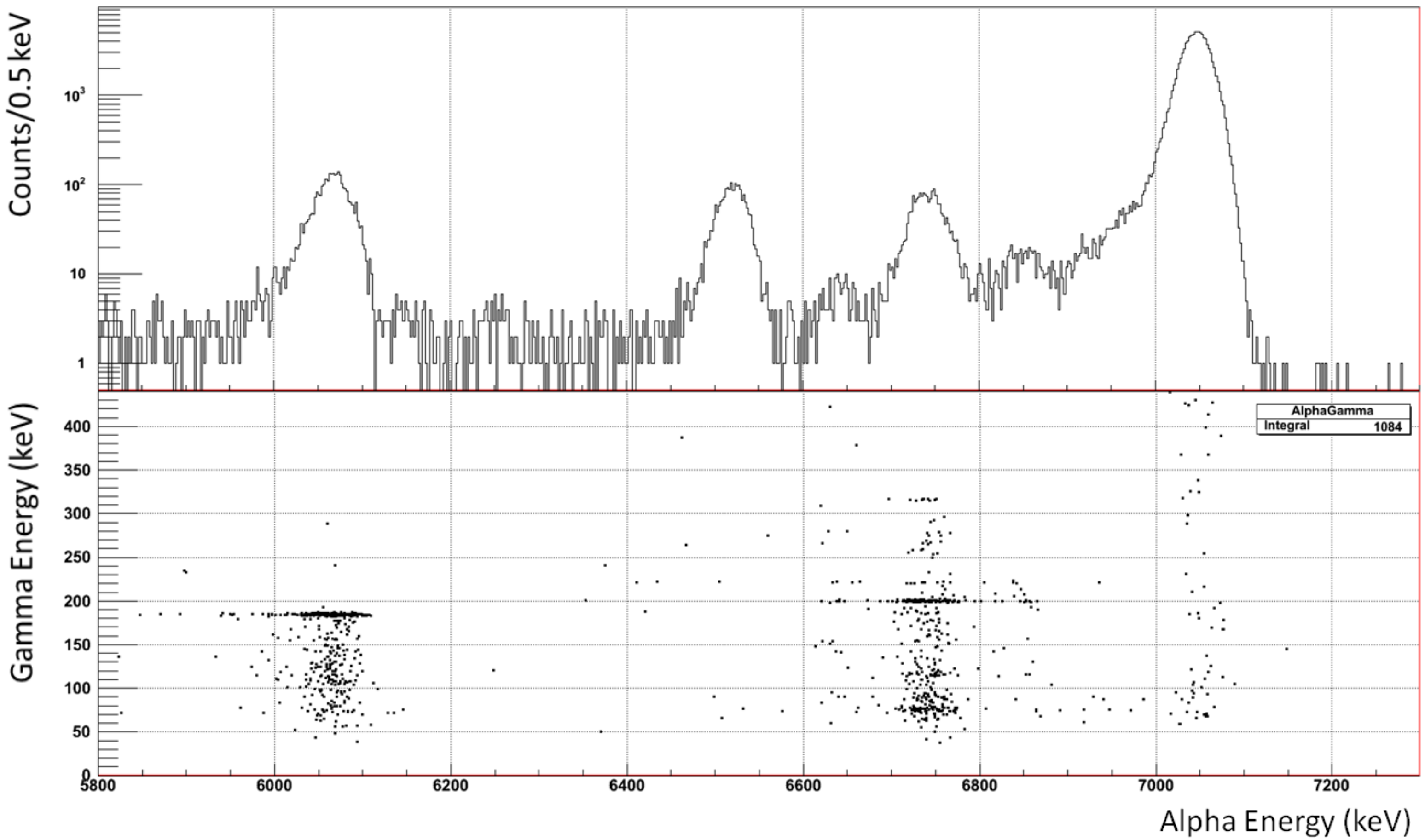

FIGURE 4.4: Singles energy spectrum added for Si1 and Si2(top) and α-γ coincidences(bottom). The presented data was taken while HPGe detectors were connected. Each dot in the bottom plot represents a coincident event.

4.2 ^{196}At fine structure

Prior to this work, only α decay line from ^{196}At to the ground state of ^{192}Bi was observed. Here, at least three more fine structure peaks are found as shown in figure 4.5.

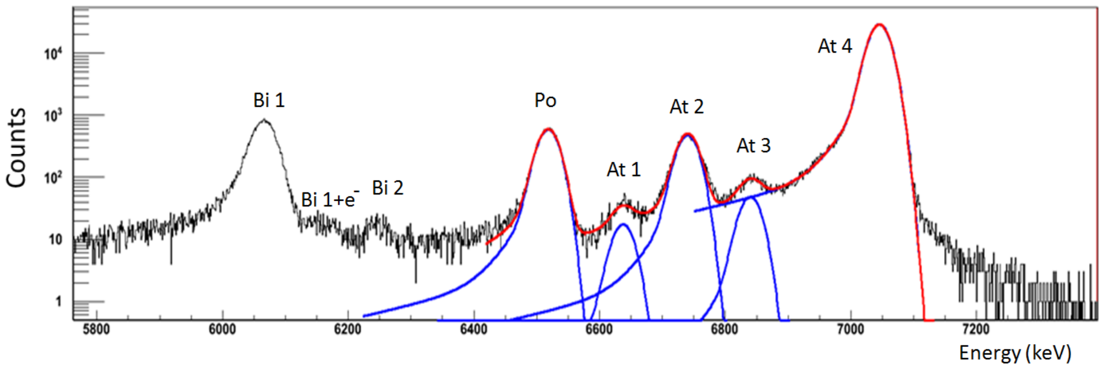

FIGURE 4.5: A fit of ^{196}Po and ^{196}At for the energy spectrum of Si1 and Si2 added together showing all data collected in May 2011. Fit function as described by Bortels et al. in [39]. (8000 Bins)

The assignment of At1,2,3 to the decay of At is based on results of α-γ coincidence analysis as well as on half-life measurements of the different peaks. As shown in section 4.3, the α particles related to At1,2,3 are in coincidence with γ rays of an energy equal to the Q-value difference between At1,2,3 and At4 respectively. Section 4.5 shows that the half-lives related to peaks of At1,2,3 are also within error bars equal to the half-life of At4 and the half-life of ^{196}At quoted in literature.

Figure 4.5 shows a fit of the α peaks coming from the decay of ^{196}Po and ^{196}At. The fit function that was used here was presented in [39] as an analytical function to describe peaks in α particle spectra from silicon detectors. The function consists of a convolution of a Gaussian and three exponential tails to the left. The resulting energies and integrals are shown in table 4.1.

The Q-value given in table 4.1 are equal to the total kinetic energy given to the α-decay products. Since also the recoiling nucleus carries a small amount of this energy (2%), the alpha energy lies slightly below the actual Q value of the decay. The kinetic energy of the alpha particle T_α can be approximated as $T_\alpha = Q(1 - 4/A)$ [1].

	E_α (keV)	Integral	Rel. intensity	$Q - Q_{At4}$ (keV)
Po*	6523(4)	2.42(2) $\times 10^4$	1.00	-
At 1	6642(4)	6.5(5) $\times 10^2$	53(4) $\times 10^{-5}$	415(5)
At 2	6744(4)	1.96(2) $\times 10^4$	16.0(2) $\times 10^{-3}$	312(5)
At 3	6846(4)	2.04(9) $\times 10^3$	16.8(7) $\times 10^{-4}$	208(5)
At 4*	7049(4)	1.199(1) $\times 10^6$	0.982(1)	0

TABLE 4.1: Fitted energies and integrals for peaks shown in figure 4.5. Relative intensities denote the measured ratio of a given α peak to the total observed amount of α decays for an isotope. Q-value differences with respect to At4 are also quoted. * denotes peaks to which the spectrum was calibrated using energies from [2].

4.3 α-γ analysis and the ^{192}Bi level scheme

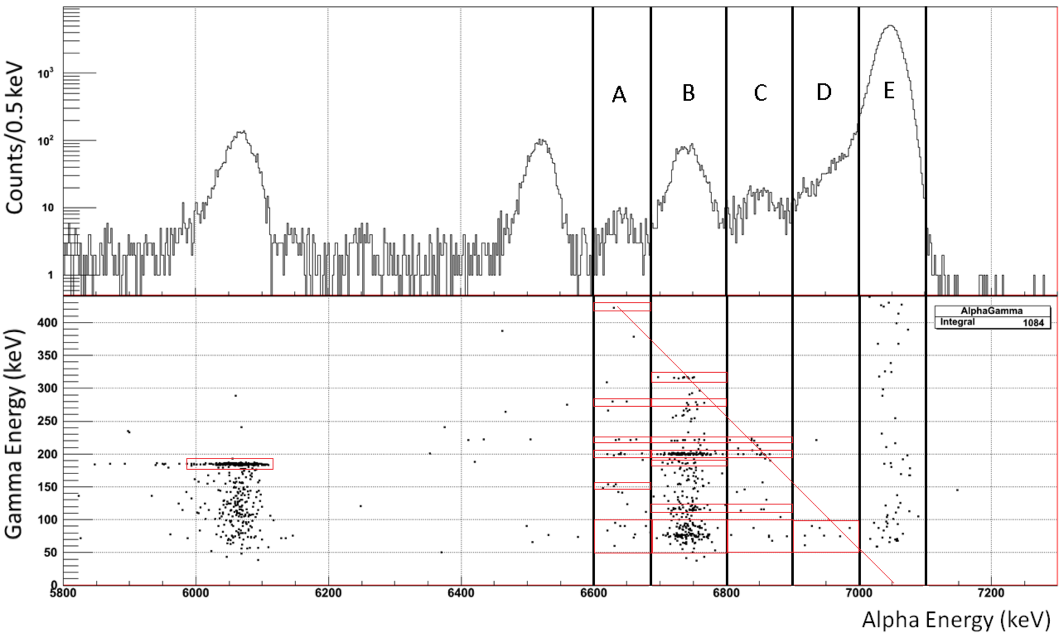

FIGURE 4.6: Energy spectrum added for Si1 and Si2(top) andα-γ coincidences(bottom) within a [0-600] ns time window. The presented data was taken while HPGe detectors were connected. Interesting regions (line struct., X-rays,..) are indicated with a red square.

In the α spectrum shown in figure 4.5, only four At peaks are clearly distinguishable. α-γ coincidence data (figure 4.4) suggests an underlying structure in the tail of the main ^{196}At peak, At4. Therefore, five different regions (named A-E) are chosen and shown in figure 4.6.

On the coincidence plot (bottom of figure 4.6), the coincident γ rays show line structures,which are related to previously unknown energy levels and transitions in ^{192}Bi, populated via the α decay of ^{196}At. Using the information provided by coincidence data, a preliminary level scheme of ^{192}Bi could be constructed and the α fine structure of ^{196}At can be studied more deeply.

4.3.1 Projections and possible relations

In order to search for low-lying levels and transitions in ^{192}Bi, spectra showing the coincident γ-ray energies are created for the different α-energy regions A to E. These plots, the so-called 'gamma projections' are shown in figure 4.8 and 4.9. The energies of the γ lines, obtained using a Gaussian fit, are also shown on the plots. Some γ-ray lines only contain a few counts, so their energy can only be estimated. The observed γ-ray energies for the different regions are quoted in table 4.2. Since At4 corresponds to a direct ground state transition, region E solely consists of random events. This can also be seen from figure 4.7, where the time difference between the detection of an α particle within a 7000-7100 keV energy range and a coincident γ ray is plotted. The randomness can clearly be seen from a comparison with figure 4.3.

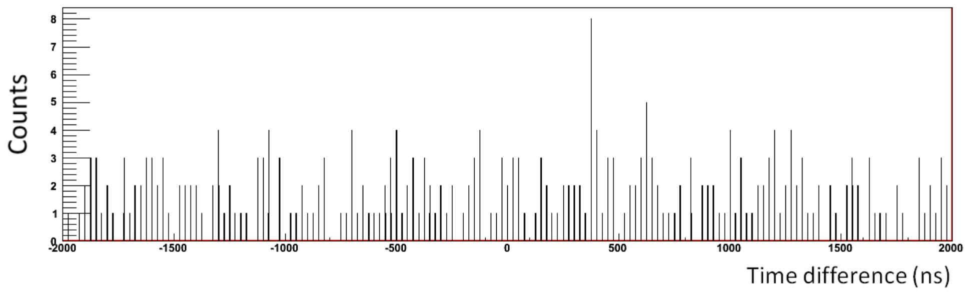

FIGURE 4.7: Time difference for α-γ coincident events. Energy ranges are: $E_\gamma \in [0{,}500]$ keV, $E_\alpha \in [7000{,}7100]$ keV.

As can be seen from figure 4.9, no random events are observed below an energy of $\sim$ 60 keV. It would be statistically impossible that 8 random coincident events with a γ-ray energy below 60 keV would be observed in region B, while none are observed in region E. This indicates that the low-energy counts present in region B might be expected to be 'real' transitions or result from Compton-scattered events thereof, but are not random. These observed energies can then be compared to the Q-value difference shown in table 4.1. This Q-value difference may be equal to the obtained

γ-ray energy, thereby indicating α feeding from ^{196}At to an excited level in ^{192}Bi, which then decays directly to the ground state. The energy of this nuclear level is then equal to the observed γ-ray energy. All ground-state transitions should lie in the vicinity of the sloped red line on figure 4.6, which indicates all points for which $Q_a = E_\gamma$.

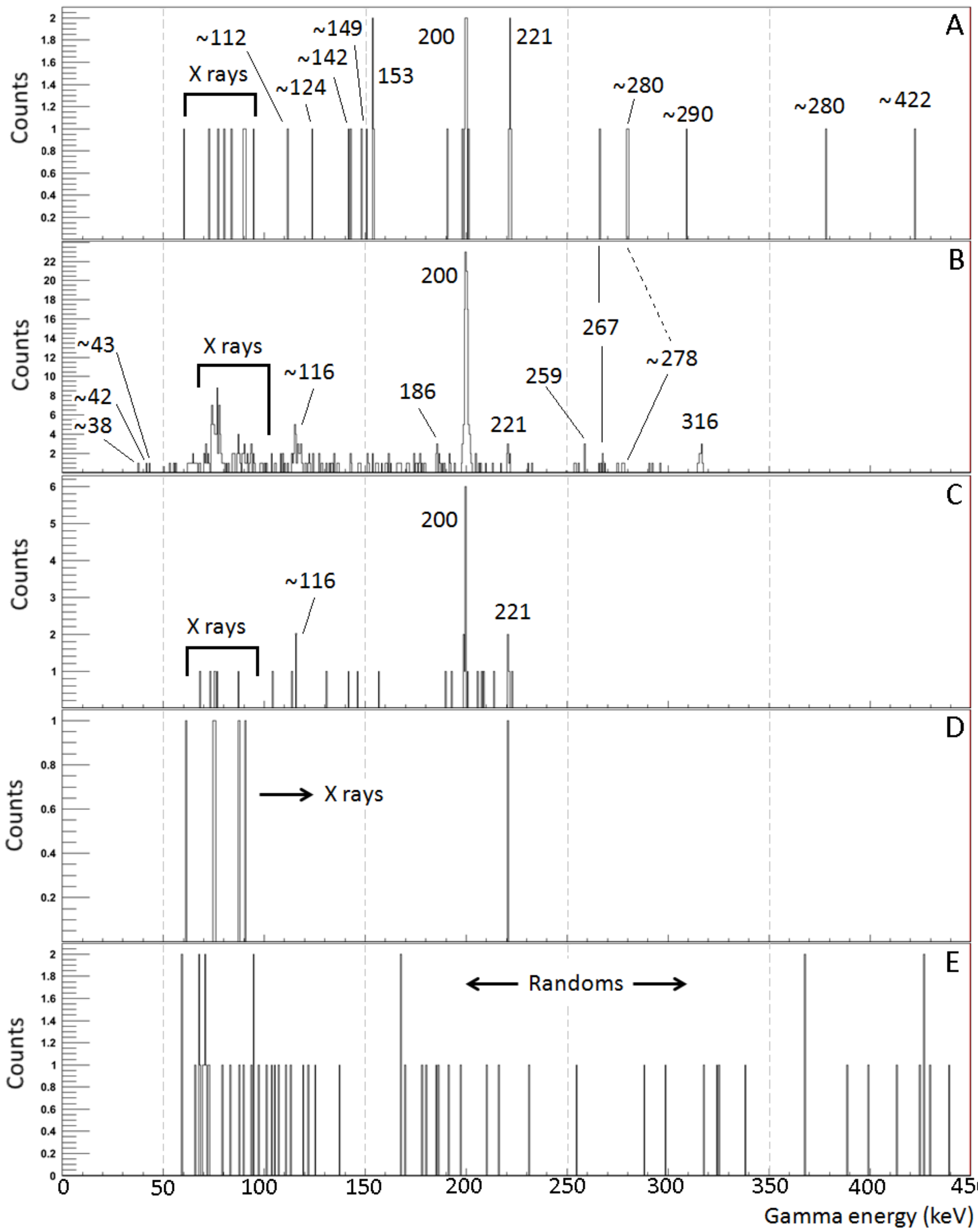

FIGURE 4.8: Projections of the coincident γ rays for α energy regions A-E shown in figure 4.6. $\sim$ denotes energies that were based on very few counts and for which a precise value could not be determined.

	E_γ (keV)
A	[422] - [378] - [309] - [280] - [266] - [293] 221(1) - 200.0(2) - 153(2) - 142(2) [124] - [112] - [95] - K_α(Bi) - K_β(Bi) - 60
B	316.2(4) - [293] - [278] - 267(1) - 259(3) - 221(1) 200.0(2) - 187(2) - 117(2) - 116(1) - 94(1) - K_α(Bi) - K_β(Bi) [85] - [78] - [71] - [56] - [53] - [50] - [43] - [42] - [38]
C	221(1) - 200.0(2) - 116(1) - [157] - [146] - [142] [131] - [105] - K_α(Bi) - K_β(Bi) - 68
D	K_α(Bi) - K_β(Bi) - [61]
E	Random coincidences

TABLE 4.2: Observed γ-ray energies and X-rays for regions A-E on figure 4.6. Square brackets [ ] denote *possible* transitions for which only one or two counts were observed and the energy could not be determined precisely. Such events might also be explained as being Compton events or background.

For region B, the 312(5) keV Q-value difference of At2 in table 4.1 equals, within error bars, the observed 316(1) keV γ ray energy.
For region C, two gamma ray energies at 200,0(2) and 221(1) keV are found close to the Q value of At3 at 208(5) keV. This issue will be discussed more deeply in section 4.3.2, where it is investigated whether or not two unresolvable, close-lying, levels at 200,0(2) keV and 221(1) keV are fed. The peak in region C might also be (partly) explained as being the result of α-e^- summing. Section 4.3.3 will dwell on this.
For region A, one single coincident count at 422 keV is observed. This might be an indication for a transition to the ground state, but more statistics should provide a conclusive answer. For region D, no clear α peak is distinguishable, and only an order of magnitude estimation for the Q value can be read of the spectrum. Figure 4.9 shows coincidences in this region with energies similar to K_α and K_β of ^{192}Bi as obtained from [40]. This may point to a strongly converted transition to the ground state, for which the exact energy cannot be obtained directly. The resulting level scheme of ^{192}Bi resulting from what was discussed until now is shown in figure 4.10

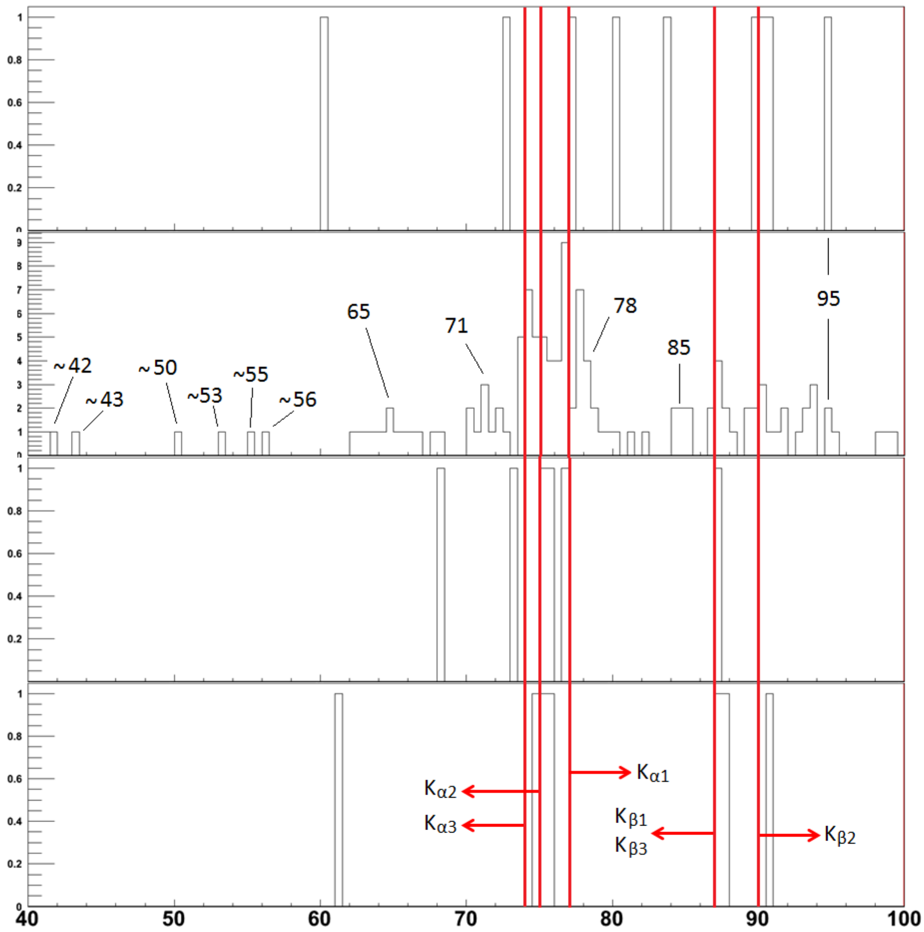

FIGURE 4.9: Zoom of gamma projections for 40-100 keV (X-ray region) for α energy regions A-D shown in figure 4.6.
$\sim$ denotes energies based on very few counts.
Red lines indicate Bi K X-ray energies from [40].

Apart from the comparison of the Q-value differences with the highest observed γ ray line for a given region of E_α, the gamma lines can be compared to each other in order to identify γ-ray cascades.

In order to further construct the level scheme of ^{192}Bi, internal relations between the observed γ-ray energies are sought for. A relation whereby two gamma rays add up to the energy of another gamma ray or a difference between two identified levels, indicates the existence of a gamma- ray cascade. Such relations are tabulated in 4.3. From this table, it can be seen that the single coincident count with energy $\sim$422 keV may come from a level at 420 keV, since several combinations seem to add up to this energy.
For some of these relations, it is not yet possible to place them in the level scheme, as is for instance the case for the 112 keV + 308 keV, since it is not sure if these

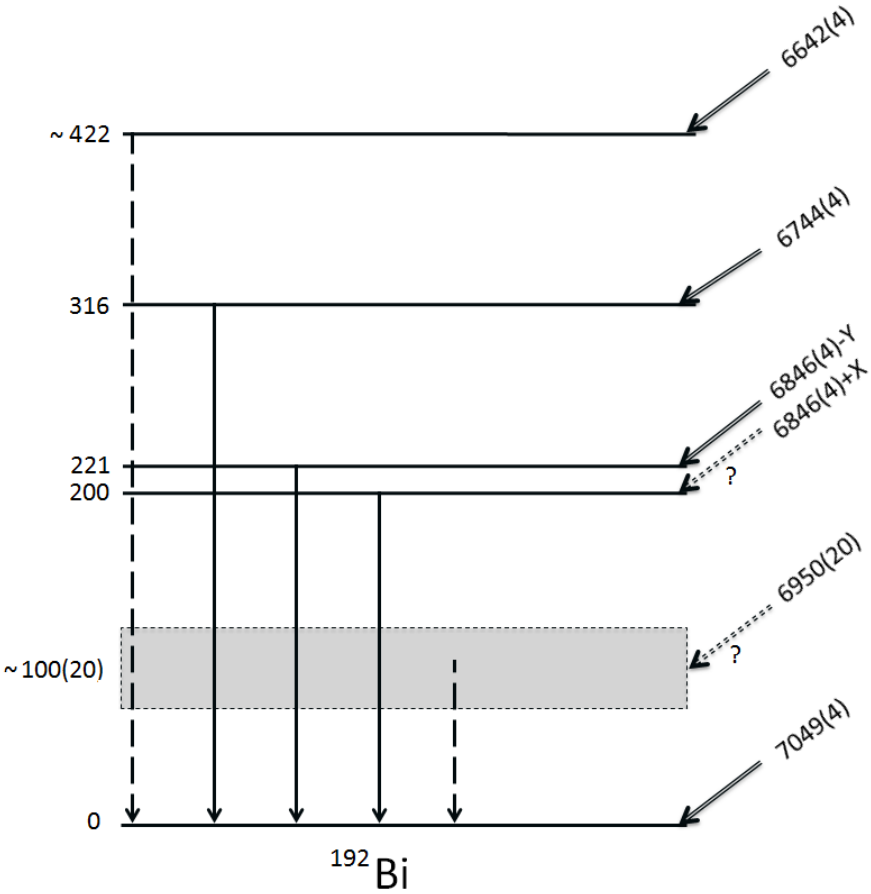

FIGURE 4.10: Building up the ^{192}Bi level scheme. Levels that are (possibly) fed by the α decay of ^{196}At
.

transitions connect 0-112-420 keV or 0-308-420 keV levels. Although a level at 112 keV could explain the X-ray counts observed in region D, no clear evidence for a 112 keV transition is found in regions B and C. Furthermore, no coincident event with 308 keV was observed in region B, making it highly improbable that this cascade is part of the level scheme.

Another way to check for possible cascades, is by investigating γ-γ coincidences. A plot showing all such coincidences in the region from 0 up to 430 keV for Ge1 and Ge2 is shown in figure 4.11.
A plot of the projection of an energy gate of $E_{\gamma1}$ around 200 keV is shown in figure 4.12. Here, the single-γ spectrum from Ge1 was scaled for visual comparison and is shown in red. A deviation from this single-γ behavior might then indicate a possible cascade. Different peaks originating from random coincidences follow the single-γ

$E_{\gamma 1} + E_{\gamma 2}$ (keV)	$= E_{\gamma 3}$ (keV)
116 + 200	= 316
95 + 221	= 316
56 + 259	= 316
38 + 278	= 316
or 38 + 221	= 259
78 + 200	= 278
153 + 267	= 420 (∼422)
∼142 + ∼278	= 420 (∼422)
296 + 124	= 420 (∼422)
308 + 112	= 420 (∼422)
149 + ((271))	= 420 (∼422)
71 + 200	= ((271))
∼50 + 221	= ((271))
85 + 186	= ((271))

TABLE 4.3: Relations between some observed γ energies which might indicate possible cascades. Double brackets (( )) indicate a not-observed transition.

spectrum. From figure 4.12, a 115.3(8) keV gamma line seems apparent, confirming the gamma ray cascade 316 - 200 - 0 keV, as indicated in table 4.3.

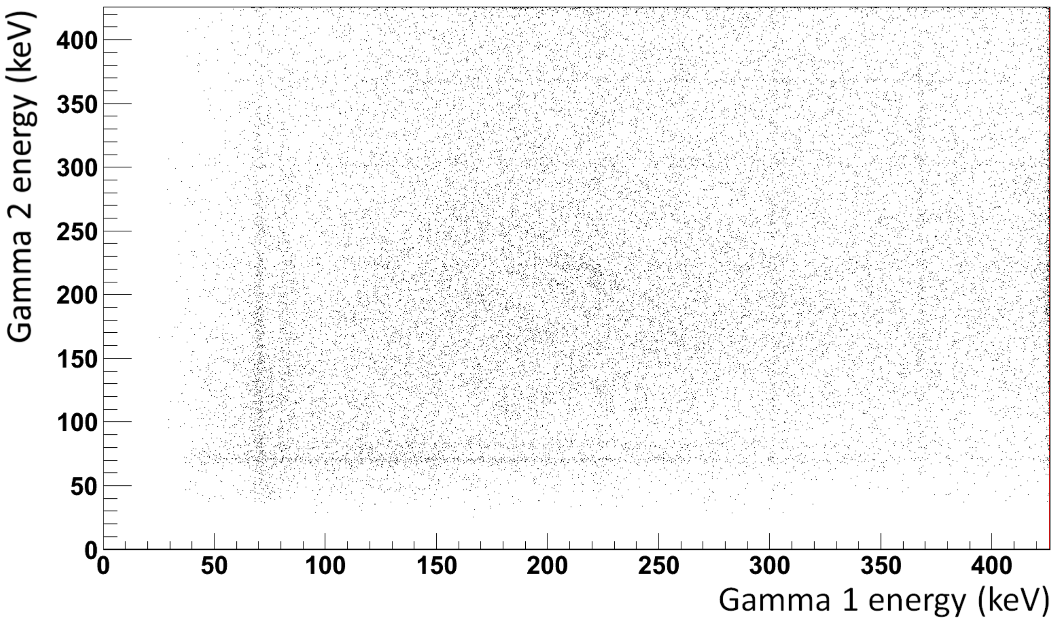

FIGURE 4.11: A plot of all γ-γ coincidences within a 600 ns time interval for an energy region from 0 up to 430 keV for Ge1 and Ge2.

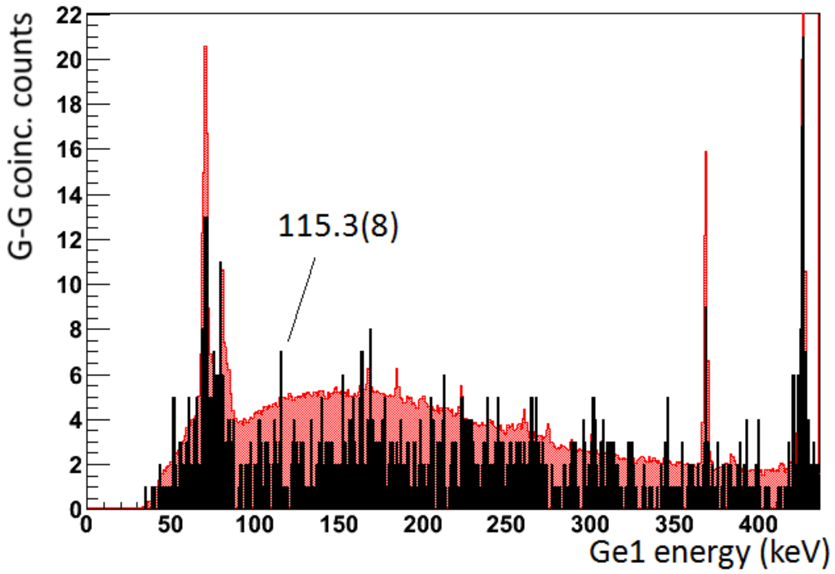

FIGURE 4.12: A projection of all γ-γ coincidences within a 600 ns time interval for an energy gate on the 200 keV γ line. The red plot shows the single-γ spectrum and is scaled for visual comparison.

4.3.2 Running gates

In order to further investigate the discrepancy between the Q-value difference and the observed γ energy of 200 and 221 keV found in region C, so-called 'running gates' were used. Here, the number γ rays for 30 keV wide α energy ranges are plotted. These window gates are shifted with 5 keV steps throughout a certain α-energy range. Each dot represents the number of α-γ coincidences present in the window in which the dot is centered. The square root of the number of counts was taken as error. Figure 4.13 shows an example of such a running-gate spectrum gated on the observed 200 keV and 221 keV γ line for α regions B,C and D.

Several interesting features are obtained from this plot. It can be seen for instance, that both γ lines cannot be explained as being coincident with α particles in the 'tail' of At2 in region B. This is due to the large dip in count number around 6800 keV in between the two maximums in regions B and C.

Another feature, is the difference in the position of the maximum in region C for both γ lines, which is spaced by $\sim$15 keV. This seems to support the possibility that the α peak in region C is a doublet.

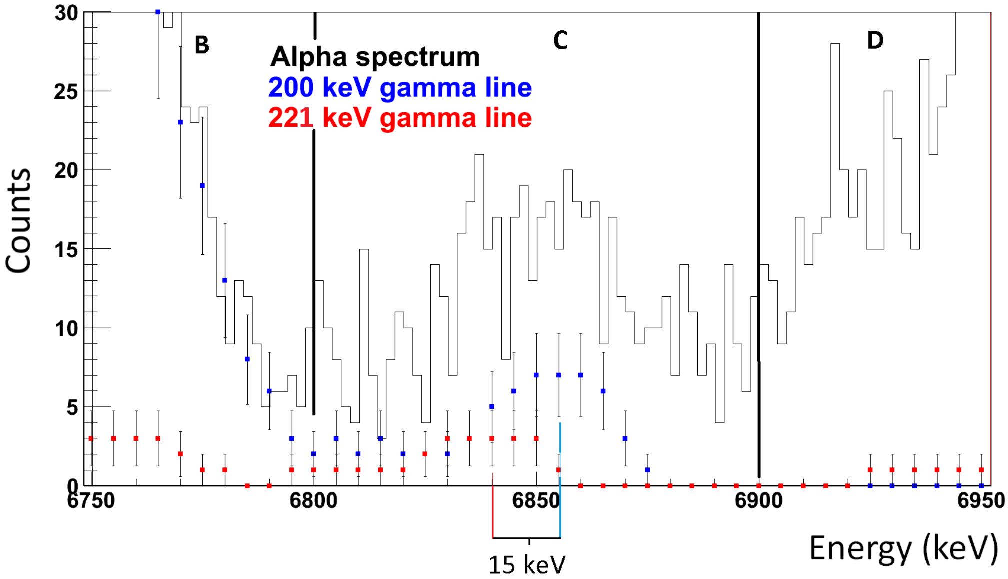

FIGURE 4.13: Running gates on 200 keV and 221 keV γ's in α regions B,C and D. Each dot represents the number of α-γ coincidences for the represented γ energy and a 30 keV α energy in which the dot is centered.

4.3.3 Possible α+e$^-$ summing in region C and D

Sometimes, a peak in the α spectrum is not simply explained as feeding to a different level in the daughter nucleus, but rather as a peak arising from an 'artificial' sum effect of α particles that have a lower energy with conversion electrons. The energy of the electron equals the transition energy from which the binding energy of the atomic electron is subtracted. Binding energies for atomic electrons of Bi are 90.5 keV and 16.4 keV for K and L_1 shells respectively. It should be carefully checked whether or not some of the five different observed regions in the ^{196}At α decay (regions A-E) arise from such an effect.

This can be checked by comparing the supposed energy of an α+e$^-$ sum event for different transitions to the observed peak energies. An estimate of the expected amount of counts and coincident X-rays in such a sum peak can then be compared to the observed amount of counts assuming different multipolarities for the converted transitions (E1,2,3,4 and M1,2,3 were checked). The estimation includes the observed amount of coincident γ rays for a given transition, supposed conversion coefficients (from [41]) and detector efficiencies for both Si and Ge detectors. The formula used for this estimation, was

$$N(sum) = N(e_{K/L}).P(sum) = N(\gamma).\alpha_{K/L}.P(sum). \tag{4.1}$$

Here, $N(sum)$ represents the number of expected counts in a α+e$^-$ sum peak. $N(e_{K/L})$ is the expected number of conversion electrons that is emitted for a certain transition, when a number of $N(\gamma)$ γ rays are in coincidence with the α line from which the summing originates. $P(sum)$ in equation (4.1) represents the geometrical probability for detecting two particles in a single Si detector and $\alpha_{K/L}$ represents the K or L conversion coefficient obtained from [41] for different transition energies and multipolarities. Assuming a detection efficiency of 19(2)% and 30(2)% for Si1 and Si2 respectively, the probability for detecting two particles in one detector,$P(sum)$, was calculated as Eff$(Si)_1$.Eff$(Si)_1$ + Eff$(Si)_2$.Eff$(Si)_2$ = 0.13(2). The detection efficiency for electrons in Si detectors was taken as 100%, which is most probably not the case. In order to obtain an order-of-magnitude estimate, the spatial coincidence probability was taken into account. The result of this calculation should thus be interpreted as an upper limit.

$N(\gamma)$ was efficiency corrected, using Ge and Si detection efficiencies, as shown in equation (4.2). α-γ coincidences are detected in one of four detector combinations possible using Ge1,2 and Si1,2. When calculating $N(\gamma)$ for a certain transition, the coincident counts detected in every detector combination, are corrected for the total efficiency = Eff$(\gamma)_i\times$ Eff$(Si)_j$ for $i, j = 1$ or 2. Hereby, four 'estimates' of the total amount of coincidences are obtained. $N(\gamma)$ was than taken as the weighted average of these numbers using

$$N(\gamma) = \frac{\sum_{i,j=1}^{2}(N(\gamma)_{ij}w_{ij})}{\sum_{i,j=1}^{2}w_{ij}} \tag{4.2}$$

$$\text{,where} \quad N(\gamma)_{ij} = \frac{N_{Obs}(\gamma)_{ij}}{\text{Eff}(Ge)_i.\text{Eff}(Si)_j} \text{ and } w_{ij} = \frac{1}{\sigma_{ij}^2}.$$

$N(\gamma)_{ij}$ in these equations are the efficiency-corrected counts for detector combination GeiSij. σ_{ij} represents the error on $N(\gamma)_{ij}$. The error on the weighted mean,$N(\gamma)$, was calculated via $\sigma^2_{N(\gamma)} = 1/\sum_{i,j=1}^{2}w_{ij}$.

The peaks in regions A,B and E cannot be fully explained by summing effects of peaks from different regions. The peak in region E is clearly due to the α decay of ^{196}At to the ground state of ^{192}Bi. The peak in region A cannot be due to α+e^{-} summing, since their is clearly no α peak lower in energy from which the summing would arise. Considering the fact that the solid angle of each detector is less than 50% of 4π, the α-e^{-} sum peak can never be larger then the original peak. Therefore, At2 in region B cannot be a sum peak. Arguments to exclude summing could not be stated for α regions C and D, so the possibility was checked. Figure 4.14 shows a close-up of the At range of the energy spectrum. Possible α + conversion e^{-} energies are shown on top of the energy spectrum as blue lines numbered 1-8. The α peak and (possibly) converted transition giving rise to lines 1-8 are quoted in table 4.4. Red lines indicate E_α as in table 4.1. Black lines mark the borders of regions A-E.

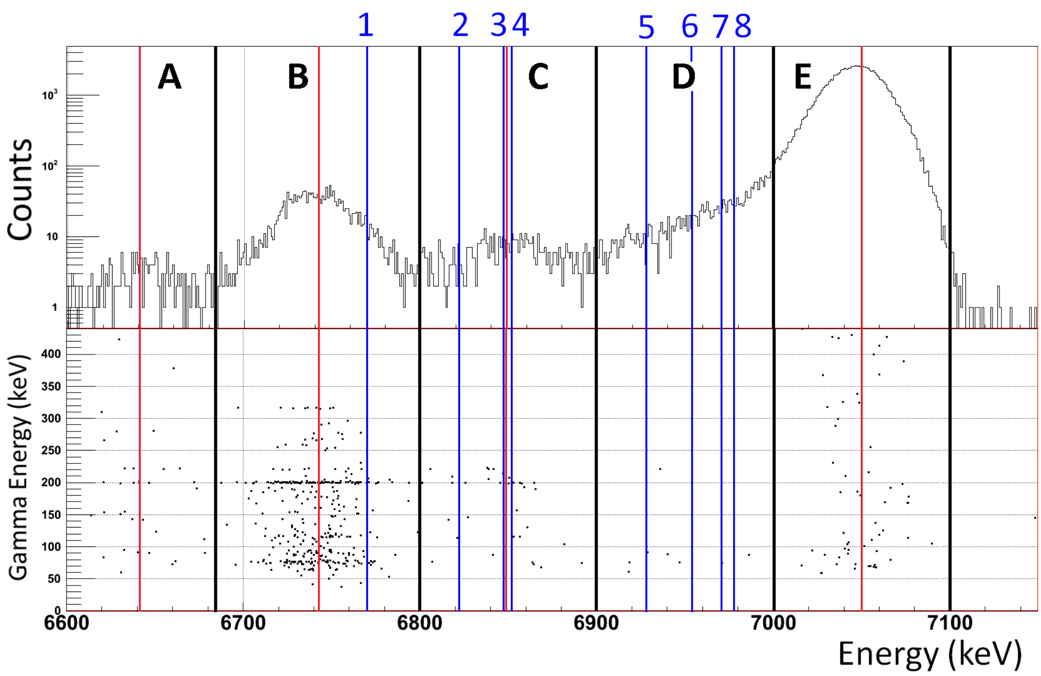

FIGURE 4.14: Possible α + conversion e^{-} energies are shown on top of the α and α-γ energy spectrum as blue lines numbered 1-6 (see also table 4.4). Red lines indicate E_α as in table 4.1. Black lines mark the borders of regions A-E.

From these energetic considerations, it is seen that the high energy shoulder of At2 might be due to summing with K-conversion electrons originating from the 116 keV transition. In addition, At3 might be partially explained by L-electron summing from this same 116 keV transition. Although summing with K-conversion electrons of 200 keV in region C is also plausible from energetic considerations, this summing effect

Line	sum energy (keV)	origin: E_α(keV) + conv. e^-
1	6770(4)	6744(3) + K(116(1))
2	6823(3)	6744(3) + L(95(1))
3	6846(4)	6744(3) + L(116(1))
4	6854(3)	6744(3) + K(200,0(2))
5	6928(3)	6744(3) + L(200,0(2))
6	6955(3)	6846(3) + K(200,0(2))
7	6970(3)	6744(3) + K(316.2(4))
8	6977(3)	6846(3) + K(221(1))

TABLE 4.4: Possible α + conversion e^- sum energies and origin for lines in figure 4.14

seems unlikely since 200 keV γ rays are observed in coincidence with At3. Furthermore, the 116 keV γ ray is smaller in amplitude as compared to the 200 key γ ray in the α-γ coincident spectrum of region C, as shown in projections in figure 4.8. This argument also supports the fact that the 116 keV transition is strongly converted. Finally, part of the α counts in region D might be explained by summing of L-electrons from the 200 keV transition and α's from the 6744 keV peak. Also K-electron summing with this α peak and the 316 keV transition can contribute to possible counts in region D. Summing of K-electrons from the 200 keV or 221 keV transitions and 6846 keV α's would also end up in region D of the α spectrum. It should be noted however, that the summing of an α with an L-electron would not contribute to the number of observed X-rays, since the energy threshold of the HPGe detectors is to high. In the scope of this thesis, only summing by At2 and L-conversion electrons of the 116 keV γ rays to explain possible summing in region C, is investigated. The result of this estimation can be found in table 4.5.

	116 keV	
	# e^-(L)	# exp. sum
E1	29(6)	4(1)
E2	$1.4(3)\times10^2$	180(40)
E3	$32(6)\times10^3$	$4(1)\times10^3$
E4	$45(1)\times10^4$	$6(1)\times10^3$
M1	$5.7(11)\times10^2$	72(18)
M2	$7.4(14)\times10^3$	$9(2)\times10^2$
M3	$10(2)\times10^4$	$13(3)\times10^3$
Obs.		$1.8(3)\times10^2$

TABLE 4.5: Estimated number of emitted conversion electrons and resulting number of expected sum-peak counts in region C.
The observed amount of counts in region C for the duration of the time when also γ detectors were present is shown in the bottom line.

From table 4.5, it can be seen that the 116 keV transition will most probably not be of an E3, E4 or M3 multipolarity, since the expected sum counts strongly exceed the total number of observed counts in region C. The lifetime for an E3 or E4 transition would also be too long for the γ ray to be observed in prompt coincidence with the α particle. Also, it is shown that α-e$^-$ summing is significant if the transition would have multipolarities M1 or E2.

4.3.4 Populating only one isomer in ^{192}Bi

Two isomers of ^{192}Bi, having half-lives of 40.6 s and 34.6 s, with respective 10^- and 3^+ spin and parities are known. Their consecutive α and γ decay have been studied ([42]), and results are shown in figure 4.15.

When studying βDF, it is important to know whether or not several isomers are produced, since they can in principle exhibit different fission behavior. In this section, it is shown that predominantly, only one isomer of ^{192}Bi is populated after the α decay of ^{196}At, indicating that only one isomer of ^{196}At was produced. This is supported by half-life determinations as discussed in 4.5.

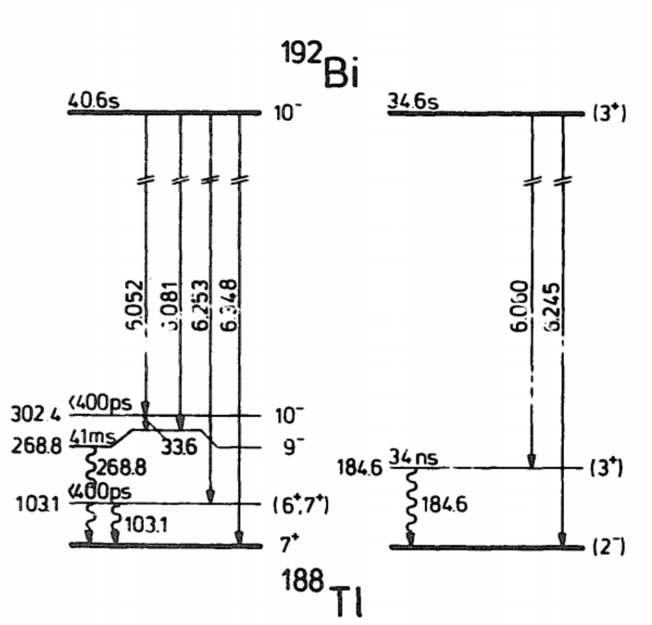

FIGURE 4.15: The α decay of ^{192}Bi showing two different isomers. figure from [42]

In the data presented in figure 4.2 and named in figure 4.5, three peaks are present which are related to the decay of ^{192}Bi. The largest peak, with E_α equal to 6060(5) keV has a strong coincident γ line at 184 keV. The second peak at 6151(4) keV is due to the summing of K-conversion electrons of the 184 keV transition and 6060 keV α particles. The energy of the third peak is found at an energy of 6242(2) keV. These observations unmistakably point to a population of the 3^+ isomer in ^{192}Bi.

From the fine structure of the 10^- isomer shown in figure 4.15, three out of four α peaks would possibly be unresolvable from the two fine structure peaks of the 3^+ isomer. Only the 6348 keV α has a reasonable energy separation from the rest. This peak is not clearly seen from the spectra, but this does not necessarily implicate it's complete absence. What can be done, is putting an upper limit on the area of the sought-for peak. A procedure explained in [43] was followed in order to determine such an upper limit. The upper limit A on the number of counts in the expected peak is calculated via

$$\alpha = I\left(\frac{A-\bar{a}}{\sigma}\right) \Big/ I\left(\frac{-\bar{a}}{\sigma}\right) \qquad \text{,where } I(z) = \frac{1}{\sqrt{2\pi}}\int_z^\infty e^{-x^2/2}dx. \tag{4.3}$$

Here, α represents the statistical significance level, σ^2 equals sum of the variance of background counts with the number of counts C in the region where the peak is expected. $\bar{a}$ represents the background-subtracted counts in the expected peak region. Spectra from Si3 and Si4 were chosen and added, since they have a much lower background level than the spectra from Si1 and Si2. This significantly lowers the upper limit A. The peak at 6348 keV was proposed to be found within the interval of 6330 keV to 6370 keV. The 95% significance level upper limit was calculated to be 9.5 counts for the proposed peak. Using the 2.5(2)% relative branching with respect to the 6052 keV intensity, this states that, at this significance level, at most 3.8(3)$\times 10^2$ counts in the 6060 keV Bi peak are due to the 10^- isomer. If the total integral is calculated for this peak from a fit, and added to the integral of the α+e$^-$ sum peak, a total of 239(3) $\times 10^2$ counts of 6060 keV alpha particles was recorded. An upper limit on the population of the 10^- isomer, is then put at 1.6(1)% with a 95% significance level.

This upper-limit calculation, in combination with the non-observation of the 103 keV or 269 keV γ rays in the coincident α-γ spectra, and the determination of the half-lives in section 4.5 (fitted $t_{1/2}$= 33.2(14) s for ^{192}Bi), strongly indicate that only the 3^+

isomer in ^{192}Bi is fed. This thus implicates, because of the spin- and parity- selection rules in alpha decay, that only the 3+ ground state of ^{196}At is produced

4.3.5 ^{192}Bi level scheme

Using the information described in previous sections, a preliminary level scheme of ^{192}Bi can be constructed. Due to the low statistics, different transitions and energy levels are suggested by only several counts or in some cases even only one count. It is therefore, that on the presented level scheme, a few lines are shown as dashed lines. These indicate that a hint of these transitions or levels were observed, but more data should be gathered to confirm or dismiss these suggestions.

At least four different levels in ^{192}Bi are directly populated via the α decay of ^{196}At. These levels are the ground state, 221 keV, 316 keV, and 420 keV.
There is a possibility that states $\sim$100 keV and 200 keV are also populated directly, but this cannot be stated with certainty. The fact that the transition with energy 200keV is the strongest in regions A.B and C, suggest that this decay feeds the ground state. Using this as a basis, the rest of the level scheme can be constructed using the relations from section 4.3.1. It is built only upon the 3^{+} isomer of ^{192}Bi, which was argued in section 4.3.4. The resulting level scheme and transitions can be found in figure 4.16.
As indicated in previous sections, several questions remain yet unanswered, and a more extended study including Monte Carlo simulations to estimate the α-e^{-} summing is necessary.

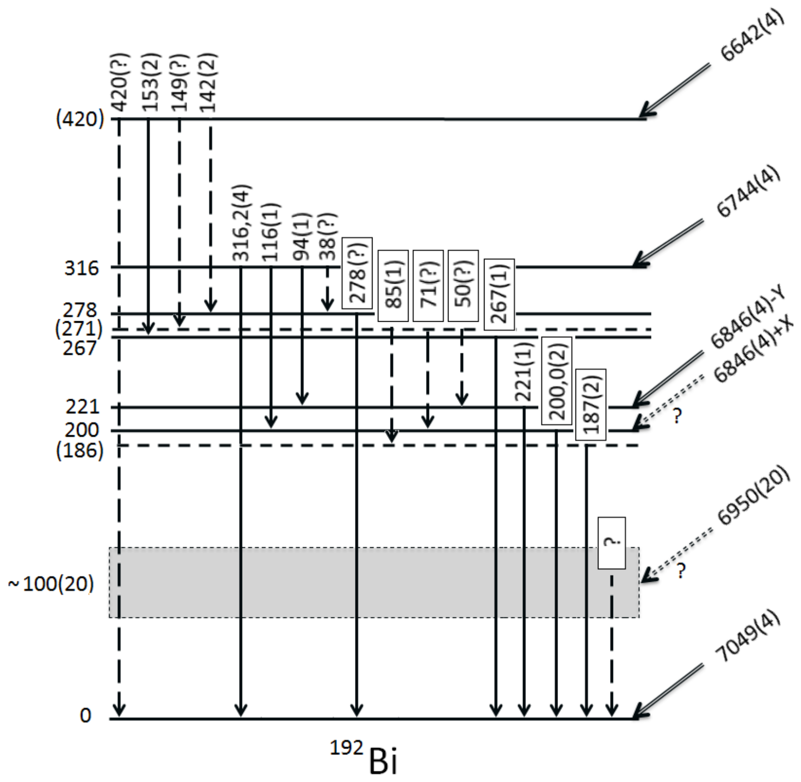

FIGURE 4.16: Preliminary level scheme for ^{192}Bi.

4.3.6 Reduced α widths, δ_{α}^{2}

The reduced α emission width, δ of an α transition, in this text often shortened to 'reduced width', is calculated via

$$\lambda = \delta^2 P/h. \tag{4.4}$$

Here, λ represents the decay constant, P is the penetration factor and h stands for Plancks constant. The reduced width, allows to compare different α emissions processes, since it corrects for the energy dependence of Coulomb-barrier tunneling. A larger value corresponds to a higher (corrected) transition rate.

In order to calculate the reduced α widths, the relative feeding of the different α transitions should be obtained. Important to notice is that the relative branchings and related the reduced α widths should not be deduced using only the α spectrum. It could in fact be that, due to the Si detector resolution, close-lying α lines are unresolvable. Consequently, wrong relative branchings and reduced α widths would be calculated.

A study of α-γ coincidence data could possibly resolve underlying structures. Relative branchings and reduced widths should then be calculated using the α-γ data corrected for detectors efficiency curves.
If one would naively use the fit result as shown in table 4.1 and the weighted half-lives from section 4.5, the reduced widths would be 0.4(1), 5.4(2), 26(1) keV for At1,2,4 respectively, when also the β branch is taken into account.
These values should be corrected for possible summing effects described above. The reduced α widths for these three peaks however will not change much.

The values shown here, thus give a reasonably good idea of how large the reduced widths are for different parts of the fine structure, even though the exact fine-structure feeding is not completely known. It is thus clearly seen that the reduced width of ground state to ground state alpha transition is much larger as compared to the fine structure decay. This is expected, since for example spin/parity changes might occur in fine structure decay, which hinder alpha decay.
The 26 keV reduced width for the 7049 keV α line is only weakly hindered and might correspond to an α transition connecting two states with the same spin and parity although a ΔL $= 1$ cannot be excluded.

4.4 Calculation of b_β for ^{196}At

In order to calculate the probability for β-delayed fission, $P_{\beta DF}$, an accurate value for the number of β decays of the parent nucleus has to be known. For the data taken in May 2012 with GPS, the number of ^{196}Po α decays following the β decay of ^{196}At is hard to determine. This is due to the fact that the peak is surrounded by several beam contaminant peaks and only shows up as a small bump situated on a large heap of counts of which many may come from inefficiently collected, more energetic α particles but also from summing of electrons with less energetic α particles. If the number of β decays would have to be calculated solely from the GPS data, a large error on $P_{\beta DF}$ would be introduced.
A different approach, used in chapter 5, uses the β branching b_β to calculate the number of β decays of ^{196}At. In this section, a precise value for the β-branch ratio b_β (and b_α) is calculated using data collected with HRS.

The beta branching b_β is defined as the ratio of the amount of β decays to total decays of a given nucleus. For ^{196}At, this calculation translates to

$$b_\beta(^{196}\text{At}) = N_\beta(^{196}\text{At})/(N_\beta(^{196}\text{At}) + N_\alpha(^{196}\text{At})) \tag{4.5}$$

, where $N_{\alpha,\beta}$ denotes the number of α, β decays respectively. A measure for $N_\beta(^{196}\text{At})$ is obtained from the number of α decays of ^{196}Po and it's β branch $b_\beta(^{196}\text{Po})$ via

$$N_\beta(^{196}\text{At}) = N(^{196}\text{Po}) = N_\alpha(^{196}\text{Po})/(1 - b_\beta(^{196}\text{Po})) \tag{4.6}$$

While N_α is obtained straightforwardly by summing the integrals of all fine structure peaks for ^{196}At solely from Si2, N_β has to be taken from Si2, Si3 since it still present when the foil is moved to the decay station, and the number of counts has to be corrected for several effects. These correction effects include possible direct production of ^{196}Po, solid-angle scaling effects and counts lost due to the decay of ^{196}Po during the transportation of the C-foils from the implantation to the decay station.
The amount of direct production of ^{196}Po is obtained from the comparison of dedicated measurements taken when RILIS lasers are either operational or blocked without moving the rotating wheel. Other corrections were done off-line and are obtained from the time structure of the ^{196}Po α detection events.

When all corrections are taken into account as described in the following sections 4.4.1 and 4.4.2, the β branching, b_β is found to be 2.4(1)%. The α branching b_α (=1-b_β), is then 97.6(1)%. A summary of the fitted counts and corrections can be found in table 4.6.

	^{196}Po counts	^{196}At counts
Si2 (impl.)	15.3(1)×10^3	778.4(12)×10^3
Si3 (decay)	3.68(6)×10^3	-
Direct prod.*	-0.17(4)×10^3	-
Si3 scaling*	-1.47(4)×10^3	-
WM movement*	+0.36(2)×10^3	-
b_α(^{196}Po)	×(1/0.94(5))	-
Total	18(1) ×10^3	778.4(12) ×10^3
	b_β = 2.4(1)%	

Table 4.6: Summary of integrals and corrections used to calculate b_β as explained in sections 4.4.1 and 4.4.2.
* Denotes corrections which are experiment specific.

4.4.1 Direct production

In order to deduce the amount of directly produced ^{196}Po, measurements were done without moving the rotating wheel. These measurements were only started after a waiting period of several minutes, allowing all of the previously implanted Po to decay ($T_{1/2}$(^{196}Po)= 5.64(6) s).
After this waiting period, the first run was taken without lasers for ∼800 s. During the second run, the lasers were unblocked and a measurement was taken for ∼1000 s. The result of these two runs are plotted on top of each other in figure 4.17. While ^{196}At has completely disappeared in the spectrum, ^{196}Po and ^{192}Bi are still present when the lasers were blocked, indicating a direct production of 1^{196}Po.
A clear indication that the counts in the ^{196}Po peak of the lasers-off spectrum are indeed the result of directly produced ^{196}Po, is shown in figure 4.18. Here, the time structure for counts which are energy gated on E_α of ^{192}Bi and ^{196}Po is plotted. A different behavior for Bi and Po is observed: While Bi only decays at the beginning of the run, Po is present at a near-constant rate throughout the whole measurement. This indicates that ^{192}Bi ($T_{1/2}$ = 34.28 s) originates from previous runs, while ^{196}Po was directly produced.

The resulting values of these runs are shown in table 4.7. For the values of the lasers-off run, the square root was taken as error, since a correct fit was impossible due to the low count number. The laser-on spectrum peaks were fitted to obtain the peak content. When the values are added for Si1,2 and scaled to the time of the lasers-on

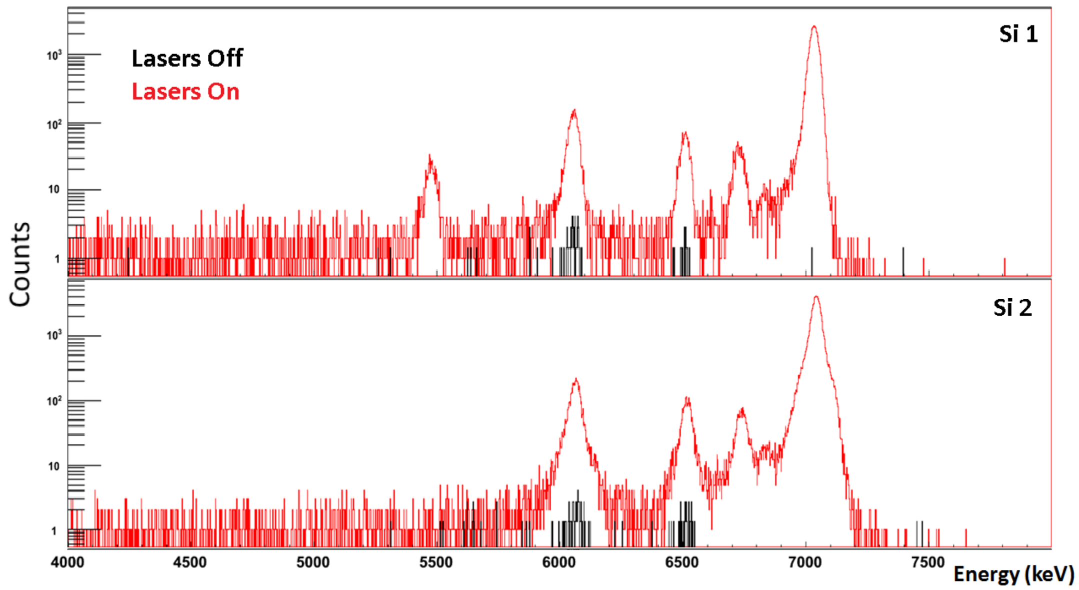

FIGURE 4.17: Energy spectra for Si1(top) and Si2(bottom) for dedicated measurements with lasers on(Red) and off(black). Spectra were scaled to measurement time.

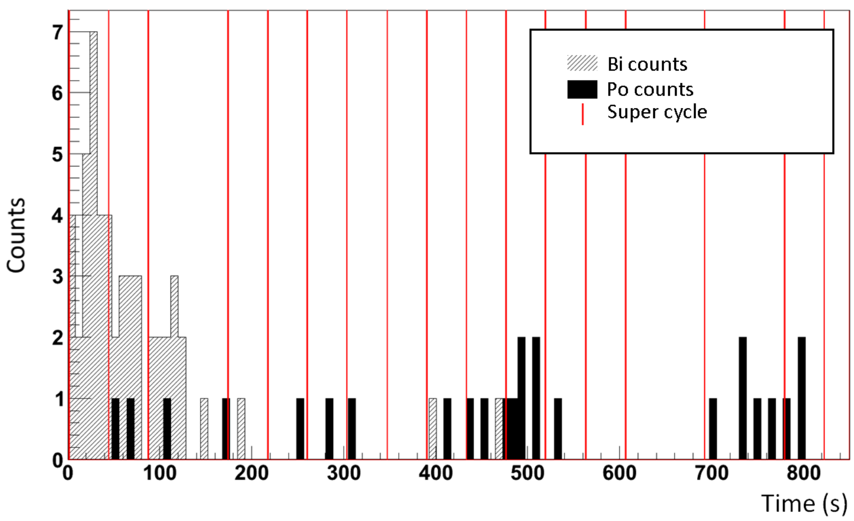

FIGURE 4.18: Po (black filled) and Bi (black striped) incidence times during lasers-off measurement in Si2. Super cycles are shown in red and contained 11 proton pulses each.

measurement, the ratio of collected counts with lasers off/on was calculated to be 1.5(2)%. The total observed α rate for directly produced ^{196}Po was 0.052(8) observed α's/s. The α detection rate for direct production for Si1 and Si2 were 0,020(5) α's/s and 0,033(7) α's/s respectively.

	^{196}Po counts (Si1)	^{196}Po counts (Si2)	meas. time (s)
Lasers Off	15(4)	25(5)	766.5(1)
Lasers On	1418(61)	2333(90)	1049.0(1)
Dir. prod. rate	0,020(5) α's/s	0,033(7) α's/s	
	Direct production = 1.5(2)%		

TABLE 4.7: ^{196}Po counts and measurement time for lasers Off/On measurements.

4.4.2 Additional corrections

Not all ^{196}Po nuclei have decayed at the end of a measurement cycle, when the carbon foil is moved from the implantation station to the decay station, causing a loss of counts for the duration of ~1 s when the foil does not face a silicon detector.

To obtain a correct count number for the total ^{196}Po α decays, events from both the implantation and decay station have to be added as well as the events that are lost due to the WM movement.

Another possible form of count loss arises, when a measurement is abruptly ended at the end of a super cycle. Since the Si detectors are not recording any events after the measurement ends, the longer-lived ^{196}Po decays without being recorded. The α counts of ^{196}At however, will all be recorded, having only a half-life of ~0.3 s.

Such abrupt endings would thus artificially increase ratio of recorded At to Po counts. A schematic representation of the super cycles which should be included to account for this effect is shown in figure 4.19. The amount of ^{196}At and ^{196}Po α decays is only compared for cycles, like the ones shown.

It is also assumed that, at the start of a measurement cycle, the C-foil which is situated at the decay station is 'clean'. Therefore, the counts collected at the decay station during the first super cycle of a measurement, are not included in this calculation.

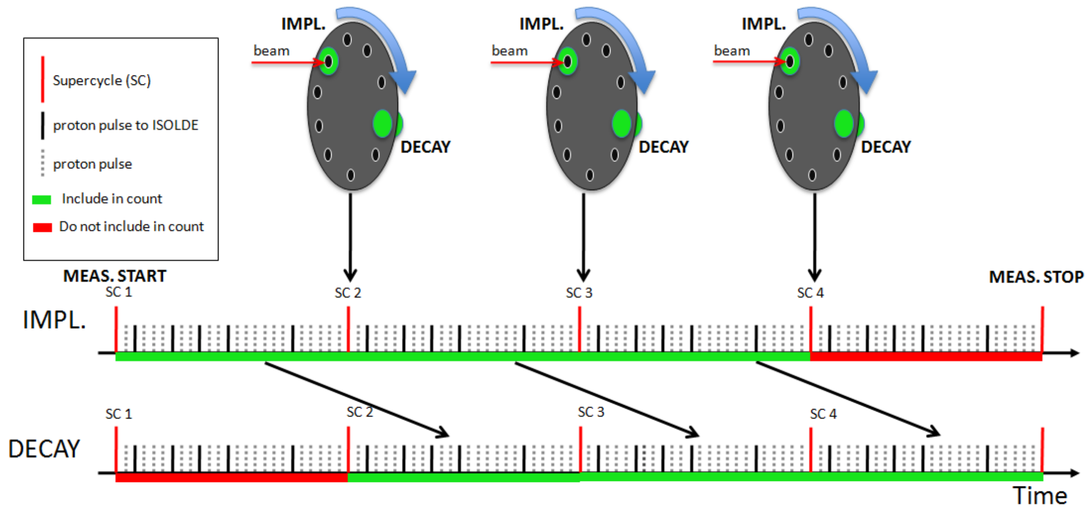

FIGURE 4.19: Schematic overview of principle for which counts to include when estimating the WM movement correction. Only the super cycles indicated in green, are included in counting.

In order to obtain the correction factor for this issue, along with the solid angle difference between both detectors, the time spectra for Si2 and Si3 were placed after each other as shown in figure 4.20. The spectrum for the decay station detector was then fitted with an exponential curve and extrapolated to the left, which is shown by the blue line on figure 4.20. The red line indicates a fit of Si2, which was then extrapolated to the right. Although the half lives resulting from these fits are the same within error bars, the amplitudes clearly differ. The ratio of these amplitudes give the solid-angle difference between both detectors. The counts in Si3 are scaled to the red fit as shown in the bottom plot in order to relate similar conditions for Si2 and Si3. The 'Si3 scaling' mentioned in table 4.6 was calculated as the difference between the two integrals of the fits.

The red square on this plot indicates the number of lost ^{196}Po counts due to the movement of the wheel and is calculated to be 360(19). The square root of these values were taken as error.

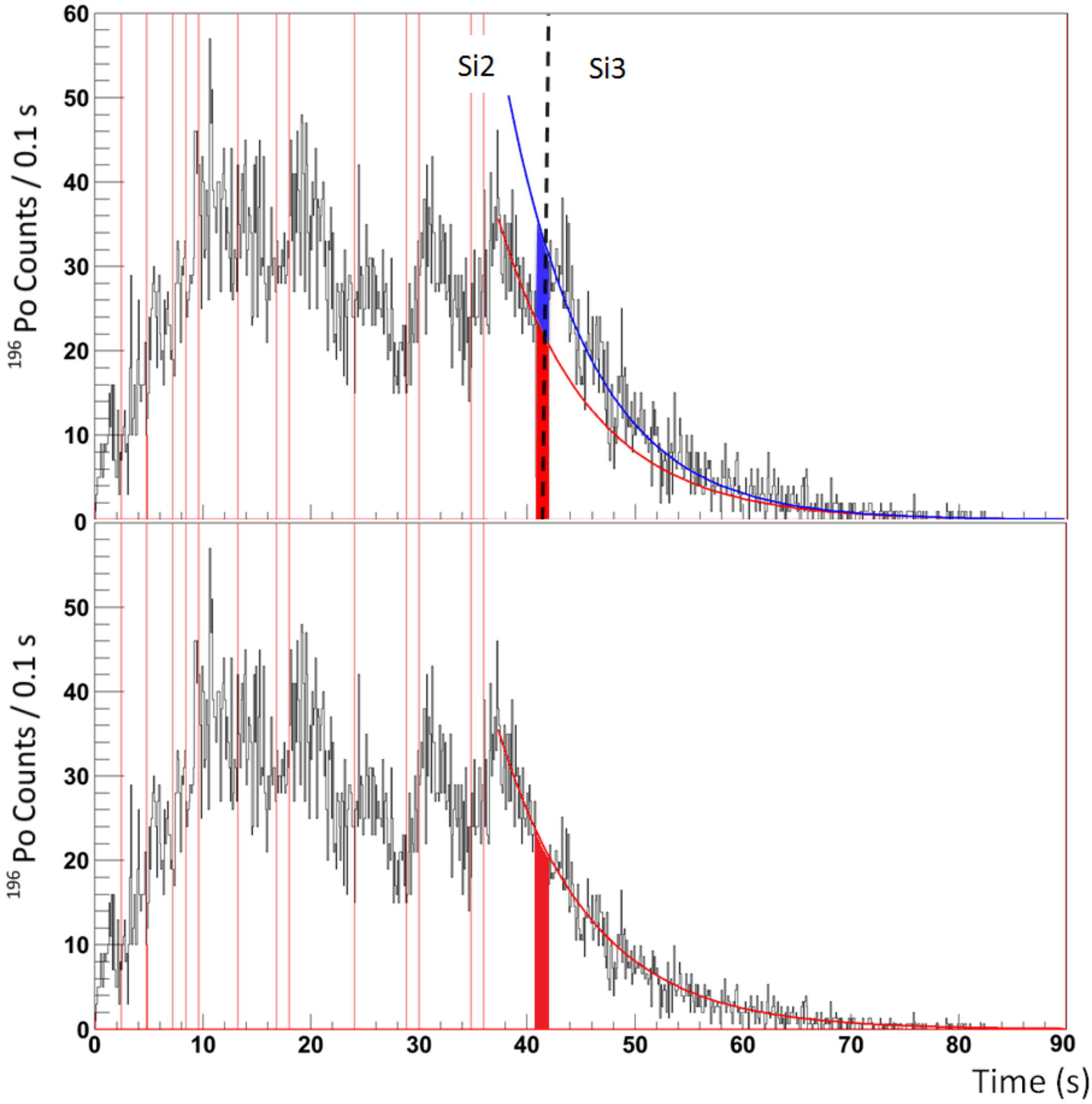

FIGURE 4.20: Count correction due to WM movement (red surface) and scaling (top vs. bottom) for Si2,3 in file 13. Proton pulses are shown as vertical red lines.
Top: Unscaled Si3 counts versus Si2.

4.5 Determination of half lives

The half lives for the produced nuclei can be obtained by fitting the time structure with the exponential decay law (eq.(4.7)).

$$N(t) = N(0)e^{-\lambda t} \tag{4.7}$$

$N(t)$ represents the number of parent nuclei at time t, λ is known as the decay constant and is related to the half life $t_{1/2}$ by $t_{1/2} = ln(2)/\lambda$.

Different elements were selected from the data by putting an energy gate on E_α. A fit for ^{196}Po and ^{192}Bi was taken for data coming from the decay station detectors. The result of this procedure for Po and Bi is shown in figures 4.21 and 4.22. Obtained fit values, literature values and a weighted average of both can be found in table 4.8.
Since ^{196}At is not present anymore at the decay station, the decay behavior has to be extracted from the implantation station. Here, both growth and decay are present. The timing of the experiment was such that the implantation stopped 1 s after an incoming proton pulse. In figure 4.23, proton pulses are shown in red and implantation stops as blue lines on the plot. A pure decay curve is thus guaranteed. In order to get a good fit, a pulse at the end of a measurement cycle was chosen for which the exponential tail was not interrupted by another implantation. Super cycles with the same time structure were added together to improve statistics.

	$t_{1/2}$(s) - (Fit)	$t_{1/2}$(s) - (Lit.)	$t_{1/2}$(s) - (Weighted Av.)
^{196}At	0.373(3)	0.388(14)	0.374(3)
^{196}Po	5.73(11)	5.60(8)	5.64(6)
^{192}Bi	33.2(14)	34.6(9)	34.2(8)

TABLE 4.8: Fitted half lives for ^{196}At, ^{196}Po and ^{192}Bi . Literature values from [2] and a weighted average are also included.

	$t_{1/2}$(s) - (Fit)
At 1	0.38(8)
At 2	0.38(2)
At 3	0.37(4)
At 4	0.372(3)
region D	0.38(2)

TABLE 4.9: Fitted half lives for ^{196}At fine structure peaks.

As can be seen from table 4.8, all fitted half lives agree within error bars with literature values from [2]. The fit value quoted for ^{196}At contained all fine structure peaks in it's energy gate. This was done after checking the agreement between the different peaks. They showed to have equal half-life values within error bars. The comparison for the different peaks can be found in table 4.9.

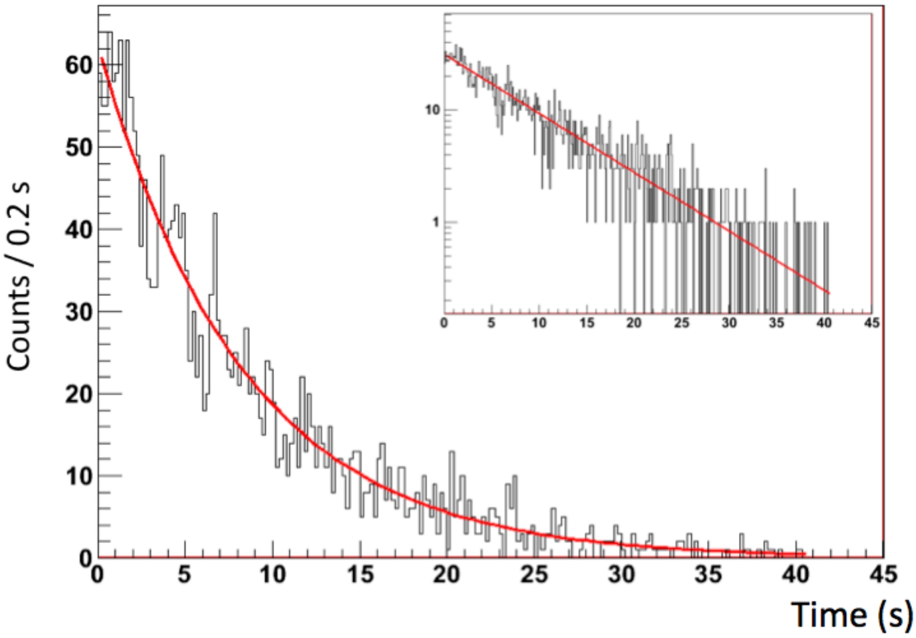

FIGURE 4.21: Fit of half life of ^{196}Po. The same plot on a logarithmic scale is shown in the indent.

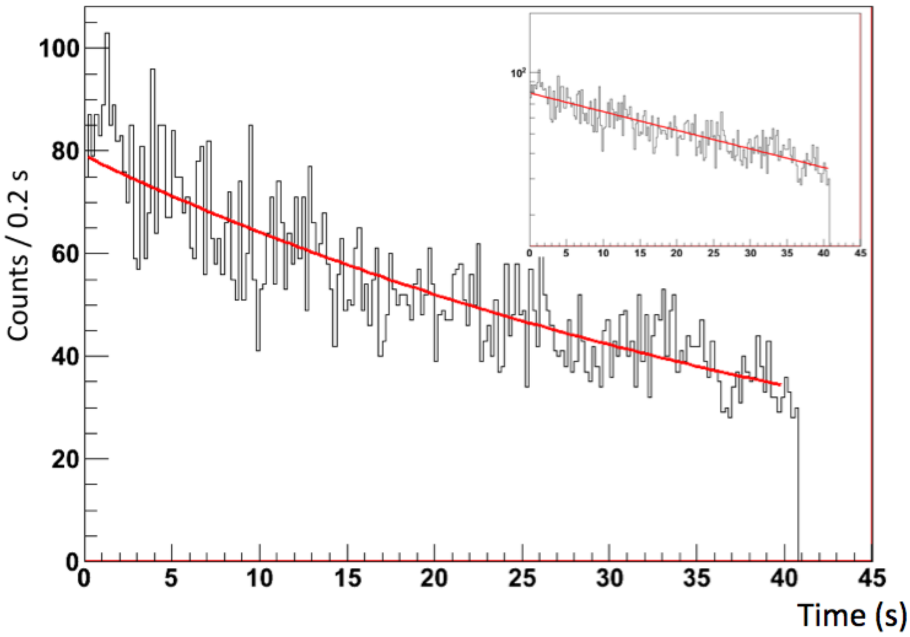

FIGURE 4.22: Fit of half life of ^{192}Bi. The same plot on a logarithmic scale is shown in the indent.

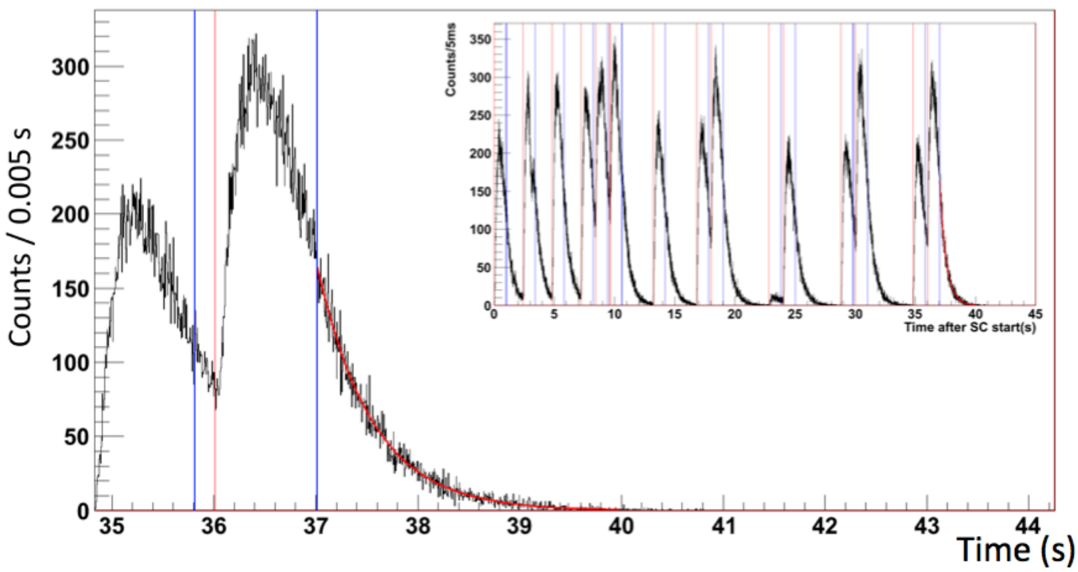

FIGURE 4.23: Fit of half life of ^{196}At. Proton pulses are shown as red lines. Blue lines denote beamgate closing. The indent shows the complete super cycle timing with different implantations and decays after an incoming proton pulse.

Chapter 5

Fission analysis

This chapter deals with the analysis concerning β-delayed fission of ^{194,196}At. The extraction of the probability for βDF, $P_{\beta DF}$, the partial half life $T_{1/2p,\beta DF}$, total kinetic energy (TKE) and fission fragment mass distributions are discussed here. These findings are then compared to what is expected from literature.

5.1 Schmitt calibration

When heavy ions (e.g. fission fragments) are incident on a silicon detector, the measured pulse height,x, does not have the same relationship to the energy as for lighter α particles. This pulse height defect (PHD) was already shortly described in section 3.3.1.1. In order to arrive at the actual energies of the incident heavy particles, Schmitt et al. proposed to add two mass-related terms to the usual linear calibration relationship (E = Ax + B). The function they proposed in [44] is

$$E = (a + a'm)x + (b + b'm), \tag{5.1}$$

where a, a', b, b' are constants for a certain detector operated under constant conditions. Schmitt et al. proposed in the same paper a way to calibrate fission fragment energy spectra using a ^{252}Cf source, by relating the constants a, a', b, b' to the recorded pulse heights for the light and heavy fission fragments. These relationships are quoted in equations (5.2) to (5.5).

$$a = a_0/(P_L - P_H) \tag{5.2}$$
$$a' = a'_0/(P_L - P_H) \tag{5.3}$$
$$b = b_0 - aP_L \tag{5.4}$$
$$b' = b'_0 - a'P_L \tag{5.5}$$

$P_{L,H}$ represents the mean pulse height for the low (L) and heavy (H) fragments respectively. The constants a_0, a'_0, b_0 and b'_0 are called the Schmitt constants and are supposed to be universal for a given detector type. In 1986, Weissenberger et al. re-evaluated these values and found a systematic overestimation of the kinetic energies in the order of 1-2% and they proposed a numerical value for these constants for a specific type of surface barrier detectors. There is a possibility that theses values are not correct for modern surface barrier or PIPS detectors, like the ones used during the βDF experiments discussed in this thesis. Therefore, a, a', b, b' are obtained for our detectors in a preparatory experiment at the Lohengrin accelerator of the Institut Laue-Langevin (ILL) in Grenoble, France. Here, fission fragments that are produced by a neutron induced fission reaction in a fissile source (such as ^{235}U), can be separated according to A/Q and E/Q values by two dipole bending magnets. A, E, Q represent fission fragment mass, energy and charge respectively.
Using the results from this experiment, quoted in an internal report at IKS [45] and the alpha calibration constants for the βDF experiments, values for a, a', b, b' are obtained and shown in table 5.1.

Const.	Annular det.	Full det.
a	1.561 $\times 10^{-3}$	1.509 $\times 10^{-3}$
a'	1.6 $\times 10^{-6}$	1.9 $\times 10^{-6}$
b	-5.8 $\times 10^{-1}$	1.22
b'	3.58 $\times 10^{-2}$	2.20 $\times 10^{-2}$

Table 5.1: Calibration constants used for analysis of the fission fragments. See equation (5.1) for relevant relation to energy and recorded pulse height.

5.2 Determination of mass and TKE distributions

Both fission fragment mass m and energy E in equation (5.1) are unknown. This leaves us with only one equation and two unknowns. In order to arrive at the sought-for mass and energy values, extra equations have to be added. These are found in the kinematics of fission events. The system of equations can be solved, if conservation of mass and momentum are added to the Schmitt calibrations of both fission fragments emitted in a fission event. The resulting set of equations are shown in eq.(5.6)-(5.9).

$$\begin{cases} E_1 = (a_1 + a_1' m_1)x_1 + (b_1 + b_1' m_1) & (5.6) \\ E_2 = (a_2 + a_2' m_2)x_2 + (b_2 + b_2' m_2) & (5.7) \\ 0 = m_1^* E_1^* - m_2^* E_2^* & (5.8) \\ A_f = m_1^* + m_2^* & (5.9) \end{cases}$$

Here E_i, m_i, x_i represent the energy, mass and recorded pulse height of the fission fragment when it hits detector i ($i = 1, 2$). Symbols marked with * denote initial values, before any possible neutron emission has occurred. A_f represents the mass number of the fissioning nucleus.

This system of equations can only be solved if the pulse heights for both fission fragments, $x_{1,2}$, sent out back-to-back in the fission event are detected in coincidence.

The recorded energy E_i of the fission fragments is not simply equal to the initial fragment energy, E_i^*. The energy difference $E_i^* - E_i$ includes energy losses caused by interactions with matter in the carbon foil (see sec 5.3) and the dead layer of the detector, but also possible neutron emission. Also the measured fragment mass m_i might have to be corrected for possible emission of ν_i neutrons. These corrections are summarized in the following equations:

$$\begin{cases} E_i = E_i^* - E_{foil} - E_{dead} - E_{i,\nu} & (5.10) \\ m_i = m_i^* - \nu_i. & (5.11) \end{cases}$$

The effect of the energy loss in the dead layer is already taken into account by using the values for a, a', b, b' obtained from the experiment in ILL. The energy loss due to the passage of the fission fragments trough the carbon foil is explained in section 5.3, and is found to be ∼0.3 MeV and ∼1.2 MeV for fragments detected with the annular and full surface barrier detectors respectively.

Furthermore, neutrons are assumed to be emitted isotropically in the center of mass system of a fission fragment. Therefore, the average fragment velocity does not change. The kinetic energy however does change. The kinetic energy of a fission fragment which has evaporated ν_i neutrons can thus be estimated as $(m_i/m_i^*)E_i^*$.
Using the previous equations, an expression of E_i^* can be found in function of m_i^* and x_i^*:

$$\begin{aligned} E_i^* &= (a_i + a_i'(m^* - \nu_i))x_i + b_i + b_i'(m_i^* - \nu_i) + \Delta E_{i,\nu} + \Delta E_{foil,i} \\ &= (a_i + a_i'(m^* - \nu_i))x_i + b_i + b_i'(m_i^* - \nu_i) + \frac{\nu_i}{m_i^*}E_i^* + \Delta E_{foil,i} \\ &= (a_i/F_i + a_i' m_i^*)x_i + b_i/F_i + b_i' m_i^* + \Delta E_{foil,i} \end{aligned} \tag{5.12}$$

where in equation (5.12) $F_i = 1 - \nu_i/m_i^*$. The set of equations from where the masses m_i^* and E_i^* have to be obtained, can then be written as

$$\begin{cases} E_i = (a_i/F_i + a_i' m_i^*)x_i + b_i/F_i + b_i' m_i^* + \Delta E_{foil,i} & (5.13) \\ 0 = m_1^* E_1^* - m_2^* E_2^* & (5.14) \\ A_f = m_1^* + m_2^* & (5.15) \end{cases}$$

The equations in this section were taken from [13]. Here, also an iterative solution process was proposed. Solving the quadratic equation (5.16) for m_i^* with $F_i = 1$ gives the solution for the case without neutron emission.

$$Am_i^{*2} + Bm_i^* + C = 0 \tag{5.16}$$

In equation 5.16 A, B and C stand for

$$A = a'_1 x_1 + b'_1 - a'_2 x_2 - b'_2 \quad (5.17)$$
$$B = a_1 x_1/F_1 + b_1/F_1 + a_2 x_2/F_2 + 2A_f a'_2 x_2 + 2A_f b'_2 + \Delta E_{foil,1} \quad (5.18)$$
$$C = -A_f(a_2 x_2/F_2 + a'_2 A_f x_2 + b_2/F_2 + A_f b'_2 + \Delta E_{foil,2}). \quad (5.19)$$

Starting from this solution, this equation can be solved for $F_i \neq 1$, whereby at the end of each iteration step, F_i is recalculated until a stable solution is found. In the used method, the end of the iteration was reached when the mass calculation yielded values for m_i^* which only differed by 1/10th of an atomic mass unit for two consecutive steps. In this thesis work, it is assumed that no neutrons are emitted in the βDF of ^{194,196}At. Further analysis should however investigate this possibility.

5.3 SRIM simulations

An important factor to account for when calibrating the fission events, is the energy loss in the carbon foil. At ions are implanted in the 888 Å thick foils. When they undergo βDF, the fission fragments travel trough a certain amount of carbon, losing a non-negligible amount of energy before they even reach the silicon detectors. Simulations were done using a program called SRIM [46].
At first, the implantation depth profile was simulated. This profile was then used to simulate the energy loss of the fission fragments when they move out of the foil and towards the detectors.

5.3.1 Implantation depth

In order to accurately estimate the amount of energy loss in the carbon foils, a reliable knowledge of the ion implantation depth is required. With SRIM, it is possible to simulate the energy loss and stopping range for various ions and initial energies. Here, 10 000 ^{196}At ions impinging on 888 Å thick carbon foils with an incoming energy of 30 keV were simulated. The result of this simulation is shown in figure 5.1.

In figure 5.1, the horizontal (X) direction is the direction of the incoming ions. Ion tracks are shown in white, while red dots correspond to the stopping position of a

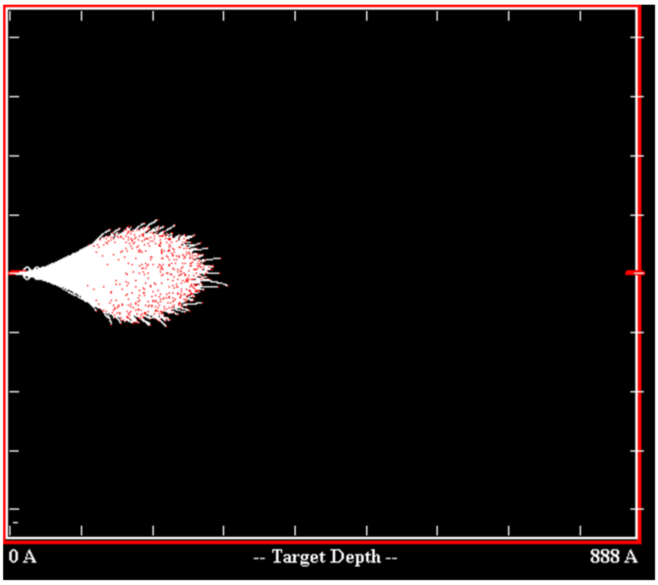

FIGURE 5.1: Simulation of the implantation of 360 keV ^{196}At ions using SRIM.

given ion. Although this figure seems to be only two dimensional, the output provided by SRIM consists of X,Y and Z values of every ion separately.

When a projection is made on the X-axis, the implantation depth profile in the carbon foil is obtained. This profile is presented in figure 5.2. From this projection, the mean implantation depth, $1.8(2)\times10^2$ Å is obtained by calculating the weighted mean of the data. This thus means that the ^{196}At ions are implanted at roughly 1/5th of the carbon foil.

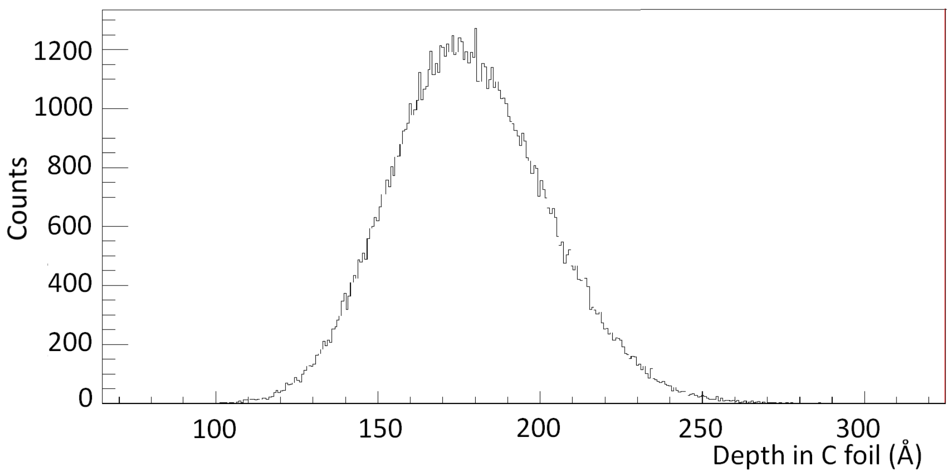

FIGURE 5.2: Projection of SRIM implantation depth

5.3.2 Energy loss of fission fragments in carbon foil

To simulate the energy loss of the fission fragments in the carbon foil, the simulation results from section 5.3.1 were used. The implantation depths were used as input for the starting depths in the next simulation, where ^{98}Mo ions were expelled from the carbon foil with an initial energy of 77 MeV. ^{98}Mo ions were used, since they are the resulting fragments of a symmetric split of ^{196}Po. An energy of 77 MeV was used, because this value is roughly half of the total kinetic energy found for coincident fission events in the silicon detectors.

In order to simulate the energy loss as accurately as possible, the implanted ions were distributed randomly over the surface of the beam spot, which was taken to be 6 mm. From figure 5.1, it can be seen that the implanted At ions are vertically contained within a 200 Å range. This thus means that the implantation itself does not have a significant influence on the position perpendicular to the beam direction and the randomization over 6 mm is allowed. The randomization was done using rejection sampling, where random points on square surface are picked, but only accepted when these points are found within the circular surface. The result is shown in figure 5.3. The implantation depths were unchanged. The fission process is expected to be isotropic in space. In order to simulate this, the angles of emission were also randomized, which is shown on a unit sphere in figure 5.4.

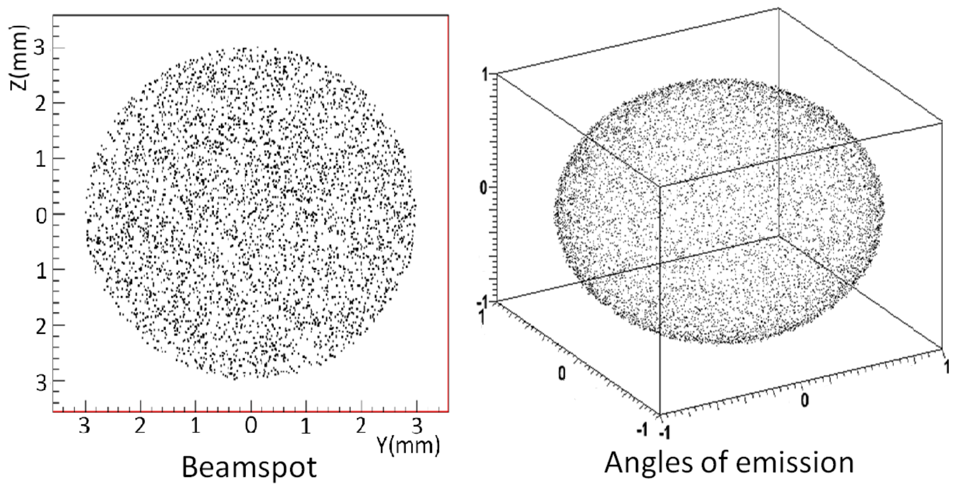

FIGURE 5.3: Randomization of beamspot and emission angles.

Using these random starting points on the beam spot, random angles of emission and simulated implantation depths, the energy loss can be simulated using SRIM. In order to determine the average energy losses for the detected fission fragments, the geometry of the setup has to be considered. A visual representation of the simulation is shown in figure 5.4. Points in red on this figure, represent fission fragments detected in the full surface barrier detector which had a coincident partner in the annular detector. The lines represented on the figure, stand for different possibilities when only one of the fission fragments is detected. The red line shows the example of an event in which a fission fragment is detected on the full detector, but for which the partner fragment falls outside of the annular detector range. The black line shows a similar event, for which one of the partner fragments is missed in the detector, since it passes trough the hole in the annular detector. An event for which one of the fission fragments hits the annular detector but misses the full detector is shown in green.

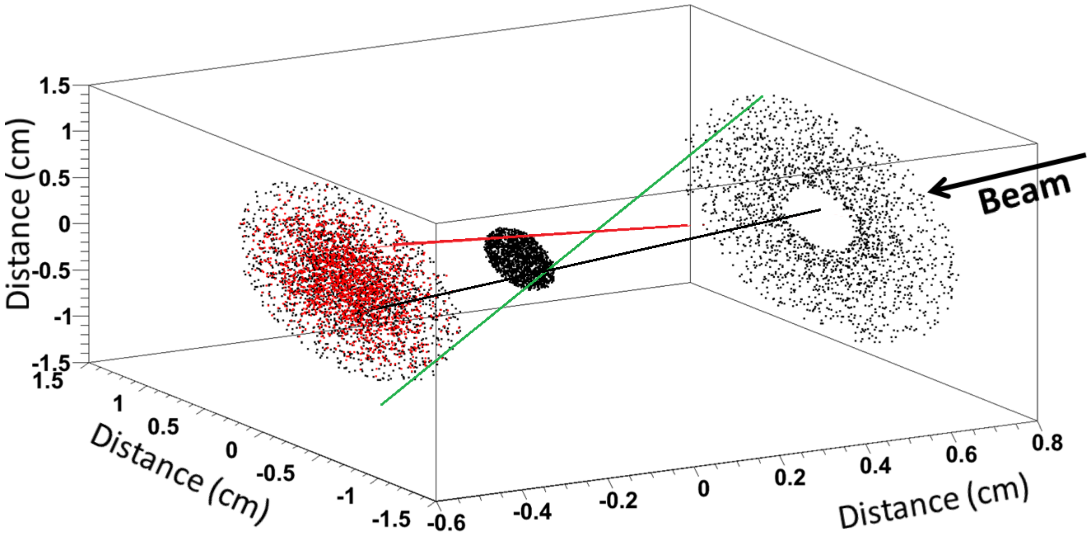

FIGURE 5.4: Visual representation of the SRIM simulation used to calculate the fission fragment energy loss in the carbon foil.

Since the total kinetic energy can only be obtained for coincident fission events, the simulated energy losses for events where no, or only one fission fragment is incident on a detector, were not considered. The resulting ion energy for detected fragments in both the annular and full Si detector are shown in figure 5.5. These energies can then be compared to the initial energy of 77 MeV in order to describe the energy loss in the carbon foil.

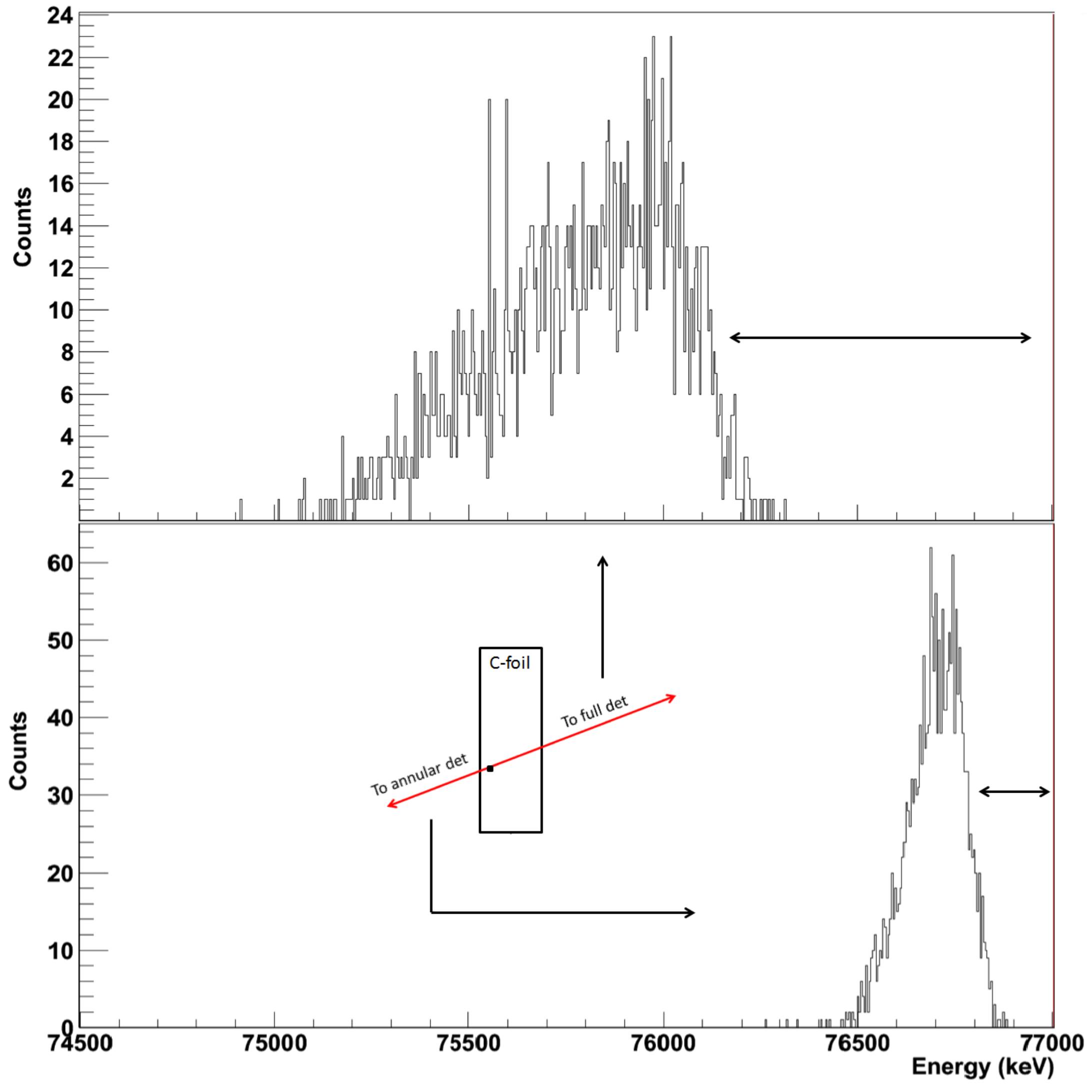

FIGURE 5.5: Energy of the simulated ^{98}Mo ions as they hit the the full (top) and annular (bottom) detector. The ions started in the simulated implantation sites in the carbon foil with an enery of 77 MeV, shown as the most-right border.

From these figures, the average energy that is lost by the fission fragments when moving through the carbon foil is found to be 0,30(8) MeV for fragments detected in the annular detector, and 1,2(3) MeV for fragments that hit the full detector.

5.4 Discussion of mass and TKE distributions

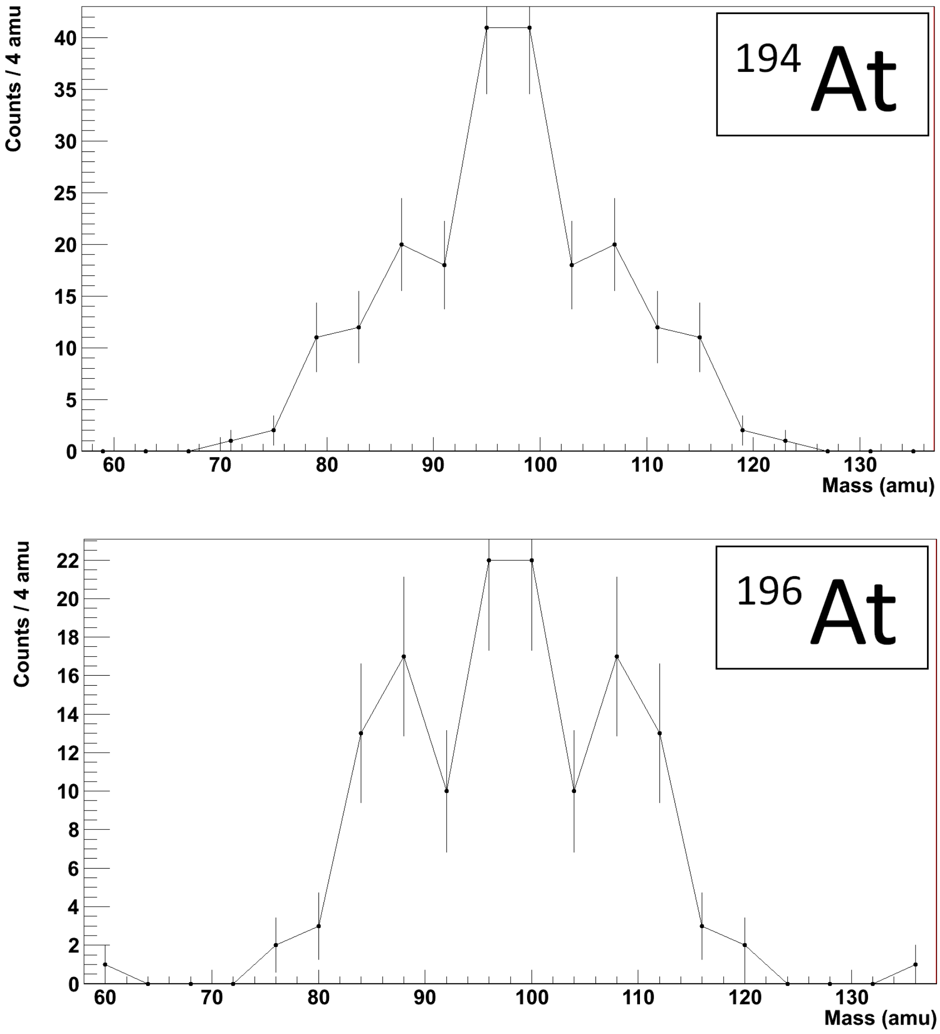

FIGURE 5.6: Mass distributions of ^{194,196}At

The mass distributions after βDF of ^{194,196}At, obtained via the equations described in the previous sections, are shown in figure 5.6. Both isotopes show a clear symmetric fission component, seen from the large central peak in their mass distributions. Besides this symmetric part, also an significant amount of asymmetric fission can be observed in both cases. Furthermore, the ratio of the amount of symmetric fission to asymmetric fission, seems to differ for both isotopes.

If the Z/N ratios are the same in the resulting fission fragments as in the fissioning nucleus, the detected nuclei are distributed around ^{98}Mo for the symmetric split, and ^{88}Sr , ^{108}Pd for the possible asymmetric fission of ^{196}Po. A symmetric split of ^{194}Po would result in two ^{97}Mo nuclei, but from the spectrum shown in figure 5.6, it is not clear around which nuclei asymmetric fission would be distributed.

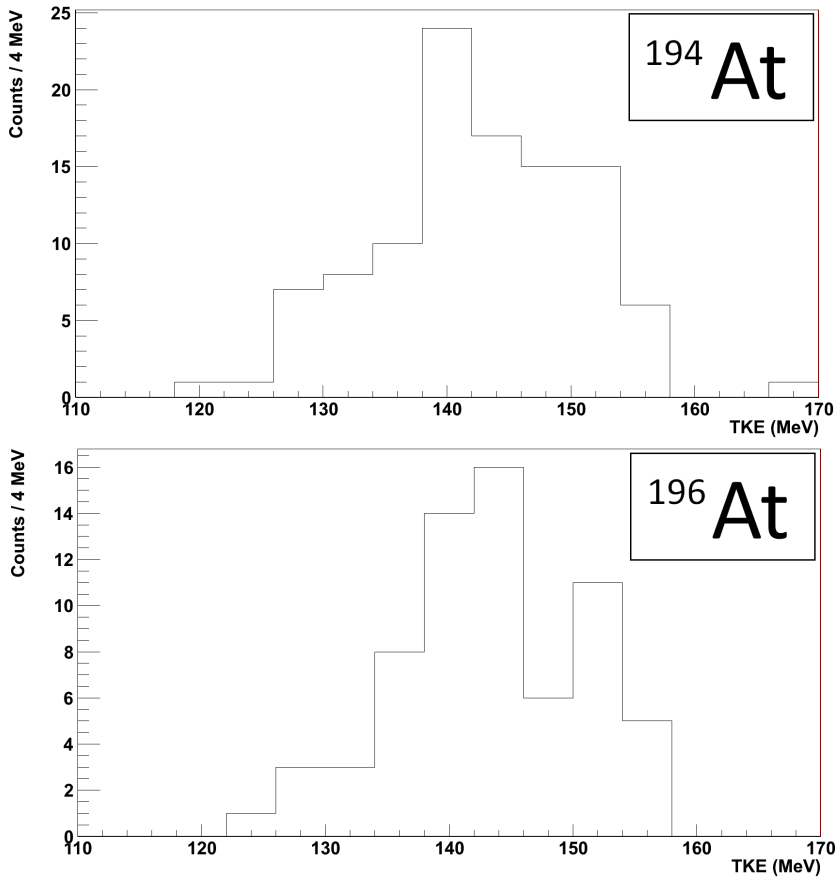

FIGURE 5.7: TKE distributions of ^{194,196}At

The TKE distributions of ^{194,196}At are shown in figure 5.7. The TKE of ^{196}At clearly shows a double-humped shape. When the mass distributions for fission events above and below 148 MeV are plotted, two very different shapes emerge. While the mass distribution corresponding to the high TKE shows to be very narrow and symmetric (A$\sim$98), the mass distribution corresponding to the low-TKE gate is very broad symmetric, or might even be asymmetric. The two different fission modes are shown in figure 5.8, and can also be recognized in figure 5.10. It is in principle possible that two different isomers might exhibit different fission behavior, but this is most likely not the case in ^{196}At, since it was already argued in section 4.3.4 that only one isomer of ^{192}Bi was populated.

While for ^{194}At no clear double-peaked structure in the TKE-distribution is seen, a similar behavior is found in the mass distributions when selecting fission fragments

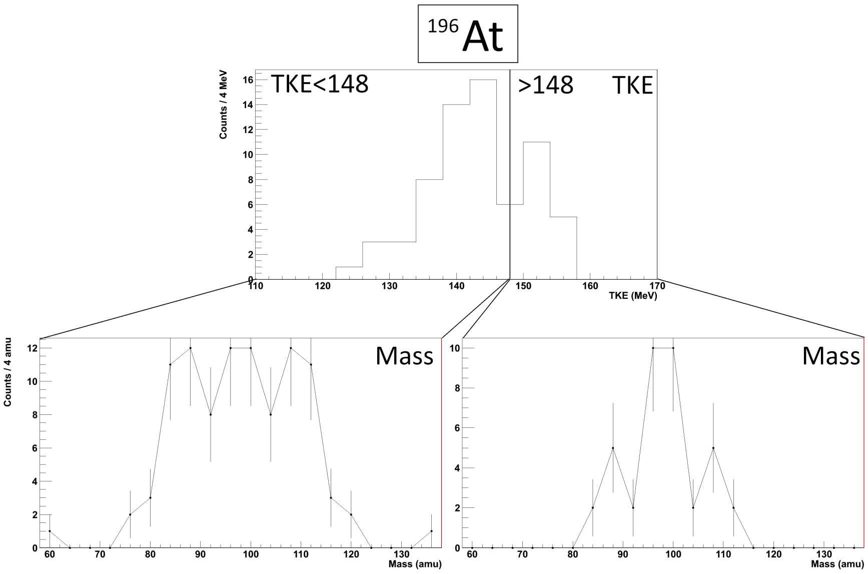

FIGURE 5.8: Mass distributions of ^{196}At gating on TKE lower or higher then 148 MeV

with a TKE higher or lower than 148 MeV. As in the case of ^{196}At, the high-TKE part also corresponds to a narrow symmetric distribution, while the low-TKE gate reveals a broad symmetric mass distribution. This is shown in figure 5.9. Two distinct modes of fission are thus also found in the case of ^{194}At. However, this nucleus is known to have at least two isomers with an appreciable half life of 40 ms and 250 ms [2]. The fission properties can thus not be disentangled with this experiment.

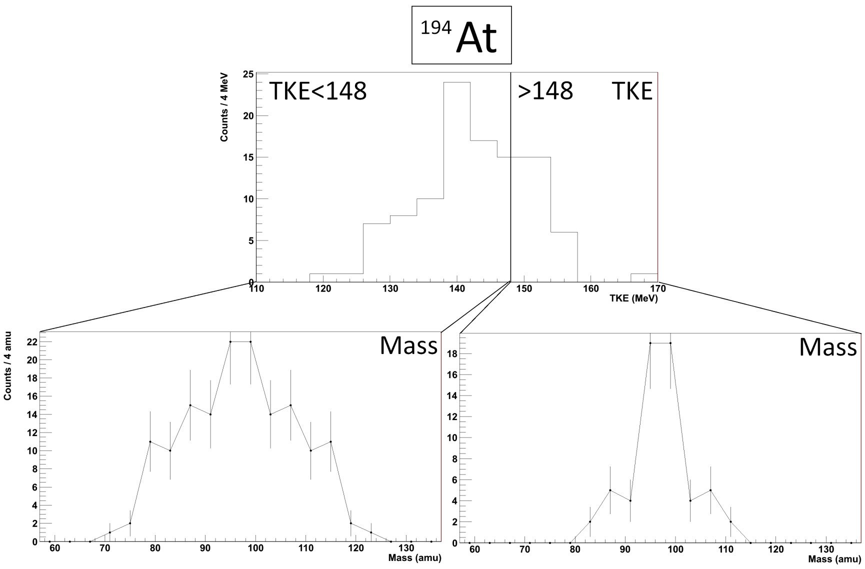

FIGURE 5.9: Mass distributions of ^{194}At gating on TKE lower or higher then 148 MeV

Figures 5.10 and 5.11 show a 3D representation of the fission data, where the fragment masses are compared to the TKE. In each figure, also the top view is presented. The trends that were discussed are clearly showing. For higher TKE's, the mass distributions show to be much more narrow than for the low TKE parts.

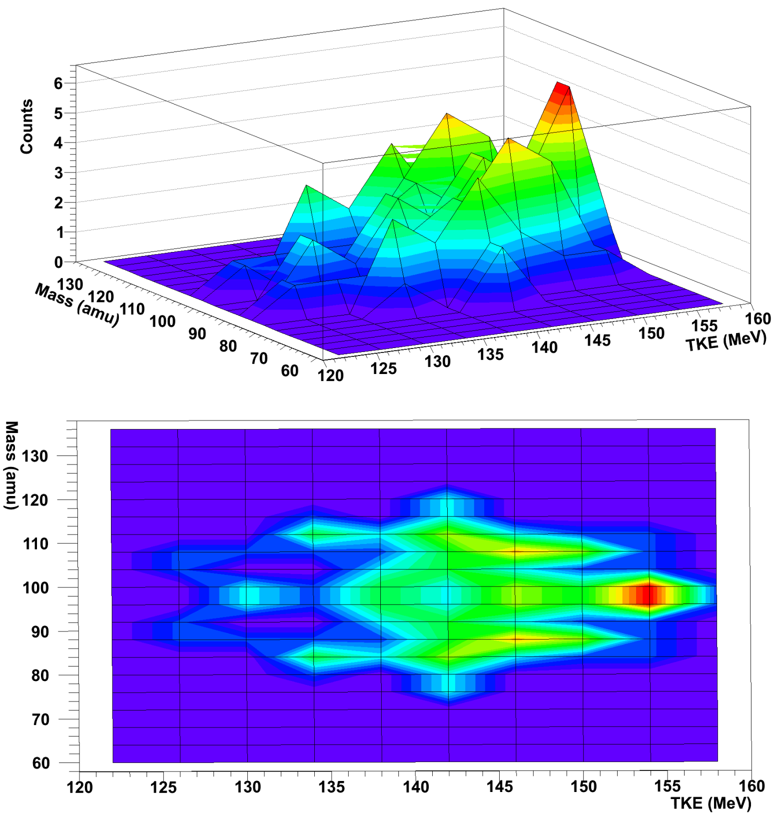

FIGURE 5.10: 3D representation of mass and TKE distributions of ^{196}At

The TKE and mass distributions are also fitted with Gaussians and the results are shown in table 5.2. These values can be compared to the Viola systematics, which were discussed in section 1.3.3.1. As can be seen from figure 5.12, where the results of this thesis are added to the rest of the data, the studied nuclei seem to agree very well with this systematic behavior. On the plot, two different values for the TKE of ^{196}At are displayed. These correspond to the different total kinetic energies observed for both fission modes.

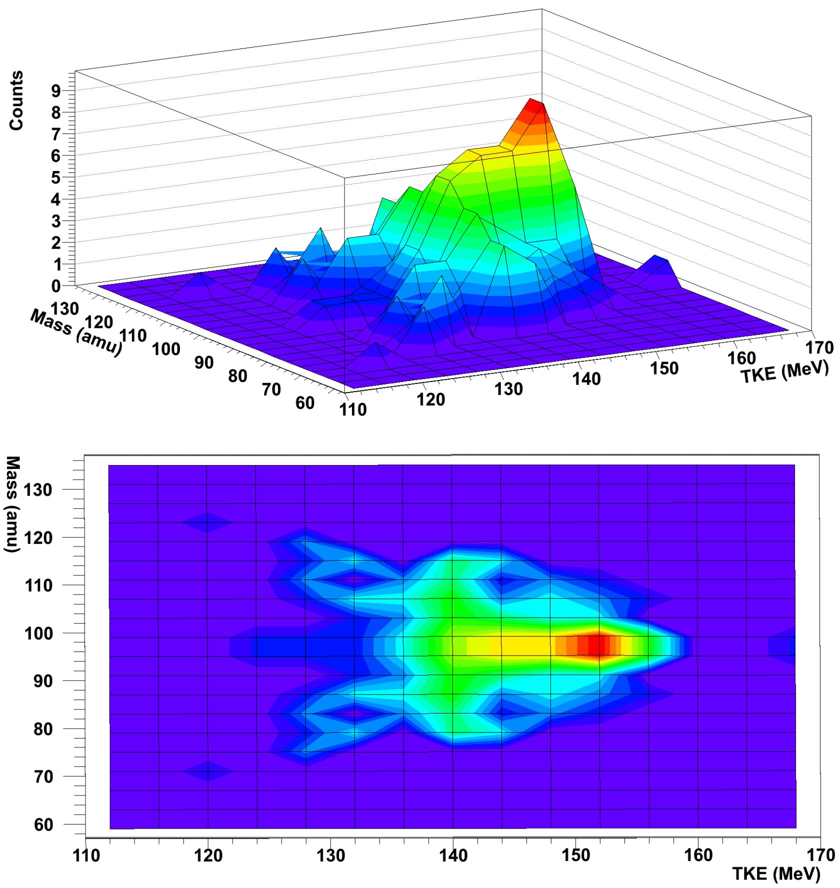

FIGURE 5.11: 3D representation of mass and TKE distributions of ^{194}At

	^{196}At		^{194}At	
	μ	σ	μ	σ
High TKE (MeV)	152(1)	3(1)	-	-
Low TKE (MeV)	142(1)	3(1)	-	-
Overall TKE (MeV)	143(1)	8(1)	142(1)	8(1)
Heavy mass (amu)	108.3(7)	3(1)	-	-
Light mass (amu)	88.7(7)	3(1)	-	-
Central mass (amu)	98.0(5)	2.3(5)	97.0(5)	2.5(3)
Broad mass (amu)	-	-	97(2)	15(3)

TABLE 5.2: Fit results for TKE and mass distribution of ^{194,196}At.

5.5 $P_{\beta DF}$ and $T_{1/2p,\beta DF}$ of ^{196}At

In order to obtain the probability for βDF, $P_{\beta DF}$ and the partial half life $T_{1/2p,\beta DF}$, the correct amount of fission events, ^{196}At α decays and the β branching ratio has to be known. From the data collected on 2011 with HRS, the beta branch, b_β can be calculated accurately, as was done in section 4.4.

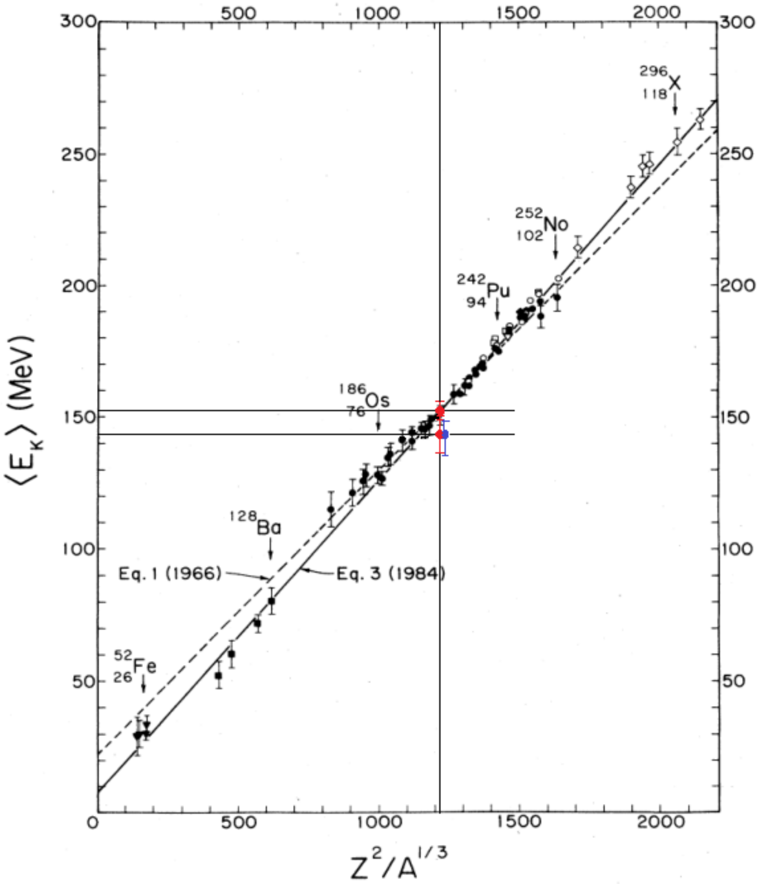

FIGURE 5.12: Viola plot with ^{194,196}At shown in blue and red respectively.

The fine structure decay of ^{196}At, which is clearly present in the 2011 data, is buried under the contamination peaks in the 2012 data. This means that the only the 7049 keV ^{196}At peak is visible in the 2012 GPS data. The ratio,R, of the 7049 keV ^{196}At peak to the total amount of ^{196}At α decays can also be calculated from the HRS data and is found to be 98.2(1)%.

Data set	Si1	Si2	Coincident	fission events	meas. time (h)
(HRS) ^{196}At	3	5	3	5	~ 1
(GPS) ^{196}At	92	181	67	206	~ 35
(GPS) ^{194}At	132	253	105	280	~ 9

TABLE 5.3: Number of observed fission events of ^{194,196}At for GPS and HRS data.

In table 5.3, the amount of fission fragments observed in each Si detector for the different experiments and isotopes are shown. The amount of fission *events* was calculated as N_F(Si1)+N_F(Si2)-N_C, where N_F represents the numbers of fission *fragments* and

N_C represents the number of observed coincidences. An estimate of the measurement time is also given here. Using this ratio R, and the β branch b_β, calculated from the HRS data, $P_{\beta DF}$ can be calculated from the GPS data using the number of observed fission events, F and the amount of α decay counts in the large ^{196}At peak, C. The formulas used to calculate $P_{\beta DF}$ and $T_{1/2p,\beta DF}$ are

$$P_{\beta DF} = \frac{F/2}{\frac{C}{R}\frac{b_\beta}{(1-b_\beta)}} \tag{5.20}$$

$$T_{1/2p,\beta DF} = \frac{T_{1/2,\text{tot}}}{b_\beta \times P_{\beta DF}} \tag{5.21}$$

The factor of 1/2 in the numerator of equation 5.20 accounts for the fact that two separate fission fragments are emitted in comparison to only one α particle. The fraction $\frac{C}{R(1-b_\beta)}$ in the denominator equals the amount of observed decays of ^{196}At. In order to arrive at the number of β decays of ^{196}At, this number is then multiplied by the beta branch b_β. Since there are two separate data sets (2011 with HRS and 2012 with GPS), $P_{\beta DF}$ can be calculated and compared for both sets. The obtained values using the formula given in equation 5.20 are shown in table 5.4. For the calculation of $P_{\beta DF}$ and $T_{1/2p,\beta DF}$, only the fragments detected in Si2 are used. This was done, since for this detector, the efficiency for detecting an α particle is easily understood as being half of the detection efficiency of a fission event and most of the recorded fission events are registered in Si2, as can be seen from table 5.3.

Data set	$P_{\beta DF}$	$T_{1/2p,\beta DF}$ (s)
GPS	$9(1)\ \times 10^{-5}$	$1.7(2)\ \times 10^{5}$
HRS	$13^{+6}_{-5}\ \times 10^{-5}$	$1.2^{+8}_{-4}\ \times 10^{5}$

TABLE 5.4: Values for $P_{\beta DF}$ and $T_{1/2p,\beta DF}$ of ^{196}At for GPS and HRS data.

Both experiments are thus in agreement with each other. The large error on the HRS values originates from low statistics, since only 5 fission events were observed. Furthermore, this error cannot simply be estimated by the square root, since a Gaussian approximation of the data is not valid. Therefore, asymmetric 1σ errors proposed by [47] were used.

The number of α decay counts in the main ^{196}At peak used to calculate the GPS values shown in table 5.4 was obtained by fitting the peak in the energy spectrum of Si2. Since various fitting functions returned various differing integral values, an average of all procedures was taken and the error on the value was chosen to include every fit result. The peaks were fitted with α peak fitting functions as described in section 4.2 for one, two and three exponential tails. Also, the integral inside the energy-borders of 6900-7100 keV was taken. In order to include all possible count numbers, the average was taken and the error was enlarged. The final value that was used was 3.9(3)$\times 10^7$ counts.

The results shown in table 5.4 can be compared to other data, as is done in figure 5.13. The measured $T_{1/2p,\beta DF}$ of 196At, shown in yellow, seems to follow the trend that was set by previously studied isotopes rather well and forms the first additional result to the two values of the Tl isotopes reported before for the lead region. The 196At results seems to confirm the systematic dependence of the partial βDF half life on the $Q_{EC} - B_f$ values when using the calculations of TF. Further experimental data are needed to put this on a proper footing. Calculations using other models for the prediction of Q_{EC} and B_f are underway in order to understand these intriguing phenomena.

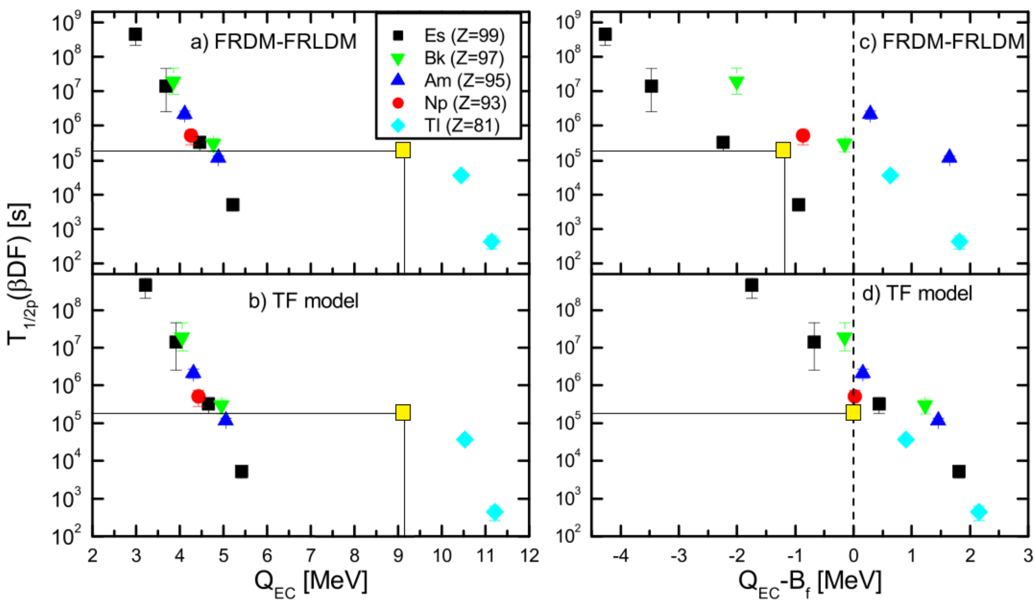

FIGURE 5.13: Plot with $T_{1/2p,\beta DF}$ systematics including ^{196}At in yellow. Original plot taken from [3].

Chapter 6

Conclusion

In this thesis, radioactive ^{194,196}At nuclei were studied. In the β decay process of these nuclei, excited states in the daughter nucleus can be populated, which have the possibility to undergo fission if their excitation energy is similar to or larger than the so-called fission barrier. This two-step process is called β-delayed fission(βDF). Next to the βDF of ^{194,196}At, the alpha-decay spectroscopy of ^{196}At was investigated. The data that was analyzed was the result of two experiments which were done at the ISOLDE facility in CERN, Geneva in May 2011 and May 2012. Here, the studied At isotopes were created and led into the so-called Windmill detection system, where the ions were implanted in carbon foils. Silicon and Germanium detectors surrounding these foils were used to measure the decay properties of the produced nuclei, by observing the α, β particles, fission fragments, γ- and X-rays.

The first part of the analysis done in this thesis, consists of the α-decay study of ^{196}At. Here, previously unknown fine structure decay of ^{196}At was observed. By studying the γ rays observed in coincidence with these α lines, a preliminary decay scheme for ^{192}Bi could be constructed. Reduced α widths for several α decays from the ground state of ^{196}At to states in ^{192}Bi were calculated. Several issues concerning the decay scheme mentioned in the text are yet unsolved and a deeper study is necessary. In this section, it was also argued that predominantly the 3^+ isomer of ^{192}Bi was populated, indicating that only the decay of the ground state of ^{196}At was observed. Decay of a high-spin isomer of ^{196}At was not observed. From the weakly or unhindered α decay of the ^{196}At ground state, it can be deduced that the ^{192}Bi(3+) state and the ground state of ^{196}At have the same spin and parity. Furthermore, the β branch b_β of ^{196}At was found to be 2.4(1)%. This calculated value was later used in the fission analysis to calculate the probability for βDF, $P_{\beta DF}$. Finally, the half lives of the produced isotopes ^{196}At, ^{196}Po and ^{192}Bi were measured and compared to literature.

The second part of this thesis consisted of the βDF study of ^{194,196}At. Here, the total kinetic energy (TKE) and mass distributions for the coincident fission fragments are extracted. Furthermore, simulations were done with SRIM to account for energy loss by the fission fragments in the carbon foil. The resulting mass distributions indicate a transition region between asymmetric fission, as observed in the βDF of ^{178,180}Tl and symmetric fission, as observed in coulex-induced fission studies of ^{204}Rn. When gating on the peaks of the double-peaked structure in the TKE distribution of ^{196}At, two very different fission modes are observed. A narrow and symmetric fission mode is observed for a TKE $>$148 MeV. A broad mass distribution is observed for lower TKE's. The centroids are situated around 152 and 142 MeV respectively. A similar feature was recognized in the βDF of ^{194}At. In contrast to ^{196}At, however, two isomers of ^{194}At are expected to be produced. In addition, the probability for βDF, $P_{\beta DF}$, and the partial half-life for βDF $T_{1/2p,\beta DF}$ are calculated for ^{196}At from both the 2011 and 2012 data set, which was found to be consistent. A value of 9(1)$\times 10^{-5}$ for $P_{\beta DF}$ and 1.7(2)$\times 10^{5}$ s for $T_{1/2p,\beta DF}$ are obtained. The TKE and $T_{1/2p,\beta DF}$ of ^{196}At are found to be in agreement with the systematic trends observed in other nuclei using the TF model for calculating the Q_{EC} and B_f values.

The α-decay spectroscopy in this thesis should be extended in order to present a final version of the ^{192}Bi level scheme. Multipolarities of different transitions and spin/parities of the levels could possibly be deduced. The βDF results (TKE, mass distributions, two fission modes) are now available for comparison with different theories. Especially the observation of two types of fission in ^{196}At will be challenging to explain. Since the experiments described in this thesis are part of an experimental campaign studying βDF of several isotopes in the neutron-deficient lead region, the results could be compared to the findings in the other studied elements in this area. The data obtained for ^{200,202}Fr isotopes for instance, are currently being analyzed. A study of the βDF behavior of different isomers would yield interesting information on the spin-sensitivity of low-energy fission. In order to do this, an isomerically pure beam of e.g. ^{194}At could possibly be produced, if a difference in hyperfine splitting in e.g. ^{194}At isomers is observed.

Bibliography

[1] K.S. Krane. *Introductory Nuclear Physics*. John Wiley & Sons, 1988.

[2] National nuclear data center (nndc), 2013. URL http://www.nndc.bnl.gov/.

[3] A. Andreyev, M. Huyse, and P. Van Duppen. Colloquium: Beta-delayed fission of atomic nuclei. *Review of Modern Physics, to be published*.

[4] C. Wagemans. *The Nuclear Fission Process*. CRC Press, 1991.

[5] S. Bjørnholm and J. E. Lynn. The double-humped fission barrier. *Rev. Mod. Phys.*, 52:725–931, Oct 1980. doi: 10.1103/RevModPhys.52.725. URL http://link.aps.org/doi/10.1103/RevModPhys.52.725.

[6] K.-H. Schmidt, J. Benlliure, and A.R. Junghans. Fission of nuclei far from stability. *Nuclear Physics A*, 693(12):169 – 189, 2001. ISSN 0375-9474. doi: 10.1016/S0375-9474(01)00648-0. URL http://www.sciencedirect.com/science/article/pii/S0375947401006480. ¡ce:title¿Radioactive Nuclear Beams¡/ce:title¿.

[7] E. K. Hulet, J. F. Wild, R. J. Dougan, R. W. Lougheed, J. H. Landrum, A. D. Dougan, M. Schadel, R. L. Hahn, P. A. Baisden, C. M. Henderson, R. J. Dupzyk, K. Sümmerer, and G. R. Bethune. Bimodal symmetric fission observed in the heaviest elements. *Phys. Rev. Lett.*, 56:313–316, Jan 1986. doi: 10.1103/PhysRevLett.56.313. URL http://link.aps.org/doi/10.1103/PhysRevLett.56.313.

[8] P. Möller, A.J. Sierk, T. Ichikawa, A. Iwamoto, R. Bengtsson, H. Uhrenholt, and S. Åberg. Heavy-element fission barriers. *Phys. Rev. C*, 79:064304, Jun 2009. doi: 10.1103/PhysRevC.79.064304. URL http://link.aps.org/doi/10.1103/PhysRevC.79.064304.

[9] K. F. Flynn, E. P. Horwitz, C. A. A. Bloomquist, R. F. Barnes, R. K. Sjoblom, P. R. Fields, and L. E. Glendenin. Distribution of mass in the spontaneous fission of ^{256}Fm. *Phys. Rev. C*, 5:1725–1729, May 1972. doi: 10.1103/PhysRevC.5.1725. URL http://link.aps.org/doi/10.1103/PhysRevC.5.1725.

[10] P. Möller, D.G. Madland, A.J. Sierk, and A. Iwamoto. Nuclear fission modes and fragment mass asymmetries in a five-dimensional deformation space. *Nature*, 409:785 – 790, Feb 2001. URL http://dx.doi.org/10.1038/35057204.

[11] T. Ichikawa, A. Iwamoto, P. Möller, and A.J. Sierk. Contrasting fission potential-energy structure of actinides and mercury isotopes. *Phys. Rev. C*, 86:024610, Aug 2012. doi: 10.1103/PhysRevC.86.024610. URL http://link.aps.org/doi/10.1103/PhysRevC.86.024610.

[12] P. Möller, J. Randrup, and A.J. Sierk. Calculated fission yields of neutron-deficient mercury isotopes. *Phys. Rev. C*, 85:024306, Feb 2012. doi: 10.1103/PhysRevC.85.024306. URL http://link.aps.org/doi/10.1103/PhysRevC.85.024306.

[13] J. Elseviers. Electron capture delayed fission of ^{180}Tl. Master's thesis, IKS, KULeuven, 2011. URL http://fys.kuleuven.be/iks/ns/phd-master-theses.

[14] D. A. Shaughnessy, K. E. Gregorich, J. L. Adams, M. R. Lane, C. A. Laue, D. M. Lee, C. A. McGrath, V. Ninov, J. B. Patin, D. A. Strellis, E. R. Sylwester, P. A. Wilk, and D. C. Hoffman. Electron-capture delayed fission properties of ^{244}Es. *Phys. Rev. C*, 65:024612, Jan 2002. doi: 10.1103/PhysRevC.65.024612. URL http://link.aps.org/doi/10.1103/PhysRevC.65.024612.

[15] V. E. Viola, K. Kwiatkowski, and M. Walker. Systematics of fission fragment total kinetic energy release. *Phys. Rev. C*, 31:1550–1552, Apr 1985. doi: 10.1103/PhysRevC.31.1550. URL http://link.aps.org/doi/10.1103/PhysRevC.31.1550.

[16] I.V. Panov, E. Kolbe, B. Pfeiffer, T. Rauscher, K.-L. Kratz, and F.-K. Thielemann. Calculations of fission rates for r-process nucleosynthesis. *Nuclear Physics A*, 747(24):633 – 654, 2005. ISSN 0375-9474. doi: 10.1016/j.nuclphysa.2004.09.115. URL http://www.sciencedirect.com/science/article/pii/S0375947404010255.

[17] P. Moller, J.R. Nix, W.D. Myers, and W.J. Swiatecki. Nuclear ground-state masses and deformations. *Atomic Data and Nuclear Data Tables*, 59(2):185 – 381, 1995. ISSN 0092-640X. doi: 10.1006/adnd.1995.1002. URL http://www.sciencedirect.com/science/article/pii/S0092640X85710029.

[18] W. D. Myers and W. J. Świątecki. Table of nuclear masses according to the 1994 thomas-fermi model. Lawrence Berkeley Laboratory Report No. LBL-36803, 1994. URL http://ie.lbl.gov/toimass.html.

[19] W. D. Myers and W. J. Świątecki. Thomas-fermi fission barriers. *Phys. Rev. C*, 60:014606, Jun 1999. doi: 10.1103/PhysRevC.60.014606. URL http://link.aps.org/doi/10.1103/PhysRevC.60.014606.

[20] S. Rothe et al. Measurement of the first ionization potential of astatine by laser ionization spectroscopy. *Nat. Commun.*, 4:1835, 2013. doi: 10.1038/ncomms2819. URL http://dx.doi.org/10.1038/ncomms2819.

[21] M B Smith, R Chapman, J F C Cocks, K-M Spohr, O Dorvaux, K Helariutta, P M Jones, R Julin, S Juutinen, H Kankaanp, H Kettunen, P Kuusiniemi, Y Le Coz, M Leino, D J Middleton, M Muikku, P Nieminen, P Rahkila, and A Savelius. Isomeric state in the doubly odd 196 at nucleus. *Journal of Physics G: Nuclear and Particle Physics*, 26(6):787, 2000. URL http://stacks.iop.org/0954-3899/26/i=6/a=303.

[22] A. N. Andreyev, J. Elseviers, M. Huyse, P. Van Duppen, S. Antalic, A. Barzakh, N. Bree, T. E. Cocolios, V. F. Comas, J. Diriken, D. Fedorov, V. Fedosseev, S. Franchoo, J. A. Heredia, O. Ivanov, U. Köster, B. A. Marsh, K. Nishio, R. D. Page, N. Patronis, M. Seliverstov, I. Tsekhanovich, P. Van den Bergh, J. Van De Walle, M. Venhart, S. Vermote, M. Veselsky, C. Wagemans, T. Ichikawa, A. Iwamoto, P. Möller, and A. J. Sierk. New type of asymmetric fission in proton-rich nuclei. *Phys. Rev. Lett.*, 105:252502, Dec 2010. doi: 10.1103/PhysRevLett.105.252502. URL http://link.aps.org/doi/10.1103/PhysRevLett.105.252502.

[23] A Andreyev, V Liberati, J Lane, K Sandhu, R Chapman, IG Darby, J Diriken, H De Witte, J Elseviers, M Huyse, L Ghys, E Rapisarda, D Radulov, P Van den Bergh, P Van Duppen, KT Flanagan, L Popescu, D Pauwels, S Antalic, Z Kalaninova, K Nishio, U Kster, RD Page, I Tsekhanovich, S Vermote, C Wagemans, M Venhart, M Veselsky, P Möller, AJ Sierk, T Itchikawa, and TE Cocolios.

Detailed bdf studies of 202fr and a search for bdf of 204fr: Addendum to the proposal is466: Identification and systematic studies of the beta-delayed fission (bdf) in the lead region. Technical Report CERN-INTC-2011-006. INTC-P-235-ADD-2, CERN, Geneva, Jan 2011. URL http://cds.cern.ch/record/1319032/export/hx?ln=en.

[24] Andrei Andreyev, Piet Van Duppen, and Valentine Fedosseev. Beta-delayed fission, laser spectroscopy and shape-coexistence studies with radioactive at beams. Technical Report CERN-INTC-2012-001. INTC-P-319, CERN, Geneva, Jan 2012. URL http://cds.cern.ch/record/1410652?ln=en.

[25] A. V. Andreev, G. G. Adamian, and N. V. Antonenko. Mass distributions for induced fission of different hg isotopes. *Phys. Rev. C*, 86:044315, Oct 2012. doi: 10.1103/PhysRevC.86.044315. URL http://link.aps.org/doi/10.1103/PhysRevC.86.044315.

[26] M. Warda, A. Staszczak, and W. Nazarewicz. Fission modes of mercury isotopes. *Phys. Rev. C*, 86:024601, Aug 2012. doi: 10.1103/PhysRevC.86.024601. URL http://link.aps.org/doi/10.1103/PhysRevC.86.024601.

[27] V. Liberati, A. Andreyev, M. Antalic, S. en nog veel meer Huyse, and P. Van Duppen. Beta-delayed fission and alpha decay of ^{178}Tl. *Phys. Rev. C, to be published*, 2013.

[28] A. et al. Andreyev. A triplet of differently shaped spin-zero states in the atomic nucleus 186pb. *Nature*, 405:430–433, May 2000. URL http://dx.doi.org/10.1038/35013012.

[29] Michael R. Zalutsky, David A. Reardon, Gamal Akabani, R. Edward Coleman, Allan H. Friedman, Henry S. Friedman, Roger E. McLendon, Terence Z. Wong, and Darell D. Bigner. Clinical experience with -particleemitting 211at: Treatment of recurrent brain tumor patients with 211at-labeled chimeric antitenascin monoclonal antibody 81c6. *Journal of Nuclear Medicine*, 49(1):30–38, 2008. doi: 10.2967/jnumed.107.046938. URL http://jnm.snmjournals.org/content/49/1/30.abstract.

[30] L. Gaffney et al. Studies of pear-shaped nuclei using accelerated radioactive beams. *Nature*, TBP:TBP, May 2013. URL TBPSOON.

[31] Isolde website, 2013. URL http://isolde.web.cern.ch/isolde/.

[32] P. Van Duppen, J. Al-Khalili, and E. Roeckl. *"Isotope Separation On Line and Post Acceleration" in The Euroschool lectures on physics with exotic beams, Vol II*. Springer, 2006.

[33] L. Ghys. Investigation of the atomic properties of At with resonant laser ionization in order to develop pure radioactive ion beams. Master's thesis, IKS, KULeuven, 2011. URL http://fys.kuleuven.be/iks/ns/phd-master-theses.

[34] T.E. Cocolios. *Single-particle and collective properties around closed shells probed by in-source laser spectroscopy*. PhD thesis, IKS, KULeuven, 2010. URL http://fys.kuleuven.be/iks/ns/phd-master-theses.

[35] G. Knoll. *Radiation detection and measurement*. John Wiley & Sons, 1999.

[36] Ortec website, 2013. URL http://www.ortec-online.com.

[37] Canberra website, 2013. URL http://www.canberra.com.

[38] A. Menchaca-Rocha, J.I. Cabrera, R. Alfaro, E. Belmont-Moreno, and A. Martnez-Dvalos. A new approach to deal with non-linearities in si detector response. *Nuclear Instruments and Methods in Physics Research Section B: Beam Interactions with Materials and Atoms*, 207(3):356 – 367, 2003. ISSN 0168-583X. doi: 10.1016/S0168-583X(03)00674-8. URL http://www.sciencedirect.com/science/article/pii/S0168583X03006748.

[39] G. Bortels and P. Collaers. Analytical function for fitting peaks in alpha-particle spectra from si detectors. *International Journal of Radiation Applications and Instrumentation. Part A. Applied Radiation and Isotopes*, 38(10):831 – 837, 1987. ISSN 0883-2889. doi: 10.1016/0883-2889(87)90180-8. URL http://www.sciencedirect.com/science/article/pii/0883288987901808.

[40] R. Firestone et al. *Table of Isotopes*. John Wiley & Sons, 1996.

[41] T. Kibedi, T.W. Burrows, M.B. Trzhaskovskaya, P.M. Davidson, and C.W. Nestor Jr. Evaluation of theoretical conversion coefficients using bricc. *Nuclear Instruments and Methods in Physics Research Section A: Accelerators, Spectrometers, Detectors and Associated Equipment*, 589(2):202 – 229, 2008. ISSN 0168-9002. doi: 10.1016/j.nima.2008.02.051. URL http://www.sciencedirect.com/science/article/pii/S0168900208002520.

[42] P. Van Duppen et al. Intruder states in odd-odd tl nuclei populated in the alpha - decay of odd-odd bi isotopes. *Nuclear Physics A*, 529(2):268–288, 1991. doi: 10.1016/0375-9474(91)90796-9. URL http://www.sciencedirect.com/science/article/pii/0375947491907969.

[43] O. Helene. Upper limit of peak area. *Nuclear Instruments and Methods in Physics Research*, 212(13):319 – 322, 1983. ISSN 0167-5087. doi: 10.1016/0167-5087(83)90709-3. URL http://www.sciencedirect.com/science/article/pii/0167508783907093.

[44] H. W. Schmitt, W. E. Kiker, and C. W. Williams. Precision measurements of correlated energies and velocities of ^{252}Cf fission fragments. *Phys. Rev.*, 137: B837–B847, Feb 1965. doi: 10.1103/PhysRev.137.B837. URL http://link.aps.org/doi/10.1103/PhysRev.137.B837.

[45] L. Ghys. Calibration of surface barrier and pips detectors for heavy ion experiments done at ill, 2012.

[46] Stopping range of ions in matter (srim),2013 version, 2013. URL http://www.srim.org.

[47] O. Helene. Errors in experiments with small numbers of events. *Nuclear Instruments and Methods in Physics Research Section A: Accelerators, Spectrometers, Detectors and Associated Equipment*, 228(1):120 – 128, 1984. ISSN 0168-9002. doi: 10.1016/0168-9002(84)90020-2. URL http://www.sciencedirect.com/science/article/pii/0168900284900202.

Intstituut voor Kern en Stralingsfysica
Celestijnenlaan 200D bus 2418
3000 LEUVEN, BELGIË
tel. + 32 16 32 72 63
fax + 32 16 32 79 85
fabienne.vanalphen@kuleuven.be
www.kuleuven.be